TUDelft

Delft University of Technology

Universal characterization of wall turbulence for fluids with strong property variations

Patel, Ashish

Important note
To cite this publication, please use the final published version (if applicable).
Please check the document version above.

Universal characterization of wall turbulence for fluids with strong property variations

Proefschrift

ter verkrijging van de graad van doctor
aan de Technische Universiteit Delft,
op gezag van de Rector Magnificus prof. ir. K.C.A.M. Luyben,
voorzitter van het College voor Promoties,
in het openbaar te verdedigen op maandag 19 juni 2017 om 12:30 uur

door

Ashish Patel

Master of Science in Mechanical Engineering,
Technische Universiteit Delft,
geboren te Raipur, India.

Dit proefschrift is goedgekeurd door de

promotor: prof. dr. ir. B. J. Boersma
copromotor: dr. R. Pecnik

Samenstelling promotiecommissie:

Rector Magnificus,	voorzitter
Prof. dr. ir. B. J. Boersma,	Technische Universiteit Delft
Dr. R. Pecnik,	Technische Universiteit Delft

Onafhankelijke leden:

Prof. dr. N. D. Sandham,	University of Southampton
Prof. dr.-ing. S. Jakirlic,	Technische Universität Darmstadt
Prof. dr. J. G. M. Kuerten,	Technische Universiteit Eindhoven
Prof. dr. ir. C. H. Venner,	Universiteit Twente
Prof. dr.-ing. S. Hickel,	Technische Universiteit Delft
Prof. dr. ir. C. Poelma,	Technische Universiteit Delft, reservelid

Dedicated to the leading ladies of my life

Mummy, Nidhi & Niara

CONTENTS

SUMMARY

Wall-bounded turbulence involving mixing of scalars, such as temperature or concentration fields, play an important role in many engineering applications. In applications with large temperature or concentration differences, the variation of scalar dependent thermophysical properties can be strong. In such cases the strong coupling between energy and momentum alters the conventional behavior of turbulence. This alteration results in peculiar momentum and heat transfer characteristics, for which conventional scaling laws for constant property flows fail and cannot be applied. The aim of this work is to characterize wall-bounded turbulence for fluids that have large near-wall gradients in thermophysical properties. The focus is on the variable inertia effects at the low-Mach number limit without the influence of buoyancy. First, a theoretical framework is developed by applying a scaling transformation to the Navier–Stokes equations, that is based on local mean values of density $\overline{\rho}$, viscosity $\overline{\mu}$ and semi-local friction velocity $u_\tau^\star = \sqrt{\tau_w/\overline{\rho}}$ (τ_w is the wall shear stress). The framework suggests that the leading order effect of varying properties on turbulence can effectively be characterized by the semi-local Reynolds number $Re_\tau^\star \equiv \sqrt{(\overline{\rho}/\rho_w)}/(\overline{\mu}/\mu_w) Re_\tau$ (Re_τ is the friction Reynolds number based on wall values). Second, Direct Numerical Simulations (DNS) of a fully developed internally heated channel flow are performed with different relations for density ρ, viscosity μ and thermal conductivity λ as a function of temperature, to test the proposed framework and to further analyse the scaling of turbulence statistics. Using the above two methodologies following insights are gained:

- The semi-local Reynolds number $Re_\tau^\star$ accounts for changes in viscous length scales due to property variations.
- Turbulence statistics and the characteristics of turbulent structures are strongly governed by $Re_\tau^\star$ profiles, and their dependence on individual density and viscosity profiles is minor.
- The viscous shear stress shows a universal collapse in the inner layer for all cases when plotted as a function of the semi-local wall coordinate $y^\star$. This universal collapse provides a basis to derive an extension of the van Driest transformation $\overline{u}^\star = \int_0^{\overline{u}^{vD}} \left(1 + (y/Re_\tau^\star)\, dRe_\tau^\star/dy\right) d\overline{u}^{vD}$ ($\overline{u}^{vD}$ is the van Driest transformed velocity), that accounts for gradients in $Re_\tau^\star$ and is able to collapse velocity profiles for all the investigated cases.

- Other turbulence statistics like mixing length, turbulence anisotropy and turbulent vorticity fluctuations do not show a universal scaling very close to the wall. This is attributed to strong non-local effects and structural changes in turbulence that affect lifting and tilting of quasi-streamwise vortices. These structural changes are related to changes in wall-normal gradient of $\overline{u}^{vD}$ and are analogous to the effects associated with changes in mean velocity gradient of a constant density flow.
- The scaling characteristics of scalar field can also be parametrized using the distribution of the local Prandtl number $Pr^\star \equiv Pr_w (\overline{\mu}/\mu_w)/(\overline{\lambda}/\lambda_w)$ (Pr_w is the Prandtl number based on wall values) and $Re_\tau^\star$.
- Similar to the extended van Driest transformed velocity, an analogous extended van Driest transformed mean temperature profile has been derived $\overline{\theta}^\star = \int_0^{\overline{\theta}^{vD}} \left(1 + \left(y/Re_\tau^\star\right) dRe_\tau^\star/dy\right) d\overline{\theta}^{vD}$, which results in a good collapse of the temperature profiles for cases with similar $Pr^\star$ distributions, irrespective of the $Re_\tau^\star$ distribution.
- Finally, it is shown that if a turbulence model is solved in a form consistent with semi-local framework, the obtained results from the model agree well with results from DNS, while the conventional modeling approach fails.

SAMENVATTING

Het turbulente transport van scalaire grootheden zoals de temperatuur of de concentratie nabij een wand speelt een belangrijke rol in veel industriële toepassingen. In toepassingen met grote temperatuur- of concentratieverschillen kan de variatie van de thermofysische eigenschappen zeer groot zijn. In dergelijke gevallen kan de sterke koppeling tussen energie en impuls het conventionele gedrag van turbulentie doen veranderen. Deze verandering zorgt voor vreemde impuls- en warmteoverdrachtskarateristieken die er toe leiden dat conventionele schalingswetten voor stromingen met constante eigenschappen niet langer toepasbaar zijn. Het doel van dit werk is turbulentie nabij de wand te karakteriseren voor vloeistoffen met grote thermofysische eigenschapsgradienten. De nadruk ligt op variabele traagheidseffecten in de lage Mach-benadering waarbij de opwaartsekracht als verwaarloosbaar beschouwd wordt. Allereerst wordt een theoretisch kader ontwikkeld door een scalingstransformatie toe te passen op de Navier–Stokes vergelijking die gebaseerd is op de lokale gemiddelde waardes van de dichtheid $\overline{\rho}$, viscositeit $\overline{\mu}$ en de semi-lokale frictiesnelheid $u_\tau^\star = \sqrt{\tau_w/\overline{\rho}}$ (waarbij τ_w de schuifspanning is op de wand). Het kader suggereert dat het primaire effect van de variabele stofeigenschappen op turbulentie goed gekarakteriseert kan worden door het semi-lokale Reynolds-getal $Re_\tau^\star \equiv \sqrt{(\overline{\rho}/\rho_w)}/(\overline{\mu}/\mu_w)Re_\tau$ (waarbij Re_τ het frictie-Reynolds-getal is, hetgeen gebaseerd is op waardes op wand). Ten tweede zijn Direkte Numerieke Simulaties (DNS) van volledig ontwikkelde en intern verhitte kanaalstromingen uitgevoerd, waarbij verschillende relaties voor de dichtheid ρ, viscositeit μ en warmtegeleidingscoefficient λ als functie van de temperatuur zijn toegepast, om zo het voorgestelde kader te testen en de schaling van de turbulente statistieken verder te kunnen analyseren. Gebruikmakend van de hiervoor beschreven methodiek zijn de volgende inzichten vergaard:

- Het semi-lokale Reynolds getal $Re_\tau^\star$ verklaart veranderingen in de viskeuze lengteschaal ten gevolge van eigenschapsvariaties.
- Turbulente statistieken en de karakteristiek van de turbulente structuren worden in sterke mate bepaald door de $Re_\tau^\star$ profielen en hun afhankelijkheid van individuele dichtheids- en viscositeitsprofielen is minder van belang.
- De viskeuze schuifspannig valt voor alle gevallen samen als deze uitgezet wordt tegen de semi-lokale wandcoördinaat $y^\star$. Dit op universele wijze samenvallen biedt een basis om een extensie van de van-Driest-transformatie af

te leiden, $\overline{u}^{\star} = \int_0^{\overline{u}^{\mathrm{vD}}} \left(1 + \left(y/Re_{\tau}^{\star}\right) dRe_{\tau}^{\star}/dy\right) d\overline{u}^{\mathrm{vD}}$ (waarbij $\overline{u}^{\mathrm{vD}}$ de van-Driest-getransformeerde snelheid is), die de gradienten in $Re_{\tau}^{\star}$ in acht neemt en die het mogelijk maakt om the snelheidsprofielen van alle onderzochte gevallen samen te laten vallen.

- Andere turbulente statistieken, zoals de mixlengte, turbulente anisotropie en de turbulente vorticiteitsfluctuaties laten niet een universele schaling zien dicht in de buurt van de wand. Dit valt de wijten aan sterke niet-lokale effecten en structurele veranderingen in turbulente die het optillen en het kantelen van quasi-stroomsgewijze kolken beïnvloeden. Deze structurele veranderingen zijn geralateerd aan veranderingen in de wand-normale gradient van $\overline{u}^{\mathrm{vD}}$ en ze zijn analoog aan de effecten die geassocieerd worden met veranderingen in de gemiddelde snelheidsgradient van een stroming met een konstante dichtheid.

- De schalingskaratteristieken van een scalair veld kunnen ook geparametriseerd worden door de verdeling van het lokale Prandtl-getal $Pr^{\star} \equiv Pr_w(\overline{\mu}/\mu_w)/(\overline{\lambda}/\lambda_w)$ (waarbij Pr_w het Prandtl-getal gebaseerd is op waardes op de wand) en $Re_{\tau}^{\star}$ te gebruiken.

- Een uitbreiding van het van-Driest-getransformeerde temperatuurprofiel, wat analoog is aan de uitbreiding van de van-Driest-getransformeerde snelheid, is afgeleid als $\overline{\theta}^{\star} = \int_0^{\overline{\theta}^{\mathrm{vD}}} \left(1 + \left(y/Re_{\tau}^{\star}\right) dRe_{\tau}^{\star}/dy\right) d\overline{\theta}^{\mathrm{vD}}$, welke resulteert in het bevredigend samenvallen van de temperatuurprofielen voor gevallen waarbij de $Pr^{\star}$ verdeling vergelijkbaar is, onafhankelijk van de $Re_{\tau}^{\star}$ verdeling.

- Ten slotte wordt aangetoont dat als een turbulentie model opgesteld wordt in een vorm die overeenkomt met het semi-lokale kader, komen de verkregen resultaten van het model goed overeen met de resultaten van de direkte numerieke simulatie, terwijl conventionele modellering faalt.

1

INTRODUCTION

1.1. MOTIVATION

TURBULENT FLOWS

Turbulence is omnipresent. When you blow off a lit candle, what you see in the smoke that follows is turbulence. The leaves falling from the tree are swayed from its path due to turbulence. When you add milk to your coffee, they mix due to turbulence. When you look at stormy patterns of *The Starry Night* by Vincent van Gogh, you see an uncanny physical resemblance to turbulence[1]. In short, turbulence is everywhere; sometimes you can see it happening right in front of you and sometimes it is the hidden protagonist behind a phenomenon. This protagonist can be the hero of a tale or a villain in another, nonetheless an important one. For example, it is turbulence within the earth's core that sustains the earth's magnetic field and protects us from the charged particles emitted from the sun. Alternatively, it is the same turbulence that creates aerodynamic drag for airplanes, ships or cars reducing their efficiency.

While a formal definition of turbulence is yet to be formulated, it is loosely defined as a state of fluid motion which is characterized by random and chaotic three-dimensional motions of varying time and length scales. Turbulent fluid motion arises when inertial forces dominate viscous forces, such that the equilibrium of the flow is disturbed as viscous forces couldn't act rapidly to damp out the induced perturbation. The ratio of inertial to viscous force gives a dimensionless parameter known as the Reynolds number *Re*, named after Osborne Reynolds who performed classic pipe flow experiments (Reynolds, 1883). He injected a dye stream into the centre of the pipe with flowing water and observed that for low flow velocity the dye stream remained straight and undisturbed, on increasing the flow velocity the dye stream mixed with the surrounding water, filling the pipe with colored water. For a given flow configuration, there exists a critical Reynolds number above which the flow becomes turbulent. The qualitative features of turbulence were later described by Richardson (1922) and Kolmogorov (1941). The large inertial forces create motions with large length and time scales (also known as large eddies), which themselves are unstable to inertial forces and break into smaller eddies. The process continues until the eddy size becomes small enough to be influenced by viscous force directly, dissipating motion into heat. This energy cascade process therefore results in the presence of a large range of length and time scales in the flow. While this qualitative description forms a strong basis for our current understanding of turbulence, its

---

[1] Van Gogh painted perfect turbulence `http://www.nature.com/news/2006/060703/full/news060703-17.html`

complete physical description still remains one of the major unresolved problems in physics (Ginzburg, 2013). The physics of turbulence is governed by the Navier–Stokes equations, the mathematical properties of which comprises one of the seven Millennium prize problem in mathematics (Carlson *et al.*, 2006). When turbulence is present, it usually dominates all other flow phenomena and results in increased energy dissipation, mixing, heat transfer, and drag (George, 2013), making it important from an engineering perspective as well. The problem of turbulence has therefore been studied for more than a century by physicist, mathematicians and engineers, yet our understanding of it has developed rather slowly.

The turbulence problem which by nature exhibits multiple length scales, becomes even more complex when the flow is confined by one or more solid walls. The presence of a wall introduces an additional length scale in terms of inhomogeneous wall-normal distance and fundamentally changes the nature of turbulence (Smits & Marusic, 2013). Although geometrically thin, the near-wall region is responsible for a large fraction of the velocity drop (Jiménez & Moser, 2007) and accounts for a significant amount of turbulence production across the boundary layer, playing a crucial role in drag and heat transfer. For example, this near-wall region accounts for up to 50% of the aerodynamic drag on modern airliners and occupy approximately the first 100 meters of our atmosphere (Marusic *et al.*, 2010*b*). About 25% of the energy used by industry and commerce is spent in moving fluids along pipes and canals, or vehicles through air or water, and about one quarter of that energy is dissipated by turbulence in the immediate vicinity of walls (Jiménez, 2013). Despite the chaotic and random nature of turbulence, wall-bounded turbulence consists of coherent structures that exhibit organized motions that are persistent in time and space; these coherent structures are responsible for the sustenance of wall turbulence and contribute significantly to the transport of heat, mass, and momentum (Marusic *et al.*, 2010*c*). Wall turbulence is of special engineering relevance, since its understanding is important in the design of moving objects like airplanes, ships, automobiles and equipments like heat-exchangers, pipelines, chemical reactors, wind turbines, bio-medical devices, propulsion and combustion systems. Besides engineering applications, wall turbulence is also a key to understand our natural surroundings, as it influences weather, oceanic currents and pollution levels.

Engineers and scientists have often relied on experimental and computational approaches to understand wall turbulence. Both approaches have their limitations and often complement each other. Experimental approaches, face difficulty in near-wall measurements, are limited in terms of spatial resolution and also simultaneous measurements of all flow variables (like velocity components, pressure or temperature) is difficult. Direct Numerical Simulation (DNS),
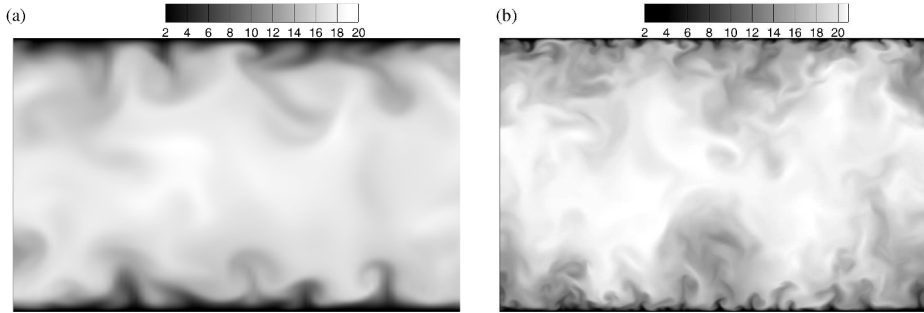
Figure 1.1: Contours of streamwise velocity in a channel flow (flow is into the plane) for Reynolds number based on friction velocity and half-channel height of (a) 150 and (b) 550.

which involve numerical simulations of the Navier–Stokes equations provides a fully resolved spatial and time-series data of velocity, pressure and other flow variables. However, DNS is computationally intensive because of the wide range of scales that need to be resolved. The range of scales increases with increase in the Reynolds number. A glimpse of this is given in figure 1.1, which shows the contour of streamwise velocity in a plane perpendicular to the flow for two different Reynolds numbers. The flow configuration is a channel and data is obtained using an in house DNS code. Due to the increase in length scales, DNS is currently limited to moderate Reynolds numbers. Nonetheless, recent advances in computational and experimental facilities, have revealed some important aspects of universality and scaling phenomenology of wall turbulence in incompressible flows. There has been considerable progress in understanding how turbulence intensities depend on the Reynolds number and predictive models for estimating them have been proposed (Marusic *et al.*, 2010*a,b*).

TURBULENT FLOWS WITH VARIABLE THERMOPHYSICAL PROPERTIES

Turbulent mixing of scalars like temperature or concentration plays an important role in many of the above mentioned engineering applications. Applications which involve small temperature or concentration differences do not influence the turbulent motions and are known as passive scalars. However, in applications with large temperature or concentration differences, the variation of scalar dependent thermophysical properties can be strong. In such cases, the effects of thermophysical property variations can be strong enough to modulate turbulence and the traditional approach of treating temperature as a pas-

sive scalar no longer holds. These make the flow state even more complex and standard correlations or models developed for constant property flows fail to reliably predict the turbulence behavior. Some of the well-known examples which involve variable thermophysical properties include supersonic flows for aircraft and propulsion systems, strongly heated or cooled flows in heat exchangers, or chemically reacting flows in combustion chambers. Further to these, a detailed understanding of turbulent flows with variable thermophysical properties is required in order to facilitate the development of future energy conversion systems which aim, to reduce our dependence on fossil fuel and to exhibit higher energy efficiency. For example, in the past decade, there has been an increased interest in heated and cooled fluids at supercritical pressure for novel thermodynamic power cycles. These thermodynamic cycles exhibit high thermal efficiency and are suitable for low-grade heat to power conversion (Chen *et al.*, 2010), for concentrated solar power plants (Iverson *et al.*, 2013) and for nuclear power plants (Dostal *et al.*, 2004). However, fluids slightly above the supercritical pressure and close to the pseudo-critical temperature pose strong thermophysical property variations due to strong dependence of properties on temperature. These result in peculiar heat transfer characteristics, which is difficult to predict using standard heat transfer correlations (Pioro *et al.*, 2004) as well as with numerical studies that rely on turbulence models (He *et al.*, 2008). This has resulted in dedicated studies to investigate turbulence characteristics of fluids undergoing heat transfer at supercritical pressure (see for e.g. Nemati, 2016; Peeters, 2016). Another, recent development in order to tackle the increasing demand of cooling in high heat flux equipments is the use of nanofluids which consists of nanoparticles suspended in fluids (Das *et al.*, 2006). Nanofluids are also considered a promising technology for directly absorbing the solar radiation, enabling them to act as volumetric solar receivers (Lenert & Wang, 2012). Volumetric receivers have a potential to transfer energy to carrier fluid in a more effective way as compared to conventional surface based receiver which suffer significant emissive losses at high operating temperatures. The thermophysical properties of nanofluid are also a strong function of both temperature and concentration. Therefore, in order to develop more efficient energy and transportation systems, it is important to understand how turbulence is affected by variation in properties and how conventional models could be extended to incorporate the effect of variable properties.

1.2. OBJECTIVE

The aim of the thesis can be divided into following broad categories:

- Developing a framework for studying wall-turbulence under variable property conditions.

- Conduct direct numerical simulations to test the suitability of the framework and to generate a database for a generalized study of variable property wall turbulence.

- Detailed investigation of physical mechanisms that results in structural changes and consequently in modulated turbulence statistics.

- Characterize the modification of turbulence statistics using a scaling parameter that accounts for the combined influence of variable properties on turbulent boundary layers.

- Propose improvement to existing turbulence models.

1.3. OUTLINE

Chapter 2 presents a theoretical background wherein the governing equations are described. A short review and discussion on some relevant literature results is also carried out.

Chapter 3 discusses the semi-local scaling framework that motivates the simulation study. First, a hypothesis that follows from semi-local scaling is put forward. Second, a mathematical proof for the validity of the semi-local scaling is provided. Third, the DNS cases and computational setup is described. Finally, the DNS results are used to validate the proposed hypothesis.

Chapter 4 discusses the characteristics of mean velocity scaling and an extension of van Driest velocity transformation is derived.

Chapter 5 discuses the modulation of turbulence statistics and structures due to property gradients.

Chapter 6 discusses the scaling characteristics of the scalar field.

Chapter 7 addresses the implication of the findings in previous chapters for turbulence modeling and proposes improvement to existing models.

Chapter 8 provides a summary of the present study.

2

THEORETICAL BACKGROUND

2.1. GENERAL ASSUMPTIONS AND GOVERNING EQUATIONS

The equations of motion governing the dynamics of a compressible flow are given by the momentum conservation equations (also known as the Navier–Stokes equation), the mass conservation (also known as the continuity equation) and the energy conservation equations. Furthermore, functional relationships are used to evaluate thermophysical properties such as density ρ, dynamic viscosity μ, thermal conductivity λ and specific heat c_p as a function of temperature T and pressure P. Such a functional relation for density is also known as an equation of state. For most of the fluids including air and water, μ, λ and c_p show a dependency on temperature only. Effects associated with density changes in response to changes in pressure are regarded as compressibility effects. These are different from variable inertia effects which are associated with changes due to temperature (Lele, 1994). The former effect is proportional to the Mach number of the flow and is important at high speeds, while the latter can be important at all speeds when intense heat transfer is present.

In the present work, we consider heat transfer at low-Mach numbers and are interested in variable inertia effects due to density changes. Based on previous experimental and numerical studies of supersonic air flows, it is known that compressibility plays an important role in the dynamics of free shear layers, where it is known to be directly responsible for the growth rate reduction of the shear layer thickness (Bradshaw, 1977; Papamoschou & Roshko, 1988; Sarkar, 1995; Vreman *et al.*, 1996). However, direct effects of compressibility on supersonic boundary layers for flows with moderate Mach numbers ($Ma < 5$) are known to be small (Coleman *et al.*, 1995; Lechner *et al.*, 2001; Guarini *et al.*, 2000; Maeder *et al.*, 2001; Pirozzoli *et al.*, 2004; Smits & Dussauge, 2006; Lagha *et al.*, 2011*a*) and any differences from an incompressible boundary layer can be accounted for by mean variations of fluid properties. In the near-wall region of a supersonic boundary layer, most of the near-wall density and temperature fluctuations are the result of solenoidal 'passive mixing' by turbulence, and density fluctuations show little correlation with pressure fluctuations (Coleman *et al.*, 1995; Lechner *et al.*, 2001). Sarkar (1995) explained the differences in the extent of compressibility effects between mixing layers and boundary layers using gradient Mach number M_g. He showed that, M_g increases more rapidly in the mixing layer than in the boundary layer, when the mean Mach number of the flow increases. In that respect, studying the influence of property gradients without compressibility effects is in line with previous studies on supersonic wall-bounded flows. Therefore, the low Mach number approximation of the Navier-Stokes equations in Cartesian coordinates is used to simulate the turbulent flow in a channel. In the low Mach number limit acoustic wave propagation is ignored and the pres-

sure field is decomposed into a thermodynamic $P_0(t)$ and a hydrodynamic component $p(x_i, t)$ (Majda & Sethian, 1985; Nemati *et al.*, 2015). Furthermore, we assume a calorifically perfect fluid in a closed system with zero net heat flux, for which it can be shown that P_0 is independent of time (Nicoud, 2000). The density and transport properties can then be evaluated independently of the hydrodynamic pressure variations ($p \ll P_0$) as a function of temperature alone. Under these assumptions, the governing equations for mass, momentum and energy can be expressed in non-dimensional form as

$$\frac{\partial \rho}{\partial t} + \frac{\partial \rho u_j}{\partial x_j} = 0, \tag{2.1}$$

$$\frac{\partial \rho u_i}{\partial t} + \frac{\partial \rho u_i u_j}{\partial x_j} = -\frac{\partial p}{\partial x_i} + \frac{1}{Re_\tau}\frac{\partial \tau_{ij}}{\partial x_j} + \rho Ri_i, \tag{2.2}$$

$$\frac{\partial \rho H}{\partial t} + \frac{\partial \rho u_j H}{\partial x_j} = \frac{1}{Re_\tau Pr_w}\frac{\partial}{\partial x_j}\left(\lambda \frac{\partial T}{\partial x_j}\right) + \frac{\phi}{Re_\tau Pr_w}, \tag{2.3}$$

with the stress tensor $\tau_{ij} = \mu\left[(\partial u_i/\partial x_j + \partial u_j/\partial x_i) - \frac{2}{3}\,\partial u_k/\partial x_k\,\delta_{ij}\right]$ and δ_{ij} the Kronecker delta. The equations are written in non-dimensional form by using following non-dimensional variables

$$x_i = \frac{x_i^0}{h^0}, \quad t = \frac{t^0}{h^0/u_\tau^0}, \quad u_i = \frac{u_i^0}{u_\tau^0}, \quad p = \frac{p^0}{\rho_w^0 u_\tau^{0^2}}, \quad T = \frac{T^0}{T_w^0},$$

$$H = \frac{H^0}{c_{pw}^0 T_w^0}, \quad \rho = \frac{\rho^0}{\rho_w^0}, \quad \lambda = \frac{\lambda^0}{\lambda_w^0}, \quad c_p = \frac{c_p^0}{c_{pw}^0}, \quad \mu = \frac{\mu^0}{\mu_w^0}, \tag{2.4}$$

where x_i, t, u_i, p, T, H and ϕ are the spatial coordinates, time, velocity, pressure, temperature, enthalpy and volumetric heat source term, respectively, with the superscript 0 indicating the dimensional quantities and subscript w the averaged wall values. $u_\tau^0 = \sqrt{\tau_w^0/\rho_w^0}$ is the friction velocity based on averaged wall values and h^0 is the half channel height. The Reynolds number, Prandtl number and Richardson number are defined as

$$Re_\tau = \frac{\rho_w^0 u_\tau^0 h^0}{\mu_w^0}, \qquad Pr_w = \frac{\mu_w^0 c_{pw}^0}{\lambda_w^0}, \qquad Ri_i = \frac{g_i^0 h^0}{u_\tau^{0^2}}, \tag{2.5}$$

where g_i^0 is the magnitude of gravitational acceleration. In the present work our focus is on identifying effects of variable property without buoyancy effects so that $Ri_i = 0$. For a physical system it implies one or more of the following conditions- a micro-gravity operating condition, a small half-channel height h^0,

or a high flow velocity. The latter is specifically true in supersonic flows. Since the following results will be discussed based on non-dimensional quantities, the superscript 0 will be dropped.

2.2. STATISTICAL AVERAGING

In order to study statistical properties of turbulence, following averaging procedures are used in the present work.

REYNOLDS AVERAGING

A generic variable γ can be decomposed into a Reynolds averaged mean part $\overline{\gamma}$ and a fluctuating part γ', such that,

$$\gamma = \overline{\gamma} + \gamma', \tag{2.6}$$

where,

$$\overline{\gamma'} = 0, \tag{2.7}$$

and

$$\overline{\gamma} = \frac{1}{N} \sum_{1}^{N} \gamma, \tag{2.8}$$

N being the number of samples.

FAVRE AVERAGING

In case of flows with variable density, the density-weighted averaging is often used to retain the simplified form of equations obtained through the conventional Reynolds averaging approach in constant density flows (see for e.g. Wilcox, 2006). A generic variable γ can be decomposed into a Favre averaged mean part $\tilde{\gamma}$ and a fluctuating part γ'', such that,

$$\gamma = \tilde{\gamma} + \gamma'', \tag{2.9}$$

where,

$$\tilde{\gamma} = \frac{\overline{\rho\gamma}}{\overline{\rho}}, \tag{2.10}$$

$$\overline{\gamma''} \neq 0, \tag{2.11}$$

but,

$$\overline{\rho\gamma''} = 0. \tag{2.12}$$

2.3. CURRENT UNDERSTANDING

CONSTANT PROPERTY WALL TURBULENCE

For constant property wall turbulence, the most relevant Reynolds number is the friction Reynolds number $Re_\tau = \delta_o/\delta_\nu$ (Marusic *et al.*, 2010*b*). It can be interpreted as a ratio of the outer length scale δ_o (which can be the half channel height h, the boundary-layer thickness δ, or the pipe radius R) and an inner length scale $\delta_\nu = \mu_w/(\rho_w u_\tau)$. A non-dimensional wall distance $y^+ = y/\delta_\nu$ can then be used to decompose the turbulent boundary layer into distinct layers namely, a viscous sublayer where viscosity is dominant, a buffer layer in which both viscosity and inertial effects should be taken into account and an outer layer where direct effect of viscosity is negligible. In a classical view (Gad-el Hak & Bandyopadhyay, 1994), the viscous sublayer is taken to be $0 < y^+ < 5$ and buffer layer is $5 < y^+ < 30$ and the outer region is $30 < y^+ < Re_\tau$. The viscous sublayer and the buffer layer together constitute the so called near-wall region. Relevant length and velocity scales in the near-wall region are δ_ν and u_τ, while in the outer layer the length scale is of the order δ_o and velocity scale continues to be u_τ, since u_τ sets up the inner boundary condition for outer flow (Marusic *et al.*, 2010*c*). At sufficiently high Reynolds numbers there also exists a region where both δ_ν and δ_o are relevant length scale and the region is defined as the overlap/log-law layer. This overlap region in a classical view (Gad-el Hak & Bandyopadhyay, 1994) is taken to be $30 < y^+ < 0.2Re_\tau$. The overlap layer together with the near-wall region constitutes the inner layer. This classification of different regions is primarily based on the scaling behavior of mean streamwise velocity. A glimpse of this velocity scaling behavior can be seen in figure 2.1(a), which uses the database of a turbulent channel flow from Lee & Moser (2015) at different Re_τ values. A good collapse of the velocity profile is evident in the inner layer for all the cases. This universal behavior of the velocity profile in the inner layer has received widespread research attention to investigate the universality of turbulence, specially in the near-wall region. While the classical scaling is able to provide an approximate collapse of Reynolds stresses in the near-wall region, there is no universal scaling with respect to Reynolds number (Morrison *et al.*, 2004; Hoyas & Jiménez, 2006). The peak amplitude of streamwise and spanwise fluctuations increase logarithmically with Re_τ, while wall-normal fluctuations increase sublogarithmically (Bernardini *et al.*, 2014). The influence of large-scale outer-layer motions on the near-wall cycle increases with Reynolds number (Morrison *et al.*, 2004; Hutchins & Marusic, 2007; Marusic *et al.*, 2010*a*). This Re_τ dependence of the streamwise turbulence intensity can be seen using data from Lee & Moser (2015) in figure 2.1(b), from which it can be seen that, even though the peak oc-

curs at similar $y^+ \approx 12$ values, the peak value increases with Re_τ. The large scale motions also influence the scaling of turbulence kinetic energy dissipation per unit volume ϵ (Hoyas & Jiménez, 2008), thereby showing Re_τ dependence. This dependence can be seen in figure 2.1(c). Nonetheless, the viscous length scales serve as a useful scaling parameter and is an important foundation in understanding the near-wall turbulence. It provides a good scaling in the inner layer for relevant turbulent length scales such as the Kolmogorov and mixing length scale. The Kolmogorov length scale η is a measure of smallest scales of motion and is defined as

$$\eta = \left(\left(\frac{\overline{\mu}}{\overline{\rho}} \right)^3 \frac{\overline{\rho}}{\epsilon} \right)^{0.25} , \tag{2.13}$$

A plot of η, normalized by wall-based viscous length scales and plotted as a function of y^+ is shown in figure 2.2(a) for different Reynolds numbers using data from Lee & Moser (2015). Since η is a function of ϵ it also has a Re_τ dependence in the near-wall region, however this dependence is weak since the expression for η has a exponent of ϵ which is less than one (=1/4). A good collapse in the inner layer can therefore be seen. DNS studies which are required to resolve all scales of turbulent motions, therefore estimate the mesh requirements for simulating wall-bounded turbulence, using these wall-based viscous scales. The mixing length l_m, which provides a quantitative measure of the size of the most energetic eddies responsible for momentum transfer, can be defined as

$$l_m{}^2 = \frac{-\overline{u'v'}}{\left(d\overline{u}/dy\right)^2}, \tag{2.14}$$

where $-\overline{u'v'}$ is the turbulent shear stress and $d\overline{u}/dy$ is the gradient of mean streamwise velocity. A good collapse of l_m, normalized by wall-based viscous scale in the inner layer, can be seen in figure 2.2(b).

Apart from turbulence statistics, the structural features of near-wall turbulence have also been investigated in great detail in the past decades. The dominant structures of the near-wall region are streamwise velocity streaks and quasi-streamwise vortices. Streaks (Kline *et al.*, 1967) are spanwise modulation of streamwise velocity and consist of low- and high-speed streaks (Smith & Metzler, 1983). The wall-based scaling is also successful in scaling the streak spacing which are known to remain invariant over a wide range of Reynolds numbers (Klewicki *et al.*, 1995). The quasi-streamwise vortices, primarily found in the buffer layer, are slightly inclined away from the wall and tilted in spanwise directions (Jeong *et al.*, 1997). Additionally, it is known that the dynamics of near-wall turbulence can be maintained autonomously by a self-sustaining process, where the streaks and the vortices continue regenerating each other independently of
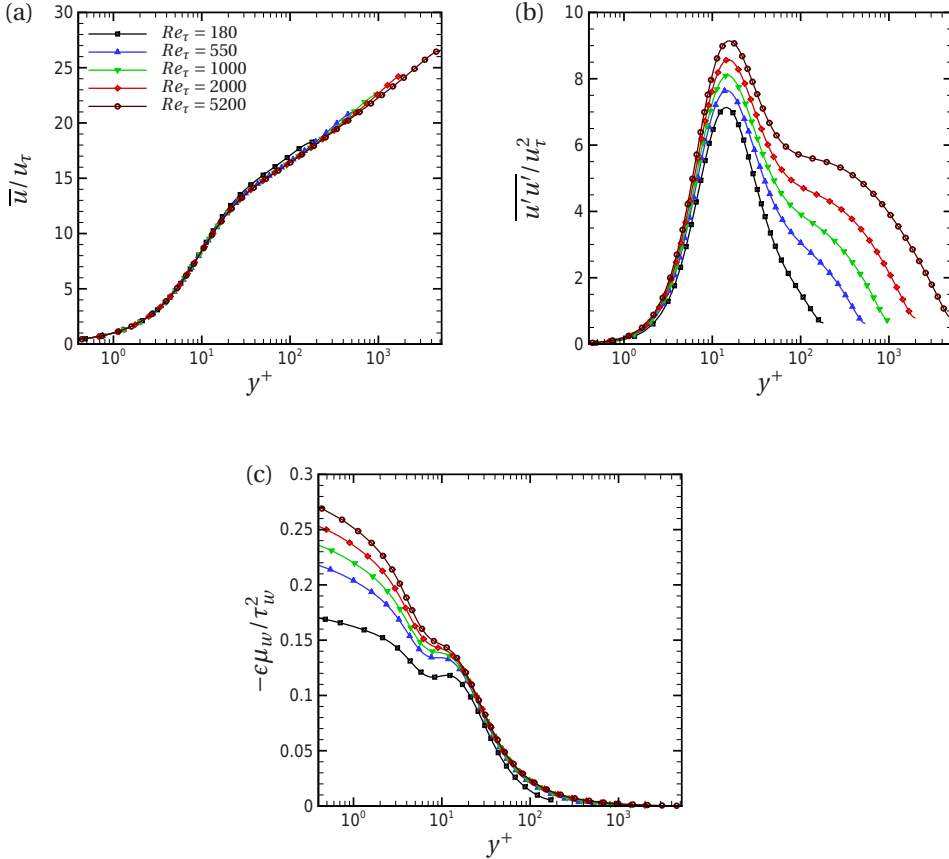
Figure 2.1: (a) Mean streamwise velocity profile, (b) streamwise turbulence intensity and (c) turbulence kinetic energy dissipation per unit volume for different Re_τ values, plotted as a function of y^+, using data of constant property turbulent channel flows from Lee & Moser (2015).
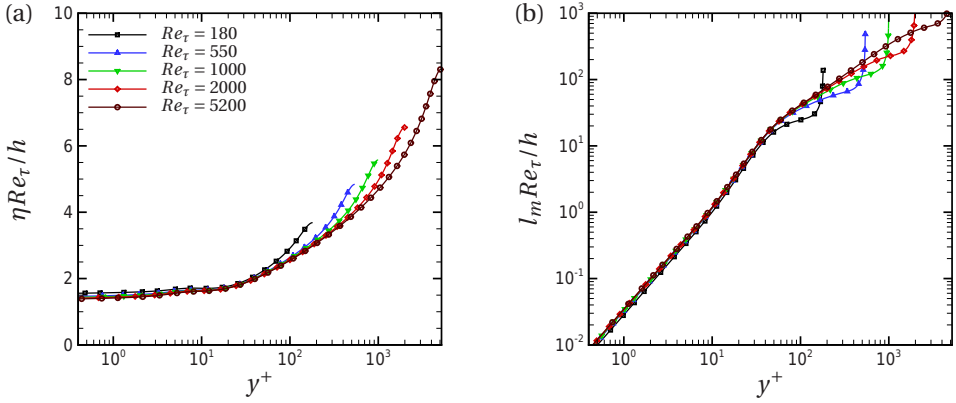
Figure 2.2: (a) Kolmogorov length scale and (b) mixing length, normalized by wall-based viscous length scales and plotted as a function of y^+ using data of constant property turbulent channel flow from Lee & Moser (2015).

the outer flow (Jiménez & Pinelli, 1999). According to Hamilton *et al.* (1995), the sustainment of near-wall turbulence involves a closed-loop mechanism whereby the generation of streaks are induced by quasi-streamwise vortices that are in turn created by streak instability. An alternate description of the self-sustaining mechanism has been provided by Chernyshenko & Baig (2005) in which the physical mechanism of streak formation is related to a combined action of wall-normal motions, mean shear and viscous diffusion. While there are differences in the interpretation of the self-sustaining process, a close relation between low-speed streaks and quasi-streamwise vortices is well-established (Robinson, 1991; Jeong *et al.*, 1997; Jiménez & Pinelli, 1999; Kim & Lim, 2000; Schoppa & Hussain, 2002) and also supported by self-sustaining mechanisms described by Hamilton *et al.* (1995) and Chernyshenko & Baig (2005).

VARIABLE PROPERTY WALL TURBULENCE

Near-wall turbulence for variable property flows has been far less explored compared to constant property flows. Most of the knowledge on variable property effects, have been obtained from experimental and numerical studies of supersonic air flow with adiabatic walls (e.g., Spina & Smits, 1987; Ringuette *et al.*, 2008; Elsinga *et al.*, 2010; Pirozzoli *et al.*, 2008; Lagha *et al.*, 2011*b*), and cooled or heated walls (e.g., Coleman *et al.*, 1995; Lechner *et al.*, 2001; Foysi *et al.*, 2004; Morinishi *et al.*, 2004; Duan *et al.*, 2010; Lagha *et al.*, 2011*a*; Shadloo *et al.*, 2015; Modesti & Pirozzoli, 2016). Experimental studies on supersonic boundary layer
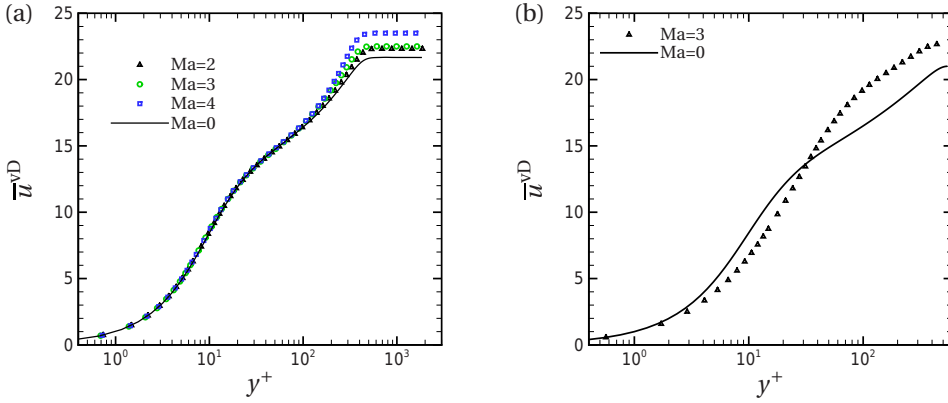
Figure 2.3: van Driest velocity $\overline{u}^{\mathrm{vD}}$ shown as a function of y^+ for (a) adiabatic supersonic boundary layers obtained from Pirozzoli & Bernardini (2011); Bernardini & Pirozzoli (2011), compared with reference boundary layer data from Jiménez *et al.* (2010) and (b) non-adiabatic supersonic channel flow obtained from Modesti & Pirozzoli (2016), compared with reference constant property data from Lee & Moser (2015).

structures are limited to investigate large-scale motions in the outer region of the flow, while numerical studies additionally allow a detailed investigation of near-wall structures. For supersonic flows, in addition to the Reynolds number, the Mach number and the associated changes in properties become additional parameters that characterize turbulent wall-bounded flows. In order to account for density variation, a modified velocity scale which uses wall shear stress and local mean density $\sqrt{\tau_w/\overline{\rho}}$ was first suggested by Morkovin (1962), such that

$$\sqrt{\frac{\overline{\rho}}{\tau_w}}u_i''\Bigg|_{\text{compressible BL}} \approx \sqrt{\frac{\rho_w}{\tau_w}}u_i'\Bigg|_{\text{incompressible BL}} \qquad (2.15)$$

Using Morkovin's hypothesis, past studies on supersonic flows over adiabatic walls have found that most of the differences with respect to the constant-property flow can be explained by simply accounting for the mean fluid property variations. By analysing supersonic boundary layer data, Morkovin also concluded that for moderate Mach numbers ($Ma < 5$), dilation is small and that the essential dynamics of these shear flows will follow the incompressible pattern (Smits & Dussauge, 2006). Over the course of time, the hypothesis has been extended and reformulated by several researchers. Bradshaw (1977) summarized Morkovin's hypothesis by stating that the direct effects of density fluctuations on

turbulence are small if the root-mean-square density fluctuation is small compared to the absolute density ($\rho'/\overline{\rho} \ll 1$). He also noted that the hypothesis in its general form does not include the effect of viscosity fluctuations and the effects of spatial gradients of mean density. Later, Coleman *et al.* (1995) investigated a supersonic channel flow using DNS with spatial gradients of properties and concluded that only mean property variations, but not property fluctuations, govern the turbulence structure. They argued that this fact reinforces Morkovin's hypothesis, as property fluctuations have a minor role on turbulence structure. A more contemporary definition of Morkovin's hypothesis, supplemented by past studies, is that- 'At moderate Mach numbers ($Ma < 5$) many of the differences seen between supersonic and constant property boundary layers, can be explained by simply accounting for the fluid property variations that accompany the temperature variation'- (Smits & Dussauge, 2006). Morkovin's hypothesis also forms the basis for the van Driest velocity transformation $\overline{u}^{\mathrm{vD}}$, which uses a density-weighted velocity scaling to collapse adiabatic supersonic boundary layer data with incompressible streamwise velocity profiles. $\overline{u}^{\mathrm{vD}}$ is defined as

$$\overline{u}^{\mathrm{vD}} = \int_0^{\overline{u}/u_\tau} \sqrt{\frac{\overline{\rho}}{\rho_w}} d\left(\frac{\overline{u}}{u_\tau}\right). \tag{2.16}$$

The van Driest transformed mean velocity $\overline{u}^{\mathrm{vD}}$, when plotted as a function of y^+, has been successful in collapsing velocity profiles of supersonic flows over adiabatic walls with velocity profiles from constant property flows (Guarini *et al.*, 2000; Maeder *et al.*, 2001; Pirozzoli & Bernardini, 2011; Lagha *et al.*, 2011*a*; Duan *et al.*, 2011). This can be seen in figure 2.3(a) which shows $\overline{u}^{\mathrm{vD}}$ plotted as a function of y^+ for data of adiabatic supersonic boundary layers from Pirozzoli & Bernardini (2011); Bernardini & Pirozzoli (2011) and compared with an incompressible boundary layer data from Jiménez *et al.* (2010). The compressible cases are with Mach numbers Ma=2, 3 and 4 and corresponding Reynolds numbers are Re_τ=450, 400 and 400, respectively. The incompressible boundary layer is at Re_τ=450. A good collapse of the velocity profile can be seen in the inner layer for all the cases. However, for non-adiabatic supersonic flows, $\overline{u}^{\mathrm{vD}}$ when plotted as a function of y^+, shows deviations if compared with profiles from constant property flows. For cooled walls, shrinking of the viscous sublayer (Duan *et al.*, 2010) and an outward shift of the log-law region with an increase in additive constant (Maeder, 2000) has been noted. This can be seen in figure 2.3(b) using data of compressible channel flow with cooled walls from Modesti & Pirozzoli (2016) at Ma=3 and Re_τ=450. The reference constant property channel flow data is from Lee & Moser (2015) at Re_τ=550. The van Driest transformation accounts for the changes in velocity scales by using a density-weighted transformation, but it assumes that the viscous length scale is similar to an incompressible boundary
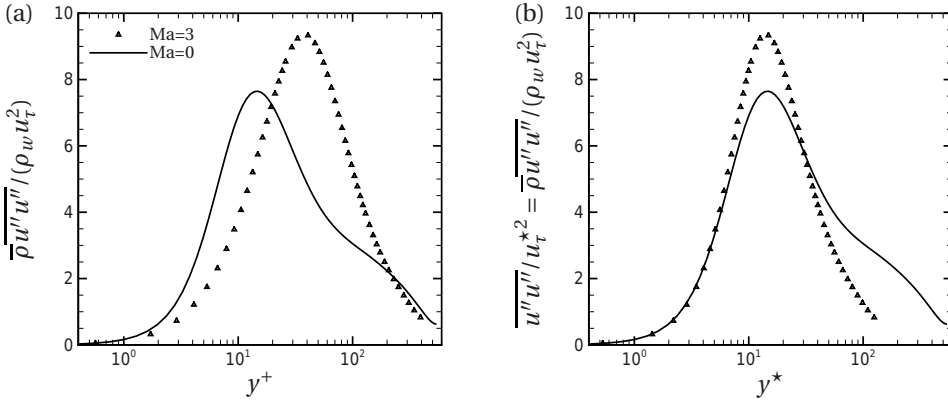
Figure 2.4: Streamwise Reynolds stress $\overline{\rho u'' u''}/(\rho_w u_\tau^2)$ shown as a function of (a) y^+ and (b) $y^\star$, using data of non-adiabatic supersonic channel flow obtained from Modesti & Pirozzoli (2016) and compared with reference constant property data from Lee & Moser (2015).

layer (Smits & Dussauge, 2006). This assumption of an invariant viscous length scale also affects the collapse of other turbulence statistics. An example of this can be seen in figure 2.4(a), which shows the streamwise Reynolds stress for both the compressible channel and constant property case discussed above. Apart from the differences in peak values, also the wall-normal location of the peak values change for the compressible case. Huang *et al.* (1995) proposed a semi-local scaling based on wall shear stress τ_w and local properties to improve the collapse of turbulence statistics in the near-wall region. Using the semi-local scaling the characteristic velocity and viscous length scale are given as $u_\tau^\star = \sqrt{\tau_w/\overline{\rho}}$ and $\delta_v^\star = \overline{\mu}/\overline{\rho} u_\tau^\star$, respectively. This leads to the semi-locally scaled wall distance $y^\star = y/\delta_v^\star$ and the corresponding semi-local Reynolds number $Re_\tau^\star = h/\delta_v^\star$. The improvement provided by the semi-local scaling is evident in figure 2.4(b), which shows that the wall-normal location of peak value of streamwise Reynolds stress now occurs at similar values. The semi-local scaling in a sense is an extension of Morkovin's hypothesis, the use of which in past literature was limited to account for changes in the velocity scale due to density changes. In a very recent study, Trettel & Larsson (2016) derived a velocity transformation that collapses the supersonic channel flows with cooled walls with the incompressible velocity profile. The transformation accounts for wall-normal density/viscosity gradients due to heat transfer and uses the semi-local wall coordinate $y^\star$.

For supersonic boundary layers with adiabatic walls, the dynamics of near-wall turbulent structures is found to be similar to constant property cases and its

characteristics scale well with the classical wall-based scaling (Ringuette *et al.*, 2008; Pirozzoli *et al.*, 2008; Lagha *et al.*, 2011*a*). For cooled walls the near-wall streaks extend in streamwise direction (Coleman *et al.*, 1995; Duan *et al.*, 2010; Lagha *et al.*, 2011*a*), while they shorten for heated walls (Lagha *et al.*, 2011*a*). These streak modifications were quantified in terms of wall-based viscous units. Morinishi *et al.* (2004) performed DNS of compressible turbulent channel flows between adiabatic and isothermal walls at a relatively low-Reynolds number of $Re_\tau = 150$. They showed that the near-wall velocity streaks for compressible turbulent flows do not become more coherent and are independent of thermal wall boundary conditions if semi-local units are used to compare with incompressible flows. Even though, the semi-local scaling is able to account for some of the differences seen between non-adiabatic variable and constant property flows, it has not been able to provide a universal scaling law. For instance, in a supersonic channel flow with cold isothermal walls, an increase in turbulence-to-mean time scale ratio was reported by Coleman *et al.* (1995) and a reduced pressure-strain rate resulting in an increased turbulence anisotropy was noted by Foysi *et al.* (2004). In a more recent study Modesti & Pirozzoli (2016) who performed DNS at different Reynolds and Mach numbers for compressible isothermal channel flows and used semi-local scaling noted an increase of streamwise turbulence intensity with Mach number as a dominant variable property effect.

While the semi-local scaling is nowadays being used more frequently, it has still not become a standard in the modern day variable property literature. One of the main reasons is the success of wall-based/classical scaling in supersonic flows with adiabatic walls. The use of a velocity and length scale that is itself a function of wall-distance is also a source of skepticism. This skepticism is further fueled by the fact that the semi-local scaling as proposed by Huang *et al.* (1995) was based purely on empirical basis and therefore lacks a theoretical framework. Additional research is necessary to establish a theoretical foundation for the use of semi-local scaling and to provide a physical explanation for changes in near-wall turbulence anisotropy that occur because of property gradients.

3

SEMI-LOCAL SCALING: THEORETICAL FRAMEWORK AND NUMERICAL EXPERIMENTS

3.1. IMPLICATION OF THE SEMI-LOCAL SCALING

As discussed in the previous chapter, the velocity and viscous length scale used to characterize the inner layer for constant property flows are given as

$$u_\tau = \sqrt{\frac{\tau_w}{\rho_w}} \quad \text{and} \quad \delta_v = \frac{\mu_w}{\rho_w u_\tau}, \tag{3.1}$$

respectively. The corresponding dimensionless wall coordinate and friction Reynolds number is then

$$y^+ = \frac{y}{\delta_v} \quad \text{and} \quad Re_\tau = \frac{h}{\delta_v} = \frac{\rho_w u_\tau h}{\mu_w}, \tag{3.2}$$

respectively. For variable property flows, the velocity and viscous length scale using semi-local scaling as proposed by Huang *et al.* (1995) is given as,

$$u_\tau^\star = \sqrt{\frac{\tau_w}{\overline{\rho}}} \quad \text{and} \quad \delta_v^\star = \frac{\overline{\mu}}{\overline{\rho} u_\tau^\star}, \tag{3.3}$$

respectively. The corresponding dimensionless semi-local wall coordinate and semi-local Reynolds number is then

$$y^\star = \frac{y}{\delta_v^\star} \quad \text{and} \quad Re_\tau^\star = \frac{h}{\delta_v^\star} = Re_\tau \frac{\sqrt{(\overline{\rho}/\rho_w)}}{(\overline{\mu}/\mu_w)}, \tag{3.4}$$

respectively.

For constant property wall-bounded turbulent flows in a given geometry, turbulence statistics are a unique function of wall-normal distance y/h and friction Reynolds number Re_τ, such that $\overline{u_i' u_j'}/u_\tau^2 = f(y/h, Re_\tau)$, where f is a generalized function and not known a priori. By applying the classical wall scaling in the inner-layer, the expression for the Reynolds stresses can be reduced to $\overline{u_i' u_j'}/u_\tau^2 \approx f(y^+)$. However, as stated in the previous chapter, no universal scaling with respect to Reynolds number exists (Morrison *et al.*, 2004; Hoyas & Jiménez, 2006). Therefore, it is more appropriate to write the Reynolds stresses as,

$$\overline{u_i' u_j'}/u_\tau^2 = f(y^+, Re_\tau). \tag{3.5}$$

For variable property wall-bounded turbulent flows, turbulence statistics for a given flow geometry not only depend on y/h and Re_τ, but also on the profile of density and viscosity. For moderate density and viscosity gradients the property

fluctuations are small and Morkovin's hypothesis holds, i.e., only mean property variations, but not thermodynamic fluctuations are important in turbulence dynamics (Coleman *et al.*, 1995). The expression for the Reynolds stresses can then be written as

$$\overline{\rho u_i'' u_j''}/\tau_w \approx f(y/h, Re_\tau, \overline{\rho}_p, \overline{\mu}_p). \tag{3.6}$$

Note, in the above equation $\overline{\rho}_p$ and $\overline{\mu}_p$ are the normalized mean profiles of density and viscosity over the complete channel cross-section. The semi-local scaling proposed by Huang *et al.* (1995) has been used in the past to account for mean property variations in the near-wall scaling of turbulence statistics for compressible flows when compared with isothermal cases. In the present work we investigate if the semi-local scaling can be used as a universal near-wall coordinate for flows with variable property effects. In other words, we assess if

$$\overline{\rho u_i'' u_j''}/\tau_w \approx f(y/h, Re_\tau^\star) \approx f(y^\star, Re_\tau^\star) \tag{3.7}$$

holds. Equation (3.7) implies that $Re_\tau^\star$ is sufficient to characterize near-wall turbulence dynamics. The validation of the above hypothesis will provide a strong support for the semi-local scaling as turbulence statistics at a given wall-normal position will depend only on the $Re_\tau^\star$ profile, thus providing a framework similar to constant property turbulence, wherein the dependence is only on Re_τ. In the following, streamwise, wall-normal, and spanwise directions are denoted as x,y, and z, respectively, while the corresponding velocity components are denoted as u, v, and w, respectively.

3.2. MATHEMATICAL SUPPORT FOR THE SEMI-LOCAL SCALING

In this section, we develop a mathematical foundation for the semi-local scaling that was suggested by Huang *et al.* (1995) using heuristic arguments. First, we propose to rescale the Navier-Stokes equations using semi-local quantities defined as

$$\hat{u}_i = \frac{u_i}{u_\tau^\star} = \left(\frac{u_i}{u_\tau}\right)\sqrt{\frac{\overline{\rho}}{\rho_w}}, \quad \hat{\rho} = \frac{\rho}{\overline{\rho}} = \left(\frac{\rho}{\rho_w}\right)\frac{\rho_w}{\overline{\rho}} = 1 + \frac{\rho'}{\overline{\rho}}, \quad \hat{\mu} = \frac{\mu}{\overline{\mu}} = \left(\frac{\mu}{\mu_w}\right)\frac{\mu_w}{\overline{\mu}} = 1 + \frac{\mu'}{\overline{\mu}},$$

$$\hat{x}_i = \left(\frac{x_i}{h}\right), \quad \hat{p} = \frac{p}{\overline{\rho} u_\tau^{\star 2}} = \left(\frac{p}{\rho_w u_\tau^2}\right). \tag{3.8}$$

The terms within brackets indicate the standard normalization used in equation (2.4). Using equation (3.8), the semi-locally scaled mass and momentum equations can be written as,

$$t_\tau^\star \frac{\partial \hat{\rho}}{\partial t} + \frac{\partial \hat{\rho} \hat{u}_j}{\partial \hat{x}_j} + \frac{\hat{\rho} \hat{v}}{2}\left(\frac{\rho_w}{\overline{\rho}}\right)\frac{\partial}{\partial \hat{y}}\left(\frac{\overline{\rho}}{\rho_w}\right) = 0, \tag{3.9}$$

$$t_\tau^\star \frac{\partial \hat{\rho}\hat{u}_i}{\partial t} + \frac{\partial \hat{\rho}\hat{u}_i\hat{u}_j}{\partial \hat{x}_j} = -\frac{\partial \hat{p}}{\partial \hat{x}_i} + \frac{\partial}{\partial \hat{x}_j}\left[\frac{\hat{\mu}}{Re_\tau^\star}\sqrt{\frac{\overline{\rho}}{\rho_w}}\left(\frac{\partial}{\partial \hat{x}_j}\left(\hat{u}_i\sqrt{\frac{\rho_w}{\overline{\rho}}}\right) + \frac{\partial}{\partial \hat{x}_i}\left(\hat{u}_j\sqrt{\frac{\rho_w}{\overline{\rho}}}\right)\right.\right.$$
$$\left.\left. -\frac{2\delta_{ij}}{3}\frac{\partial}{\partial \hat{x}_k}\left(\hat{u}_k\sqrt{\frac{\rho_w}{\overline{\rho}}}\right)\right)\right],$$
$$(3.10)$$

where $t_\tau^\star = h/u_\tau^\star$ is the corresponding time scale[1]. Next the equations (3.9) and (3.10) are used to derive the conservation equations for the mean and the fluctuating component of $\hat{u}_i$. But before doing so, we first discuss the influence of density fluctuations on turbulence statistics by highlighting the relation between Reynolds and Favre decomposition for a generic quantity γ as,

$$\overline{\gamma} = \tilde{\gamma} - \frac{\overline{\rho'\gamma'}}{\overline{\rho}}, \tag{3.11}$$

$$\gamma' = \gamma'' + \frac{\overline{\rho'\gamma'}}{\overline{\rho}}. \tag{3.12}$$

From Morkovin's hypothesis it is known that the direct effects of density fluctuations on turbulence are small if the root-mean-square density fluctuation is small compared with the absolute density (Bradshaw, 1977), i.e., $\sqrt{\rho'^2}/\overline{\rho} \ll 1$. Therefore, under the validity of Morkovin's hypothesis ($\sqrt{\rho'^2}/\overline{\rho} \ll 1$), any turbulence statistics resulting from density fluctuations should be insignificant in comparison to those obtained using mean density. This implies that the second term on the right hand side of equations (3.11) and (3.12) is insignificant. We assess this using the DNS data in section 3.4. The semi-locally scaled velocity components can then be related to the classically scaled velocity components as,

$$\frac{\overline{u}}{u_\tau} \approx \tilde{u}\sqrt{\frac{\rho_w}{\overline{\rho}}} = \frac{\tilde{u}}{u_\tau}, \quad \frac{\overline{v}}{u_\tau} \approx \tilde{v}\sqrt{\frac{\rho_w}{\overline{\rho}}} = \frac{\tilde{v}}{u_\tau} = 0, \quad \frac{\overline{w}}{u_\tau} \approx \tilde{w}\sqrt{\frac{\rho_w}{\overline{\rho}}} = \frac{\tilde{w}}{u_\tau} = 0,$$

$$\frac{u'}{u_\tau} \approx \hat{u}''\sqrt{\frac{\rho_w}{\overline{\rho}}} = \frac{u''}{u_\tau}, \quad \frac{v'}{u_\tau} \approx \hat{v}''\sqrt{\frac{\rho_w}{\overline{\rho}}} = \frac{v''}{u_\tau}, \quad \frac{w'}{u_\tau} \approx \hat{w}''\sqrt{\frac{\rho_w}{\overline{\rho}}} = \frac{w''}{u_\tau}. \tag{3.13}$$

Note that for a fully developed turbulent channel flow $\tilde{v} = \tilde{w} = 0$. Next the Reynolds decomposition of density and viscosity can be written, using equation (3.8) as:

$$\overline{\hat{\rho}} = 1, \quad \hat{\rho}' = \frac{\rho'}{\overline{\rho}}, \quad \overline{\hat{\mu}} = 1, \quad \hat{\mu}' = \frac{\mu'}{\overline{\mu}}. \tag{3.14}$$

---

[1]The time derivative in Patel *et al.* (2015) was written as $\frac{\partial}{\partial \hat{t}} (= t_\tau^\star \frac{\partial}{\partial t})$, with $\hat{t} = t/t_\tau^\star$. However, since the equations were derived by using variables as a function of space independent time coordinate t, it is more appropriate to write the time derivative as $t_\tau^\star \frac{\partial}{\partial t}$ in order to clarify the functional dependence.

Assuming relatively small viscosity fluctuations ($\hat{\mu}' = \mu'/\overline{\mu} \ll 1$), the Reynolds-averaged continuity and momentum equations are simplified to

$$\frac{\partial \widetilde{u}_j}{\partial \hat{x}_j} = 0, \tag{3.15}$$

$$\frac{\partial \widehat{\widetilde{u}_i'' \widetilde{v}''}}{\partial \hat{y}} \approx -\frac{\partial \overline{p}}{\partial \hat{x}_i} + \frac{\partial}{\partial \hat{y}} \left[\frac{1}{Re_\tau^\star} \sqrt{\frac{\overline{\rho}}{\rho_w}} \frac{\partial}{\partial \hat{y}} \left(\widetilde{u}_i \sqrt{\frac{\rho_w}{\overline{\rho}}} \right) \right]. \tag{3.16}$$

Substituting $\overline{\widetilde{u}}_i$ from equation (3.13) back into equation (3.16) we can write the mean streamwise momentum equation as

$$\frac{\partial \widehat{\widetilde{u}'' \widetilde{v}''}}{\partial y} \approx -\frac{\partial \overline{p}}{\partial x} + \frac{\partial}{\partial y} \left[\frac{1}{Re_\tau^\star} \sqrt{\frac{\overline{\rho}}{\rho_w}} \frac{\partial}{\partial y} \left(\frac{\overline{u}}{u_\tau} \right) \right], \tag{3.17}$$

where $\widehat{\widetilde{u}'' \widetilde{v}''} = \overline{\rho u'' v''}/\tau_w$. Note that the above equation has been obtained, without making any assumption on density fluctuations and only neglecting the viscosity fluctuations.

The term $\sqrt{\overline{\rho}/\rho_w}\, \partial(\overline{u}/u_\tau)$, in equation (3.17) can be expressed as the van Driest transformed velocity with

$$\partial \overline{u}^{\mathrm{vD}} = \sqrt{\frac{\overline{\rho}}{\rho_w}}\, \partial \left(\frac{\overline{u}}{u_\tau} \right). \tag{3.18}$$

Thus, the turbulent shear stress and the mean velocity profile are related through

$$\frac{\partial \widehat{\widetilde{u}'' \widetilde{v}''}}{\partial y} \approx -\frac{\partial \overline{p}}{\partial x} + \frac{\partial}{\partial y} \left(\frac{1}{Re_\tau^\star} \frac{\partial \overline{u}^{\mathrm{vD}}}{\partial y} \right). \tag{3.19}$$

The only governing parameter in this relation is the semi-local scaling parameter $Re_\tau^\star$. Therefore if the hypothesis stated in section 3.1 holds, flows with similar $Re_\tau^\star$ profiles will result in similar van Driest transformed velocity and turbulent shear stress profiles. Similarly, the mean wall-normal momentum equation gives the relation between pressure and wall-normal Reynolds stress as

$$\widehat{\widetilde{v}'' \widetilde{v}''} \approx -\overline{p} + \mathrm{constant} \tag{3.20}$$

The conservation equations for the fluctuating velocity components are derived next to relate second order turbulence statistics with the van Driest velocity and $Re_\tau^\star$ profiles. Assuming relatively small density and viscosity fluctuations

($\hat{\rho}' = \rho'/\overline{\rho} \ll 1$ and $\hat{\mu}' = \mu'/\overline{\mu} \ll 1$) such that both $\hat{\rho} \to 1$ and $\hat{\mu} \to 1$, we obtain the continuity and momentum equations for $\hat{u}_i''$ as,

$$\frac{\partial \hat{u}_j''}{\partial \hat{x}_j} + \frac{\hat{v}''}{2}\left(\frac{\rho_w}{\overline{\rho}}\right)\frac{\partial}{\partial \hat{y}}\left(\frac{\overline{\rho}}{\rho_w}\right) \approx 0, \tag{3.21}$$

$$t_\tau^\star \frac{\partial \hat{u}_i''}{\partial t} + \frac{\partial \hat{u}_i'' \hat{u}_j''}{\partial \hat{x}_j} + \hat{v}''\frac{\partial \tilde{u}^{\mathrm{vD}}}{\partial \hat{y}}\delta_{i1} + \tilde{\hat{u}}_j\frac{\partial \hat{u}_i''}{\partial \hat{x}_j} \approx -\frac{\partial \hat{p}'}{\partial \hat{x}_i} + \frac{\partial \widetilde{\hat{u}_i'' \hat{u}_j''}}{\partial \hat{x}_j} + \frac{\partial}{\partial \hat{x}_j}\left(\hat{\tau}_{ij}' - \hat{D}_{ij}\right), \tag{3.22}$$

with

$$\begin{aligned}
\hat{\tau}_{ij}' &= \frac{1}{Re_\tau^\star}\left[\left(\frac{\partial \hat{u}_i'}{\partial \hat{x}_j} + \frac{\partial \hat{u}_j'}{\partial \hat{x}_i}\right) - \frac{2}{3}\frac{\partial \hat{u}_k'}{\partial \hat{x}_k}\delta_{ij}\right] \quad \text{and} \\
\hat{D}_{ij} &= \frac{1}{Re_\tau^\star}\left(\frac{\rho_w}{\overline{\rho}}\right)\left[\frac{\hat{u}_i'}{2}\frac{\partial}{\partial \hat{x}_j}\left(\frac{\overline{\rho}}{\rho_w}\right) + \frac{\hat{u}_j'}{2}\frac{\partial}{\partial \hat{x}_i}\left(\frac{\overline{\rho}}{\rho_w}\right) - \delta_{ij}\frac{\hat{v}'}{3}\frac{\partial}{\partial \hat{y}}\left(\frac{\overline{\rho}}{\rho_w}\right)\right].
\end{aligned}$$

For a detailed derivation see appendix A.

This relation can further be used to derive the transport equations for the second order turbulence statistics[2]. Thus, analysing equation (3.22) can shed light on the scaling properties of Reynolds stresses, which are not evident from the averaged momentum equations. If equation (3.22) is compared with the analogous equation for constant property turbulent flows, three differences can be seen: 1) the third term (production term in the transport equations for the second order turbulence statistics) is governed by the gradient of the van Driest velocity $\overline{u}^{\mathrm{vD}}$ instead of $\overline{u}/u_\tau$ as in constant property flows, 2) instead of Re_τ the semi-local Reynolds number $Re_\tau^\star$ governs the scaling of the viscous term (turbulence dissipation) within the first spatial derivative, and 3) an additional term $\hat{D}_{ij}$ appears that is related to the wall-normal gradient of mean density. Scaling arguments can be used to estimate the ratio of $\hat{S}_{ij}'$ and $\hat{D}_{ij}$. Following Tennekes & Lumley (1972) with Λ as the Taylor length scale, these terms can be estimated as $\hat{S}_{ij}' \approx \mathcal{O}\left(\overline{u}/\Lambda\right)$ and $\hat{D}_{ij} \approx \mathcal{O}\left(\overline{u}/h\right)$. The ratio is then $\hat{S}_{ij}'/D_{ij} \approx \mathcal{O}\left(h/\Lambda\right)$, which is far larger than unity for highly turbulent flows, and thus $\hat{D}_{ij}$ plays a minor role on the evolution of turbulent fluctuations. Now, it can be seen that also for equation (3.22) the governing parameter is $Re_\tau^\star$ (in equation (3.19) we showed that

---

[2]The transport equation for turbulence kinetic energy is derived in Chapter 7. There it can be seen that the present rescaling framework also allows to retain density fluctuations in the terms using Favre averaging (similar to the mean momentum equation (3.16)). Since instantaneous/fluctuation equation does not involve any averaging operations, assuming $\hat{\rho} \to 1$ provides a first order approximation.

$\overline{u}^{\text{vD}}$ is governed by $Re_\tau^\star$) and therefore it can be hypothesized that the second order turbulence statistics also depend on the $Re_\tau^\star$ profile only. This allows several conclusions. For example, given a turbulent flow with variable density and viscosity, such that $Re_\tau^\star$ is constant, the van Driest velocity profile $\overline{u}^{\text{vD}}$ and the second order turbulence statistics $\widehat{u_i'' u_j''} = \overline{\rho u_i'' u_j''}/\tau_w$ will overlap with the mean velocity $\overline{u}/u_\tau$ and turbulence statistics $\overline{u_i' u_j'}/u_\tau^2$ from a constant property turbulent flow. Furthermore, similar turbulence statistics and van Driest velocity profiles will be obtained for cases with similar $Re_\tau^\star$ profiles, even if their density and viscosity profiles substantially differ. Or more general, turbulent flows with similar $Re_\tau^\star$ profiles will give similar turbulence statistics, provided Morkovin's hypothesis and $\hat{\mu}' \ll 1$ are not invalidated. This hypothesis will be tested by means of numerical experiments outlined in the next section.

3.3. NUMERICAL EXPERIMENTS

3.3.1. COMPUTATIONAL DETAILS

Direct numerical simulations of fully developed turbulent channel flows are performed using the low Mach number approximation of the Navier–Stokes equations given by equations (2.1)-(2.3), without the influence of buoyancy. In the low Mach number limit, the density and transport properties can be evaluated as a function of temperature only, independent of pressure fluctuations (Majda & Sethian, 1985; Nemati *et al.*, 2015). In order to achieve variations in temperature T, and consequently in thermophysical properties, the flow is uniformly heated with a volumetric heat source ϕ, while the temperature at both channel walls is kept constant. This allows a wall heat flux and ensures that the flow is in thermal equilibrium. In this manner, the symmetry of the mean flow is maintained and the Reynolds number Re_τ is constant with respect to property variations. This forms the basis for an ideal setup to study turbulence modification due to variable properties, and to compare scaling laws with isothermal flows, as compared to a case where the bottom and top walls are at different temperatures and therefore at different Reynolds numbers (Nicoud & Poinsot, 1999; Zonta *et al.*, 2012). The flow is driven by a constant streamwise pressure gradient $\partial \overline{p}/\partial x$. The relation between $\partial \overline{p}/\partial x$ and mean wall shear stress τ_w can be obtained using force balance (see for e.g. Pope, 2000) along the streamwise direction and is given as,

$$-\frac{\partial \overline{p}}{\partial x} = \frac{\tau_w}{h} \frac{h}{\rho_w u_\tau^2} = 1 \tag{3.23}$$

Note, because of the symmetry of the flow, both walls have the same τ_w.

The present study uses a Cartesian version of a code that was initially developed in cylindrical coordinates for DNS of turbulent heat transfer to fluids at supercritical pressure in an annulus by Peeters (2016) . The DNS code discretises the spatial derivatives in wall-normal direction using a sixth order staggered compact finite difference scheme (Lele, 1992; Boersma, 2011) and the derivatives in homogeneous directions (spanwise and streamwise) are computed using a Fourier expansion with periodic boundary conditions. To avoid aliasing errors, the advection terms in homogeneous directions are discretized with a quasi-skew-symmetric formulation. The equations are integrated in time using the second order Adams-Bashforth method. The pressure correction scheme is based on the projection method (McMurtry *et al.*, 1986). The validation of the numerical approach is discussed in appendix B.

3.3.2. CASE DESCRIPTION

Density and viscosity that appear in the mass and momentum equations are directly responsible for influencing the turbulent motions. Other properties like the thermal conductivity which affects only the scalar equation, influences the turbulence only in an indirect way by modifying the density and viscosity distribution. Therefore, in order to study and characterize the influence of variable properties on turbulence we first focus on cases with different constitutive relations for density and viscosity. Other transport properties like thermal conductivity λ and specific heat c_p are constant in all simulations. The Prandtl number Pr_w based on wall quantities is taken to be unity for all cases. Eleven cases have been simulated and are summarised in table 3.1. The simulations consist of three constant property (CP395, CP150, CP550) and eight variable property cases (CRe$_\tau^\star$, SRe$_{\tau GL}^\star$, GL, LL, SRe$_{\tau LL}^\star$, SRe$_{\tau Cv}^\star$, Cv, LL2). The acronym CP refers to a constant property case; CRe$_\tau^\star$ refers to a variable property case with constant $Re_\tau^\star$ (= 395) across the whole channel. This is achieved with ρ and μ being proportional to $1/T$ and $\sqrt{1/T}$, respectively. Such a behavior can qualitatively occur in fluids at supercritical pressures close to the pseudo-critical point; both ρ and μ decrease with increase of temperature (Nemati *et al.*, 2015; Peeters *et al.*, 2016). GL corresponds to a gas-like property variation, whereby ρ decreases and μ increases with increase of T. LL corresponds to a liquid-like behavior as μ deceases with increase of T, two liquid-like cases LL and LL2 are simulated, case LL and LL2 have a Re_τ of 150 and 395, respectively. Cv refers to a constant kinematic viscosity ν case with $\rho(T) = \mu(T)$. Finally, SRe$_{\tau GL}^\star$, SRe$_{\tau LL}^\star$ and SRe$_{\tau Cv}^\star$ are hypothetical cases that resemble similar $Re_\tau^\star$ profiles as cases GL, LL and Cv, respectively, but with different functional relations for ρ and μ. The functional relations for ρ/ρ_w and μ/μ_w as a function of T/T_w are shown in the second and

Case	ρ/ρ_w	μ/μ_w	Re_τ	$Re_{\tau\,c}^\star$	ϕ
CP395	1	1	395	395	0
$CRe_\tau^\star$	$(T/T_w)^{-1}$	$(T/T_w)^{-0.5}$	395	395	17.55
$SRe_{\tau GL}^\star$	1	$(T/T_w)^{1.2}$	395	152	18.55
GL	$(T/T_w)^{-1}$	$(T/T_w)^{0.7}$	395	142	17.55
LL	1	$(T/T_w)^{-1}$	150	543	29
$SRe_{\tau LL}^\star$	$(T/T_w)^{0.6}$	$(T/T_w)^{-0.75}$	150	535	31.5
$SRe_{\tau Cv}^\star$	1	$(T/T_w)^{-0.5}$	395	532	17.55
Cv	$(T/T_w)^{-1}$	$(T/T_w)^{-1}$	395	538	16
LL2	1	$(T/T_w)^{-1}$	395	703	17.55
CP150	1	1	150	150	0
CP550	1	1	550	550	0

Table 3.1: Simulation parameters for all cases. CP395 - constant property case with $Re_\tau = 395$; $CRe_\tau^\star$ - variable property case with constant $Re_\tau^\star$ (= 395) across the channel; GL - case with gas-like property variations; $SRe_{\tau GL}^\star$ - variable property case with $Re_\tau^\star$ similar to case GL; LL - case with liquid-like property variations and $Re_\tau = 150$; $SRe_{\tau LL}^\star$ - variable property case with $Re_\tau^\star$ similar to case LL; Cv - variable property case with constant kinematic viscosity v; $SRe_{\tau Cv}^\star$ - variable property case with $Re_\tau^\star$ similar to case Cv; LL2 -case with liquid-like property variations and $Re_\tau = 395$; CP150 - constant property case with $Re_\tau = 150$; CP550 - constant property case with $Re_\tau = 550$.

third column of table 3.1. The next two columns report the wall-based friction Reynolds number Re_τ, and the semi-local Reynolds number at the channel centre $Re_{\tau\,c}^\star = Re_\tau \sqrt{(\overline{\rho}_c/\rho_w)}/(\overline{\mu}_c/\mu_w)$ (subscript c denotes the value at channel centre). Note, at the wall $Re_{\tau\,w}^\star = Re_\tau$. The last column reports the value of volumetric heat source term ϕ used in the energy equation (2.3). The value of ϕ is chosen such that strong variations in properties occur, but without considerably invalidating Morkovin's hypothesis.

Figure 3.1 shows the distributions of density, viscosity and $Re_\tau^\star$ for all cases. Cases with variable density are shown as lines and cases with constant density are shown as symbols. As can be seen, we use different combinations of ρ and μ to obtain quasi-similar $Re_\tau^\star$ profiles (symbols and lines with same colour). Note, the strongest gradients in $Re_\tau^\star$ occur at the wall. The cases forming the first pair – CP395 and $CRe_\tau^\star$ (black symbols and line, respectively) – have constant $Re_\tau^\star$ in wall-normal direction ($dRe_\tau^\star/dy = 0$), even though for case $CRe_\tau^\star$ the density and viscosity are varying and decrease away from the wall. For the second pair
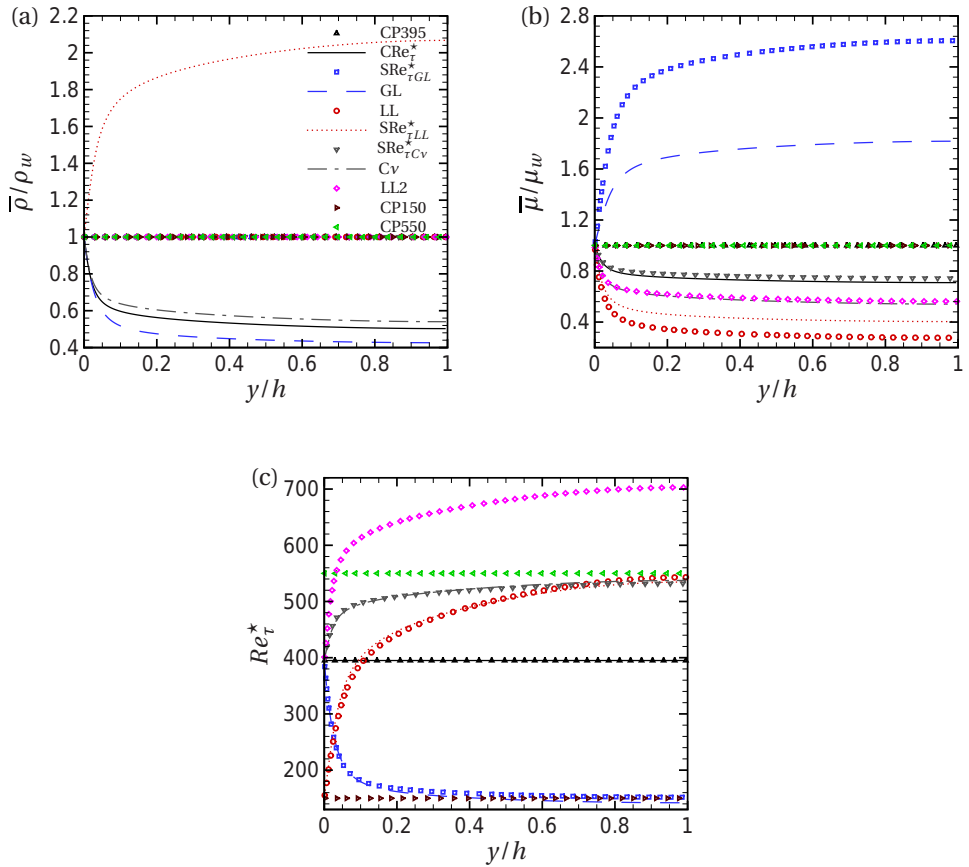
Figure 3.1: (a) Density $\overline{\rho}/\rho_w$, (b) viscosity $\overline{\mu}/\mu_w$, and (c) semi-local Reynolds number $Re_\tau^\star$ as a function of wall-normal distance y/h.
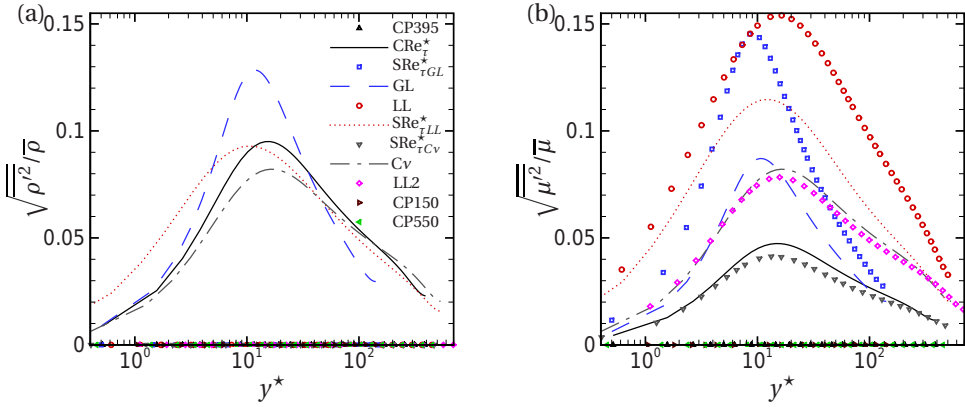
Figure 3.2: (a) Relative density fluctuations $\sqrt{\overline{\rho'^2}}/\overline{\rho}$ and (b) relative viscosity fluctuations $\sqrt{\overline{\mu'^2}}/\overline{\mu}$ as a function of semi-local wall coordinate $y^\star$.

– $\text{SRe}^\star_{\tau GL}$ and GL (blue symbols and line, respectively) – the profile for $Re^\star_\tau$ decreases from 395 at the wall to approximately 150 at the channel centre. Later, we will denote these cases as $dRe^\star_\tau/dy < 0$. For the third pair – LL and $\text{SRe}^\star_{\tau LL}$ (red symbols and line, respectively) – $Re^\star_\tau$ increases from 150 at the wall to approximately 540 at the channel centre. For the fourth pair – $\text{SRe}^\star_{\tau Cv}$ and Cv (grey symbols and line, respectively) – $Re^\star_\tau$ increases from 395 at the wall to approximately 540 at the channel centre. For case LL2 the $Re^\star_\tau$ increases from 395 at the wall to approximately 700 at the channel centre. The third and fourth pair, along with case LL2, will be referred to as $dRe^\star_\tau/dy > 0$. The simulations CP150 (brown symbol) and CP550 (green symbol) are cases that bound the $Re^\star_\tau$ profiles of the variable property cases (except case LL2) in order to investigate and distinguish any Reynolds number effects with respect to effects caused by property gradients. Considerable variations in properties have been obtained for all variable property cases. However, the relative property fluctuations $\rho'_{rms}/\overline{\rho}$ and $\mu'_{rms}/\overline{\mu}$ (the subscript rms indicates the root mean square value) are still not more than 0.15 for all variable property cases as can be seen in figure 3.2.

Table 3.2 provides details on the computational box size and also shows the corresponding resolutions in terms of conventional wall scaling (Δx^+, Δy^+_w, Δz^+) and semi-local scaling at the channel centre ($\Delta x^\star_c$, $\Delta y^\star_c$, $\Delta z^\star_c$). For constant property cases reporting the mesh spacing in terms of + units is well established, since the smallest values of Kolmogorov length scale occur in the near-wall region and are known to scale well in classical wall-based scaling (see figure 2.2(a)). For vari-
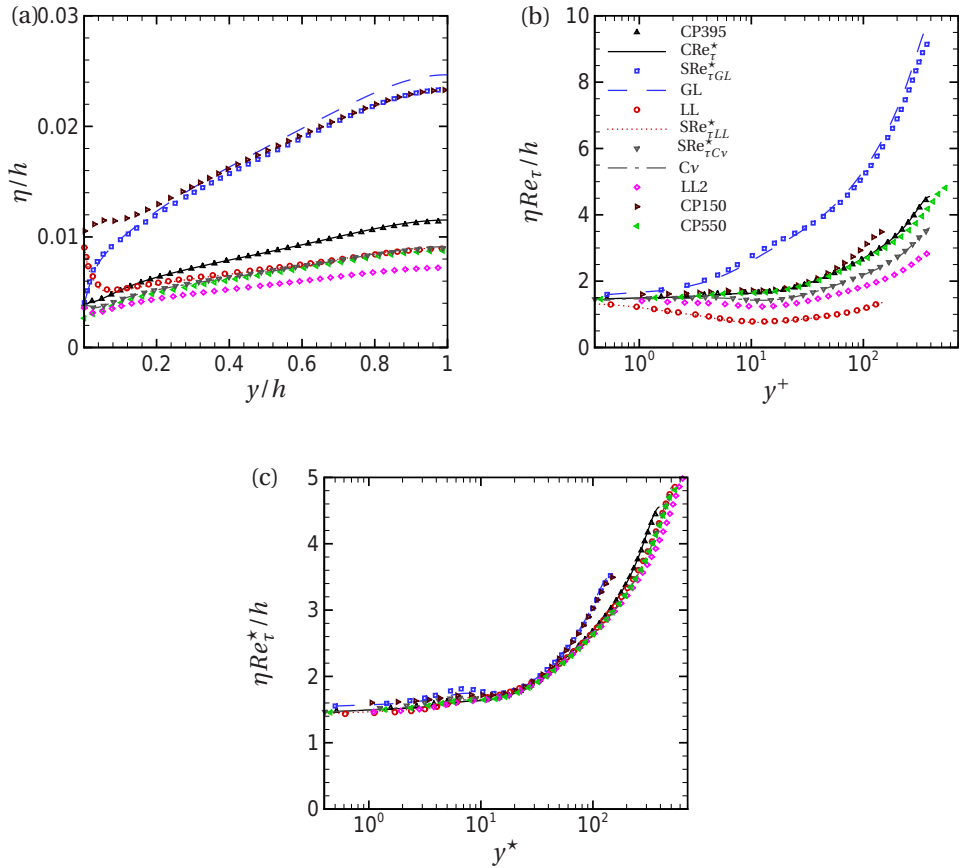
Figure 3.3: Kolmogorov length scale normalized by and plotted using, (a) outer scales, (b) wall-based viscous length scales and (c) semi-local viscous length scales.

Case	$L_x \times L_y \times L_z$	Δx^+	Δy_w^+	Δz^+	$\Delta x_c^\star$	$\Delta y^\star_c$	$\Delta z^\star_c$
CP395	$2\pi h \times 2h \times \pi h$	10.34	1.03	5.17	10.34	4.01	5.17
$\mathrm{CRe}_\tau^\star$	$2\pi h \times 2h \times \pi h$	10.34	1.03	5.17	10.34	4.01	5.17
$\mathrm{SRe}_{\tau GL}^\star$	$5\pi h \times 2h \times 2\pi h$	17.23	1.03	6.89	6.63	1.54	2.65
GL	$5\pi h \times 2h \times 2\pi h$	17.23	1.03	6.89	6.20	1.44	2.48
LL	$3\pi h \times 2h \times 1.5\pi h$	3.92	0.36	1.96	14.19	5.55	7.09
$\mathrm{SRe}_{\tau LL}^\star$	$3\pi h \times 2h \times 1.5\pi h$	3.92	0.36	1.96	13.98	5.47	6.99
$\mathrm{SRe}_{\tau Cv}^\star$	$2\pi h \times 2h \times \pi h$	10.34	0.80	5.17	13.92	4.61	6.96
Cv	$2\pi h \times 2h \times \pi h$	10.34	0.80	5.17	14.08	4.66	7.04
LL2	$2\pi h \times 2h \times \pi h$	6.89	0.69	3.45	12.27	5.28	6.13
CP150	$5\pi h \times 2h \times 2\pi h$	12.26	0.69	4.9	12.26	2.36	4.9
CP550	$2\pi h \times 2h \times \pi h$	11.07	0.9	5.53	11.07	4.81	5.53

Table 3.2: Mesh resolution for all cases.

able property cases, determining the mesh resolutions using + units alone is not adequate and therefore we also report resolution based on semi-local scaling at channel centre. These serve as a useful measure for evaluating mesh adequacy for cases with a monotonic $Re_\tau^\star$ profile. This fact can be appreciated by studying the scaling characteristics of Kolmogorov length scales, $\eta = ((\overline{\mu}/\overline{\rho})^3 \overline{\rho}/\epsilon)^{0.25}$ (ϵ is the turbulence kinetic energy dissipation per unit volume). Figure 3.3 shows η, normalized by, and plotted as a function of outer scales (figure 3.3(a)), wall-based viscous length scales (figure 3.3(b)) and semi-local viscous length scales (figure 3.3(c)) for all cases. Cases with similar $Re_\tau^\star$ profiles show similar distributions of Kolmogorov scales, indicating that the smallest scales are strongly governed by $Re_\tau^\star$ profiles. The Kolmogorov scale normalized using the half-channel height increases for cases with decreasing $Re_\tau^\star$, while it decreases for cases with increasing $Re_\tau^\star$. The cases with $dRe_\tau^\star/dy < 0$, for which $Re_\tau^\star$ varies from 395 at the wall to approximately 140 at the channel centre, have a Kolmogorov length scale that transitions from values of case CP395 at the wall to CP150 at the channel centre. A similar observation can be made for cases with $dRe_\tau^\star/dy > 0$. The Kolmogorov scale, when normalized by and plotted as a function of classical wall-based viscous units, shows strong deviations away from the wall for cases with $dRe_\tau^\star/dy \neq 0$. On the other hand, using semi-local length scales provides a good collapse of η for all cases in the near-wall region. Hence, the semi-local scaling also provides a good measure to assess the mesh spacing requirements for simulations with strong fluid property variations. Table 3.3 lists the maximum grid spacing in terms of η for all cases, and the values are within the resolution re-

Case	$(\Delta x/\eta)_{max}$	$(\Delta(y)_{min}/\eta)_{max}$	$(\Delta(y)_{max}/\eta)_{max}$	$(\Delta z/\eta)_{max}$
CP395	6.98	0.69	0.89	3.49
$CRe_\tau^\star$	7	0.7	0.88	3.5
$SRe_{\tau GL}^\star$	10.78	0.64	0.43	4.31
GL	10.8	0.64	0.41	4.3
LL	5.02	0.27	1.15	2.51
$SRe_{\tau LL}^\star$	5.18	0.27	1.14	2.59
$SRe_{\tau Cv}^\star$	7.11	0.55	0.96	3.55
Cv	7.11	0.55	0.95	3.57
LL2	5.6	0.68	1.04	2.8
CP150	7.76	0.44	0.68	3.55
CP550	7.6	0.62	1	3.8

Table 3.3: Maximum spatial resolution normalized using the Kolmogorov scale η.

quirements of $\Delta x < 12\eta$, $\Delta y < 2\eta$, $\Delta z < 6\eta$, as also reported in other DNS studies (Zonta *et al.*, 2012; Lee *et al.*, 2013).

The adequacy of the box size to accommodate the large-scale structures can be studied using the one-dimenisonal pre-multiplied energy spectra, defined as

$$\phi_{\rho u'' u''}(k_\alpha) = k_\alpha \left[\mathscr{F}\left(\sqrt{\rho} u''\right) \mathscr{F}\left(\sqrt{\rho} u''\right)^* \right] = k_\alpha \left[E_{\rho u'' u''}(k_\alpha) \right]. \tag{3.24}$$

In the above equation, $\mathscr{F}(\psi)$ is the Fourier coefficient of ψ, $\mathscr{F}(\psi)^*$ is the complex conjugate, $E_{\rho u'' u''} = \mathscr{F}\left(\sqrt{\rho} u''\right) \mathscr{F}\left(\sqrt{\rho} u''\right)^*$ represents the energy spectra of the density weighted streamwise velocity fluctuation and k_α is the wavenumber in streamwise k_x or spanwise k_z direction. The streamwise Reynolds stress is related to $\phi_{\rho u'' u''}$ and $E_{\rho u'' u''}$ as

$$\overline{\rho u'' u''} = \overline{\rho \widetilde{u'' u''}} = \int_0^\infty E_{\rho u'' u''}(k_\alpha)\, \mathrm{d}k_\alpha = \int_0^\infty \phi_{\rho u'' u''}(k_\alpha)\, \mathrm{d}\left(\log \lambda_\alpha\right), \tag{3.25}$$

where $\lambda_\alpha = 2\pi/k_\alpha$ is the wavelength. The area under the pre-multiplied spectra, when plotted in lin-log scale, represents the Reynolds stress. A plot of $\phi_{\rho u'' u''}$, normalised by $\overline{\rho u'' u''}$ and plotted as a function of streamwise and spanwise wavelength at different wall-normal planes, is shown in figure 3.4. While the spanwise spectra indicates that the spanwise box size is sufficient, it can be argued that the length of the box in streamwise direction could be increased to resolve all the large-scale contributions. However, as noted in previous studies
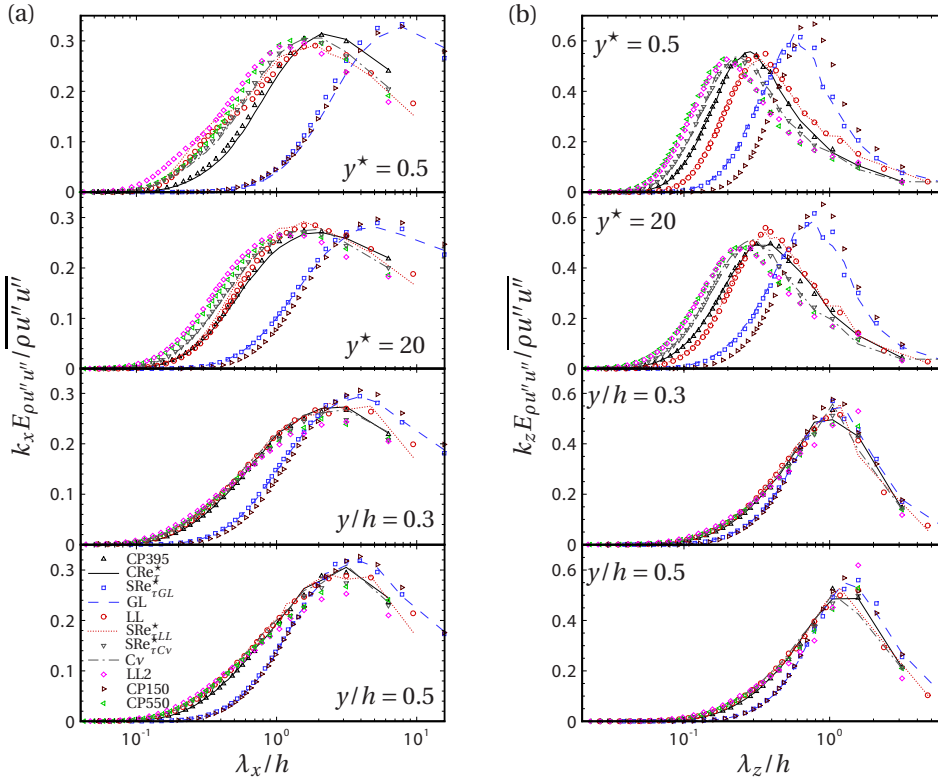
Figure 3.4: (a) Normalised pre-multiplied streamwise spectra $k_x E_{\rho u'' u''}/\overline{\rho u'' u''}$ as a function of streamwise wavelength λ_x/h and (b) normalised pre-multiplied spanwise spectra $k_z E_{\rho u'' u''}/\overline{\rho u'' u''}$ as a function of spanwise wavelength λ_z/h, at different wall-normal locations.

(Abe *et al.*, 2004; Lozano-Durán & Jiménez, 2014) the influence of these un-resolved large scales structures (due to the moderate box size) on turbulence statistics is negligible, and resolving the peak of the streamwise pre-multiplied spectra (e.g. DNS data of Moser *et al.* (1999)) is considered sufficient for the present work.

3.4. TURBULENCE STATISTICS

In this section, we assess the arguments made in section 3.1 and 3.2 using the DNS results for three quasi-similar $Re_\tau^\star$ pairs. The validity of Morkovin's hypothesis, which was used in section 3.2 to develop the theoretical framework, is also assessed. The cases forming the first pair – CP395 and $CRe_\tau^\star$ – have constant $Re_\tau^\star$

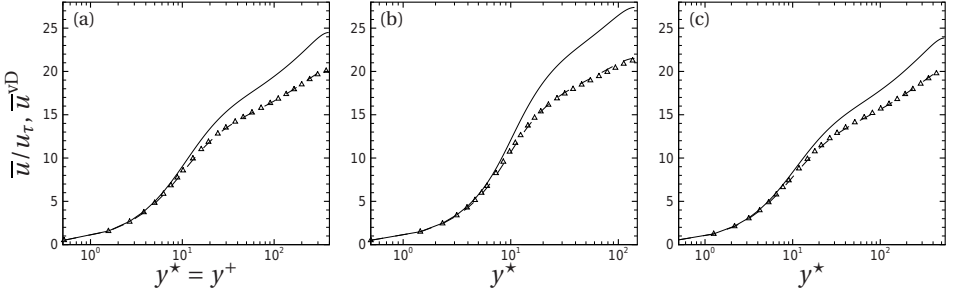Figure 3.5: Averaged velocity profiles for cases (a) CP395 and $CRe_\tau^\star$, (b) $SRe_{\tau GL}^\star$ and GL, (c) $SRe_{\tau Cv}^\star$ and Cv. Symbols are constant density cases: CP395, $SRe_{\tau GL}^\star$ and $SRe_{\tau Cv}^\star$, lines are variable density cases: $CRe_\tau^\star$, GL and Cv. (——) mean streamwise velocity $\overline{u}/u_\tau$ and (– – –) van Driest transformed streamwise velocity profile $\overline{u}^{vD}$.

in wall-normal direction, even though for case $CRe_\tau^\star$ the density and viscosity are varying and decrease away from the wall. For the second pair – $SRe_{\tau GL}^\star$ and GL – the profile for $Re_\tau^\star$ decreases from 395 at the wall to approximately 150 at the channel centre. For the third pair – $SRe_{\tau Cv}^\star$ and Cv – $Re_\tau^\star$ increases from 395 at the wall to approximately 540 at the channel centre.

Based on the equation (3.19) three quasi-similar $Re_\tau^\star$ pairs are assessed for quasi-similarity of van Driest transformed streamwise velocity profile $\overline{u}^{vD}$ and the Reynolds shear stress $\overline{\rho u'' v''}/\tau_w$. The comparison of $\overline{u}^{vD}$ is shown in figure 3.5. The solid line indicates the streamwise velocity profile for variable density cases ($CRe_\tau^\star$, GL and Cv), while the dashed line represents their corresponding van Driest transformed streamwise velocity profile. $\overline{u}^{vD}$ overlaps with the velocity from the corresponding quasi-similar $Re_\tau^\star$ cases (symbols) with constant density (CP395, $SRe_{\tau GL}^\star$ and $SRe_{\tau Cv}^\star$). The comparison of the Reynolds shear stress is shown in figure 3.6(a)-3.6(c) also showing a good collapse. A comparison of other second order statistics, namely normal Reynolds stress components $\overline{\rho u_i'' u_i''}/\tau_w$, their corresponding anisotropies b_{ii} and the root mean square of pressure fluctuations p'_{rms}/τ_w are shown in figure 3.6(d)-3.6(l). The normalised anisotropy tensor is defined as $b_{ij} = \overline{\rho u_i'' u_j''}/\overline{\rho u_k'' u_k''} - 1/3\delta_{ij}$. All comparisons support the universality of the second order turbulence statistics for quasi-similar $Re_\tau^\star$ cases. We further investigate the quasi-similarity of the 1D energy spectra in figure 3.7(a)-3.7(f). Figures 3.7(a)-3.7(c) show the pre-multiplied streamwise 1D energy spectra of the density weighted streamwise velocity fluctuation at $y^\star \approx 15$ as a function of semi-locally scaled ($k_x^\star = k_x/Re_\tau^\star$) wave-number for quasi-similar $Re_\tau^\star$ cases. The inset shows the energy spectra
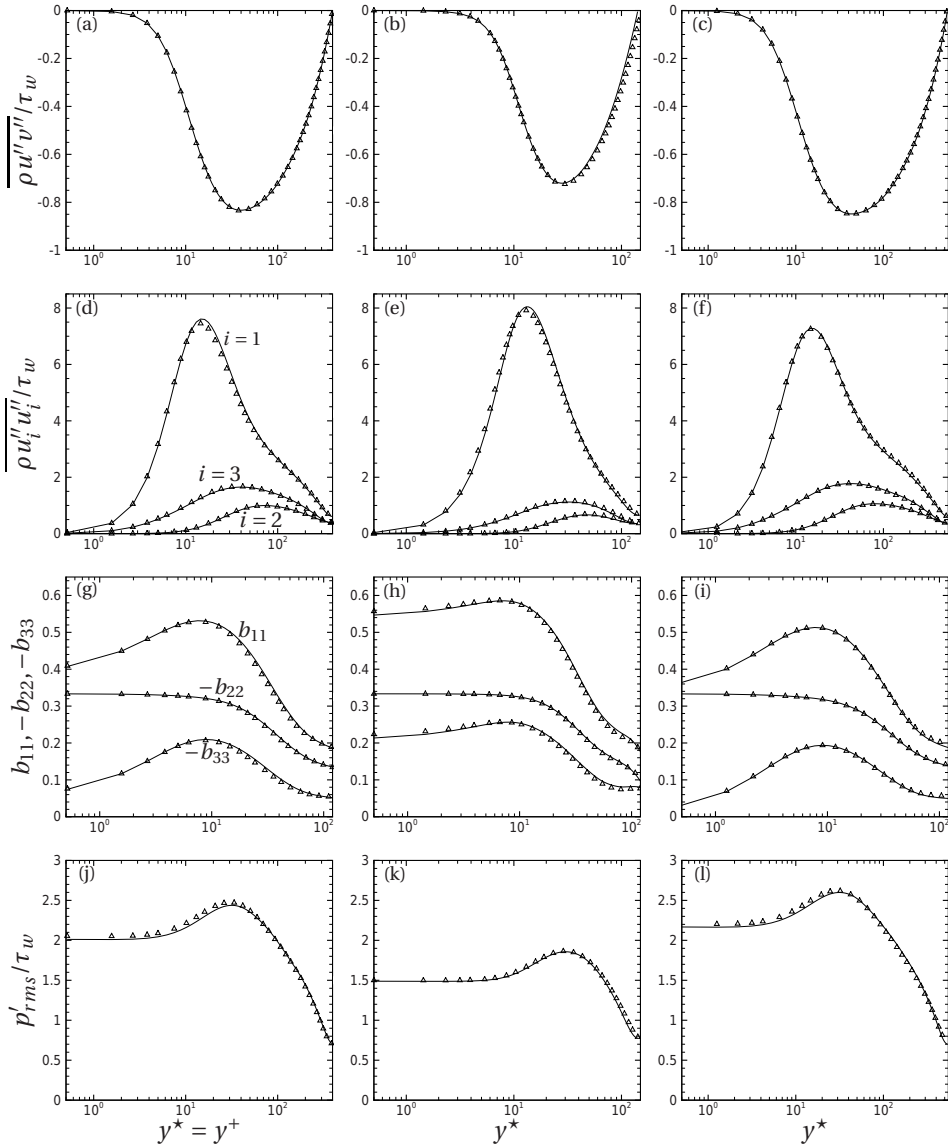
Figure 3.6: Comparison of (a-c) Reynolds shear stress, (d-f) normal Reynolds stresses, (g-i) normal Reynolds stress anisotropies and (j-l) root mean square of pressure fluctuations for cases (left column) CP395 and $\mathrm{CRe}_\tau^\star$, (middle column) $\mathrm{SRe}_{\tau GL}^\star$ and GL, (right column) $\mathrm{SRe}_{\tau Cv}^\star$ and Cv. Symbols are constant density cases: CP395, $\mathrm{SRe}_{\tau GL}^\star$ and $\mathrm{SRe}_{\tau Cv}^\star$, lines are variable density cases: $\mathrm{CRe}_\tau^\star$, GL and Cv.
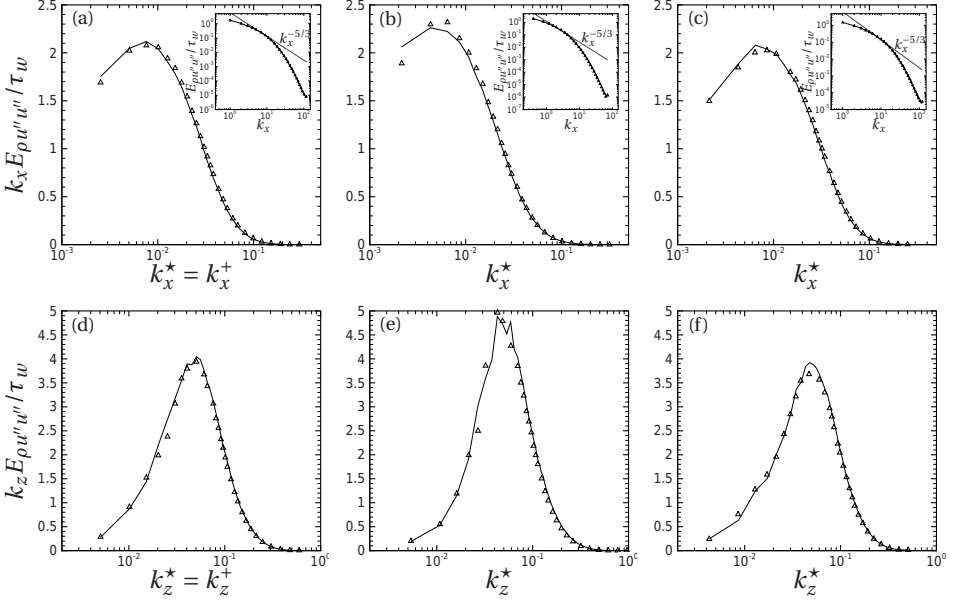
Figure 3.7: Comparison of pre-multiplied 1D (a-c) streamwise spectra and (d-f) spanwise spectra of the density weighted streamwise velocity fluctuation at $y^\star \approx 15$ for cases (left column) CP395 and CRe$_\tau^\star$, (middle column) SRe$_{\tau GL}^\star$ and GL, (right column) SRe$_{\tau Cv}^\star$ and Cv. Symbols are constant density cases: CP395, SRe$_{\tau GL}^\star$ and SRe$_{\tau Cv}^\star$, lines are variable density cases: CRe$_\tau^\star$, GL and Cv. In (a-c) the inset shows the 1D streamwise energy spectra in log-log plot.

in log-log plot, showing adequacy of grid-resolution as energy falls off over several decades. Because of moderate Reynolds number the inertial range is not very prominent (shown by $k_x^{-5/3} slope$). Spanwise 1D spectra are compared in figure 3.7(d)-3.7(f). Both streamwise and spanwise spectra show a good collapse for quasi-similar $Re_\tau^\star$ cases. Figures 3.5, 3.6 and 3.7 provide further evidence that the semi-local scaling is an effective tool to categorize variable property turbulence.

We now proceed to assess the influence of density fluctuations on turbulence statistics (Morkovin's hypothesis) by investigating second, third and fourth order moments of velocity fluctuation. Under the limit of small density fluctuations $\overline{\hat{u}_i' \hat{u}_j'} = \overline{\rho u_i' u_j'}/\tau_w \approx \overline{\rho u_i'' u_j''}/\tau_w \approx \overline{\rho u_i'' u_j''}/\tau_w = \widetilde{\hat{u}_i'' \hat{u}_j''}$ should hold. The different statistics are related as,

$$\overline{\rho u_i'' u_i''} = \overline{\rho}\,\overline{u_i'' u_i''} + \overline{\rho' u_i'' u_i''}, \tag{3.26}$$

and using equation (3.12) the relation between Reynolds and Favre averaged sec-
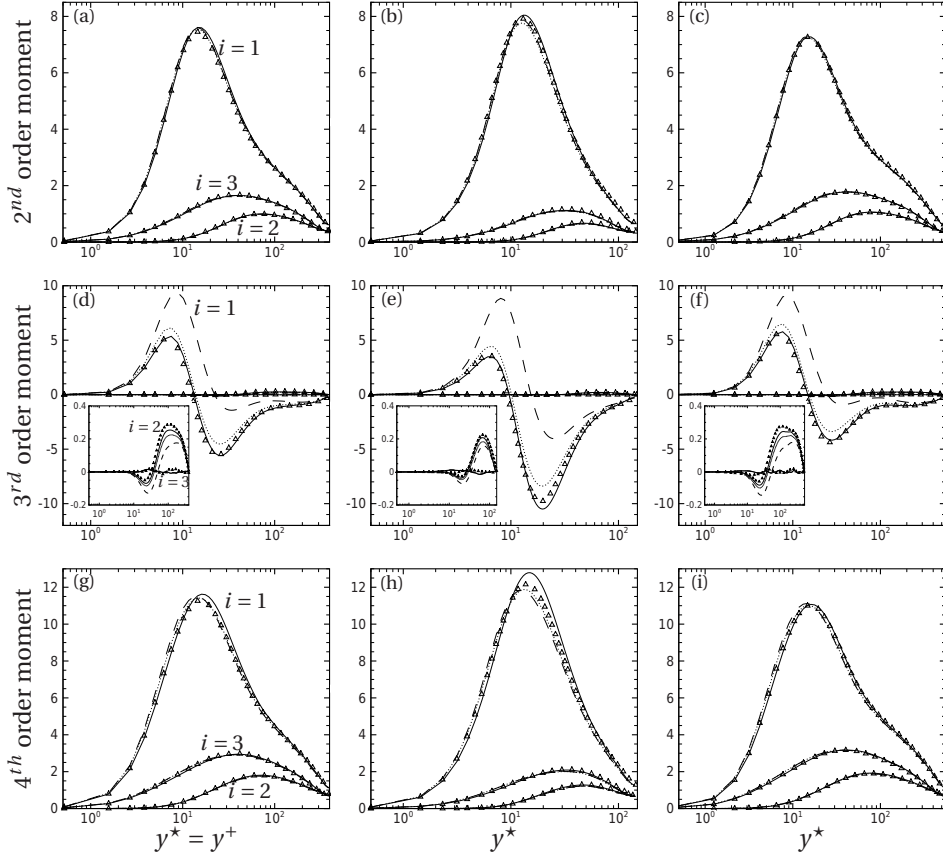
Figure 3.8: Influence of density fluctuation on (a-c) second (d-f) third and (g-i) fourth order moments of velocity fluctuations for cases (left column) CP395 and $CRe_\tau^\star$, (middle column) $SRe_{\tau GL}^\star$ and GL, (right column) $SRe_{\tau Cv}^\star$ and Cv. Symbols are constant density cases: CP395, $SRe_{\tau GL}^\star$ and $SRe_{\tau Cv}^\star$, lines are variable density cases: $CRe_\tau^\star$, GL and Cv. In (a-c) (——) $\overline{\rho u_i'' u_i''}/\tau_w$, (– – –) $\overline{\rho u_i'' u_i''}/\tau_w$, (·········) $\overline{\rho u_i' u_i'}/\tau_w$. In (d-f) (——) $\overline{\rho^{3/2} u_i''^3}/\tau_w^{3/2}$, (– – –) $\overline{\rho}^{3/2} \overline{u_i''^3}/\tau_w^{3/2}$, (·········) $\overline{\rho}^{3/2} \overline{u_i'^3}/\tau_w^{3/2}$. In (g-i) (——) $\sqrt{\overline{\rho^2 u_i''^4}}/\tau_w$, (– – –) $\overline{\rho}\sqrt{\overline{u_i''^4}}/\tau_w$, (·········) $\overline{\rho}\sqrt{\overline{u_i'^4}}/\tau_w$.

ond order statistics is given as,

$$\overline{\rho u_i' u_i'} = \overline{\rho u_i'' u_i''} - \overline{\rho}\left(\frac{\overline{\rho' u_i'}}{\overline{\rho}}\right)^2 \qquad (3.27)$$

These different relations are plotted in figure 3.8(a)-3.8(c), where it can be seen that the differences are negligible. The maximum error of $\approx 3.5\,\%$ occurs in case GL for which the density fluctuations are the highest (see figure 3.2(a)). The second terms on the right hand side of equation (3.26) and (3.27) are negligible compared with the first terms and therefore the difference between the profiles is insignificant.

We further assess the quasi-similarity and applicability of Morkovin's hypothesis on third and fourth order moments of velocity fluctuations. Under the validity of Morkovin's hypothesis the statistics should satisfy the following relation for the third order moments $\widehat{u_i'}^3 = \overline{\rho}^{3/2}\overline{u_i'}^3/\tau_w^{3/2} \approx \overline{\rho}^{3/2}\overline{u_i''}^3/\tau_w^{3/2} \approx \overline{\rho^{3/2}u_i''}^3/\tau_w^{3/2}$ and $\widehat{u_i'}^4 = \overline{\rho}^2\overline{u_i'}^4/\tau_w^2 \approx \overline{\rho}^2\overline{u_i''}^4/\tau_w^2 \approx \overline{\rho^2 u_i''}^4/\tau_w^2$ for the fourth order moments. For third order moments, the relation between $\overline{\rho^{3/2}u_i''}^3$ and $\overline{\rho}^{3/2}\overline{u_i''}^3$ can be expressed by using a binomial series for $\rho^{3/2} = \overline{\rho}^{3/2}(1 + \rho'/\overline{\rho})^{3/2}$, leading to,

$$\overline{\rho^{3/2}u_i''}^3 \approx \overline{\rho}^{3/2}\overline{u_i''}^3 + \frac{3}{2}\overline{\rho}^{1/2}\overline{\rho' u_i''}^3. \qquad (3.28)$$

Using equation (3.12) the relation between Reynolds and Favre averaged third order statistics is then,

$$\overline{\rho}^{3/2}\overline{u_i'}^3 = \overline{\rho}^{3/2}\overline{u_i''}^3 + 3\overline{\rho}^{3/2}\left(\frac{\overline{\rho' u_i'}}{\overline{\rho}}\right)\overline{u_i''}^2 - 2\overline{\rho}^{3/2}\left(\frac{\overline{\rho' u_i'}}{\overline{\rho}}\right)^3. \qquad (3.29)$$

Similarly, for fourth order moments, the relation between $\overline{\rho^2 u_i''}^4$ and $\overline{\rho}^2\overline{u_i''}^4$ is,

$$\overline{\rho^2 u_i''}^4 = \overline{\rho}^2\overline{u_i''}^4 + 2\overline{\rho}\overline{\rho' u_i''}^4 + \overline{\rho'^2 u_i''}^4, \qquad (3.30)$$

and using equation (3.12) the relation between Reynolds and Favre averaged fourth order statistics is given as,

$$\overline{\rho}^2\overline{u_i'}^4 = \overline{\rho}^2\overline{u_i''}^4 + 4\overline{\rho}^2\left(\frac{\overline{\rho' u_i'}}{\overline{\rho}}\right)\overline{u_i''}^3 + 6\overline{\rho}^2\left(\frac{\overline{\rho' u_i'}}{\overline{\rho}}\right)^2\overline{u_i''}^2 - 3\overline{\rho}^2\left(\frac{\overline{\rho' u_i'}}{\overline{\rho}}\right)^4. \qquad (3.31)$$

Figure 3.8(d)-3.8(f) shows the comparison for the third order moments of velocity fluctuations between quasi-similar $Re_\tau^\star$ cases. The inset shows an enlarged view for wall-normal (i=2) and spanwise direction (i=3). Unlike the lower-order statistics the adequacy of the sample size used to compute the higher-order

statistics is marginal as can be seen by small oscillations in the profiles of span-wise third order moments, which should be zero. For the variable density cases ($CRe_\tau^\star$, GL and Cv), the third order statistics using different forms of averaging do not collapse, which indeed is a breakdown of Morkovin's hypothesis. This break-down will most likely also be present in fully compressible simulations, but to the best of the authors knowledge, there is no literature that studies the Morkovin's hypothesis for third order statistics in compressible flows. Interestingly, a good agreement between quasi-similar $Re_\tau^\star$ cases is obtained using $\overline{\rho^{3/2} u_i''^{\,3}}/\tau_w^{3/2}$. The comparison is only qualitatively similar when $\overline{\rho}^{3/2}\overline{u_i'^{\,3}}/\tau_w^{3/2}$ is used but different when $\overline{\rho}^{3/2}\overline{u_i''^{\,3}}/\tau_w^{3/2}$ is used. These results indicate that $\sqrt{\rho}\,u_i''/\sqrt{\tau_w}$ is the ap-propriate scale for comparing quasi-similarity of third moments. The reason of the breakdown of Morkovin's hypothesis is discussed next. For the streamwise component (i=1), the third order moments are a measure of low and high speed streaks. In our present simulations with a cooled wall, the turbulent heat transfer at the lower wall requires $T'v' < 0$. Based on quadrant analysis it is known that, the high speed streaks have a tendency to move towards the wall (sweep) while low speed streaks tend to lift away from the wall (ejection), which for the lower wall corresponds to $u'v' < 0$. This implies that $T'u' > 0$, and since the density is inversely proportional to temperature $\rho'u' < 0$. The terms $\overline{\rho'u''^{\,3}}$ and $\overline{\rho'u'}$ are a measure of preferential concentration of high density fluid in low speed streaks and low density fluid in high speed streaks. In equation (3.28), this measure of preferential concentration is dominant as both the first and second terms on the right hand side are of comparable magnitudes, thereby causing a significant dif-ference between $\overline{\rho^{3/2} u''^{\,3}}$ and $\overline{\rho}^{3/2}\overline{u''^{\,3}}$. Similarly, the second term on the right hand side of equation (3.29) is of the same order as the first one, therefore, re-sulting in the difference between $\overline{\rho}^{3/2}\overline{u'^{\,3}}$ and $\overline{\rho}^{3/2}\overline{u''^{\,3}}$.

Figure 3.8(g)-3.8(i) shows the comparison for the square root of the fourth order moment of velocity fluctuations. A good collapse is obtained for cases with quasi-similar $Re_\tau^\star$ profiles except in case of GL for which a maximum dif-ference of ≈ 9 % occurs due to the high magnitudes of density fluctuations (see figure 3.2(a)). In both equations (3.30) and (3.31), the first term on the right side is dominant, therefore making the statistics weakly dependent on density fluctu-ations.

3.5. SUMMARY

Similar to constant property turbulent channel flows, where turbulence statistics can be expressed as a function of wall-normal distance y/h and friction Reynolds number Re_τ (based on wall quantities), we investigate if turbulence statistics for

turbulent flows with variable density ρ and viscosity μ can also be expressed as a function of y/h and semi-local Reynolds number $Re_\tau^\star \equiv Re_\tau \sqrt{(\overline{\rho}/\rho_w)}/(\overline{\mu}/\mu_w)$ (based on semi-local quantities). First a mathematical framework has been derived by rescaling the low-Mach number approximation of Navier-Stokes equations using local mean values for density, viscosity and semi-local friction velocity. The resulting semi-locally scaled governing equation for the mean and turbulent motions suggests that the leading order effect of variable properties on turbulence can be effectively characterized by $Re_\tau^\star$. The framework provides a theoretical basis for the use of semi-local scaling which was proposed based on heuristic arguments by Huang *et al.* (1995) and in addition provides additional implications. The approach suggests that the equivalent mean velocity is the van Driest transformed velocity $\overline{u}^{\mathrm{vD}}$, the wall-normal gradient of which also governs the production of semi-locally scaled turbulent fluctuations. In addition scaling of the viscous term is shown to be governed by $Re_\tau^\star$. Second, direct numerical simulations of a fully developed internally heated channel flow are performed to test the framework. Different constitutive relations for density and viscosity as a function of temperature are used in order to mimic a wide range of fluid behaviors and to develop a generalised framework for studying scaling characteristics of turbulence in variable property flows. Comparing turbulence statistics from different variable property cases lead us to conclude that $\overline{u}^{\mathrm{vD}}$ and second order turbulence statistics are a strong function of $Re_\tau^\star$ and their dependence on individual density or viscosity profile is minor. Furthermore, the Kolmogorov length scale normalized by semi-local viscous length scale ($\delta_\nu^\star = h/Re_\tau^\star$) is shown to exhibit good collapse as a function of semi-local wall coordinate ($y^\star = y/\delta_\nu^\star$) for all cases in the inner layer. We further assessed the quasi-similarity of higher order statistics and found that the fourth order moments collapse reasonably well for all quasi-similar $Re_\tau^\star$ cases. The comparison of the third order moments however, exhibits a breakdown of Morkovin's hypothesis, as they show a strong dependence on density fluctuations. A good collapse of third order moments among quasi-similar $Re_\tau^\star$ cases is observed when $\sqrt{\overline{\rho}}\,u_i''/\sqrt{\tau_w}$ is used as the fluctuating velocity scale.

4

EXTENDED VAN DRIEST VELOCITY TRANSFORMATION

4.1. VAN DRIEST VELOCITY TRANSFORMATION

The van Driest transformed velocity $\overline{u}^{\mathrm{vD}}$ and the diagnostic function $y d\overline{u}^{\mathrm{vD}}/dy$ as a function of y^+ and $y^\star$ for selected cases are shown in figure 4.1. As noted earlier, cases with quasi-similar $Re_\tau^\star$ profiles (symbols and lines with same colour) exhibit similar $\overline{u}^{\mathrm{vD}}$ profiles, irrespective of their individual density and viscosity profiles. However, when comparing cases with different $Re_\tau^\star$ gradients, deviations can be observed. For example, in figure 4.1(a), the slope of the linear viscous sublayer ($\overline{u}^{\mathrm{vD}} = y^+$) increases for cases with $dRe_\tau^\star/dy > 0$ (red line and symbols) and decreases for cases with $dRe_\tau^\star/dy < 0$ (blue line and symbols). Also an increase in the log-law additive constant (commonly $B = 5.2$) can be seen for cases with $dRe_\tau^\star/dy < 0$, while the opposite is observed for cases with $dRe_\tau^\star/dy > 0$. Additionally, the log-layer shifts outwards for cases with $dRe_\tau^\star/dy < 0$ and inwards for cases with $dRe_\tau^\star/dy > 0$, as can be seen from the profiles of the diagnostic function $y d\overline{u}^{\mathrm{vD}}/dy$ in figure 4.1(c). Figures 4.1(b) and figure 4.1(d) show $\overline{u}^{\mathrm{vD}}$ and the diagnostic function as a function of $y^\star$. The deviation of $\overline{u}^{\mathrm{vD}}$ for cases with $dRe_\tau^\star/dy \neq 0$ is even more prominent if plotted as a function of $y^\star$. On the other hand, the diagnostic function collapses the onset of the log-layer if plotted as function of $y^\star$. The reason for this collapse is investigated further using the streamwise stress-balance equation.

4.2. STRESS-BALANCE RELATION

The stress-balance relation for the turbulent and viscous stresses can be obtained by integrating the mean streamwise momentum equation, which, for a fully developed turbulent channel flow (neglecting viscosity fluctuations), gives

$$-\frac{\overline{\rho \widetilde{u'' v''}}}{\rho_w u_\tau^2} + \frac{h}{Re_\tau}\left(\frac{\overline{\mu}}{\mu_w}\right)\frac{d\left(\overline{u}/u_\tau\right)}{dy} \approx \frac{\tau}{\tau_w} = \left(1 - \frac{y}{h}\right), \tag{4.1}$$

where τ and τ_w are the total and wall shear stress, respectively. Equation (4.1) can be written in terms of semi-locally scaled velocity fluctuations (using the semi-local friction velocity $u_\tau^\star = \sqrt{\tau_w/\overline{\rho}}$)

$$\hat{u}_i'' = \frac{u_i''}{u_\tau^\star} = \sqrt{\frac{\overline{\rho}}{\rho_w}}\left(\frac{u_i''}{u_\tau}\right) \tag{4.2}$$

and the van Driest mean velocity increment

$$d\overline{u}^{\mathrm{vD}} = \sqrt{\frac{\overline{\rho}}{\rho_w}}\,d\left(\frac{\overline{u}}{u_\tau}\right), \tag{4.3}$$
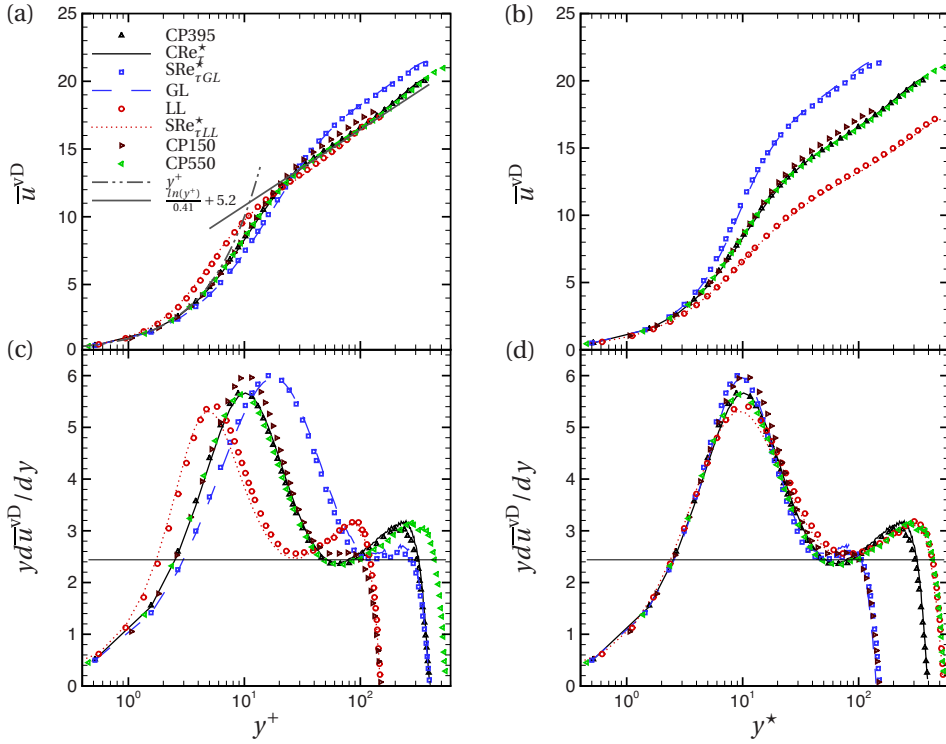
Figure 4.1: (a) and (b) van Driest velocity $\overline{u}^{\text{vD}}$, (c) and (d) diagnostic function $y d\overline{u}^{\text{vD}}/dy$ shown as a function of y^+ (left side) and $y^\star$ (right side). The solid horizontal line in (c) and (d) has a value of $1/0.41$.
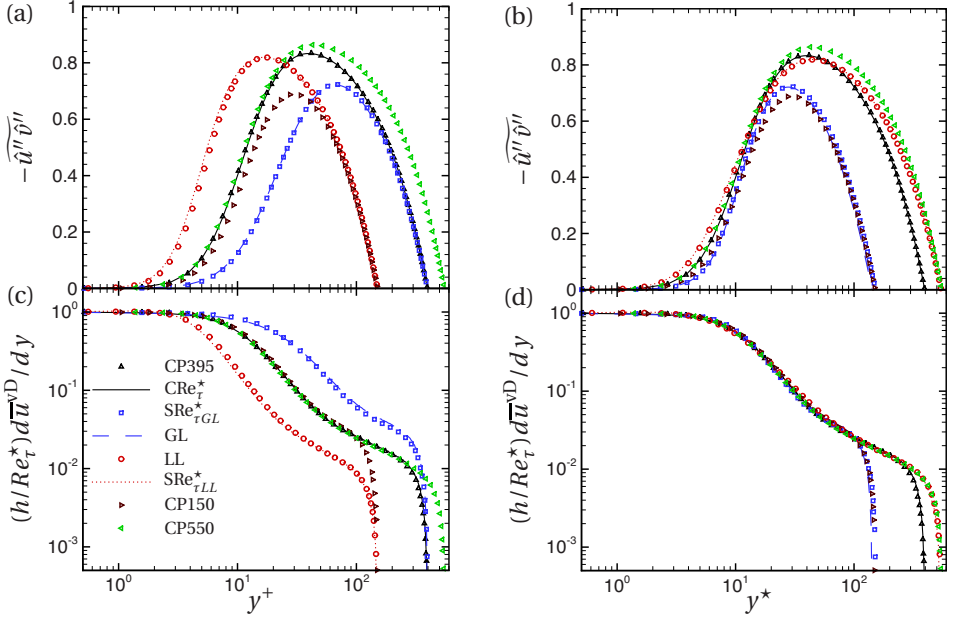
Figure 4.2: (a) and (b) Reynolds shear stress $-\widetilde{u''\hat{v}''}$, (c) and (d) viscous shear stress $\left(h/Re_\tau^\star\right)d\overline{u}^{\mathrm{vD}}/dy$ shown as a function of y^+ (left side) and $y^\star$ (right side).

to obtain the semi-locally scaled stress balance equation

$$-\widehat{u''\hat{v}''} + \frac{h}{Re_\tau^\star}\frac{d\overline{u}^{\mathrm{vD}}}{dy} \approx \frac{\tau}{\tau_w} = \left(1 - \frac{y}{h}\right). \tag{4.4}$$

Note, the viscous stress term is a function of the van Driest mean velocity gradient, scaled by the inverse of the semi-local Reynolds number. The reason for writing equation (4.1) in terms of $\overline{u}^{\mathrm{vD}}$ and $\widehat{u''\hat{v}''}$, originates from the previous chapter, where the Navier-Stokes equations were rescaled using the semi-local friction velocity and local mean properties in order to obtain governing equations for the semi-locally scaled mean, $\overline{u}^{\mathrm{vD}}$, and fluctuating velocities, $\hat{u}''_i$, with $Re_\tau^\star$ as a strong parameter. In other words, the combined influence of density and viscosity variations on turbulence statistics can be characterized using a single parameter, $Re_\tau^\star$.

The Reynolds shear stress $\widehat{u''\hat{v}''}$ and viscous stress term $\left(h/Re_\tau^\star\right)d\overline{u}^{\mathrm{vD}}/dy$ in equation (4.4) are plotted as a function of y^+ and $y^\star$ in figure 4.2. It is apparent that both stresses do not collapse if shown as a function of y^+ (figure 4.2(a) and (c)) for cases with different $Re_\tau^\star$ gradients. Similar observations have been reported for compressible non-adiabatic flows in Coleman *et al.* (1995); Foysi *et al.*

(2004); Morinishi *et al.* (2004). In comparison to a constant property case with a similar Re_τ value, the Reynolds shear stress decreases for cases with $dRe_\tau^\star/dy < 0$ and increases for cases with $dRe_\tau^\star/dy > 0$. On the other hand, if the stresses are plotted as a function of $y^\star$ (figure 4.2(b) and (d)), two observations can be made. First, the Reynolds shear stress profiles for all cases collapse closely in the inner layer, except in the region very close to the wall where small differences can be seen. Second, and more importantly, the viscous stresses for all cases perfectly collapse over the entire $y^\star$ range.

4.3. Extended van Driest velocity transformation

Given the last observation, it is evident that the viscous stress term, expressed as $(h/Re_\tau^\star)\, d\overline{u}^{\mathrm{vD}}/dy$, forms the basis to develop a proper scaling law for the mean velocity in flows with large density and viscosity gradients. We thus propose that the transformation must be based on the viscous stress

$$\frac{h}{Re_\tau^\star} \frac{d\overline{u}^{\mathrm{vD}}}{dy} = \Phi(y^\star)\,, \tag{4.5}$$

where Φ is an unknown function of $y^\star$. Using the chain rule $d/dy = (dy^\star/dy)d/dy^\star$, we can write equation (4.5) as

$$\frac{h}{Re_\tau^\star} \left(\frac{dy^\star}{dy}\right) \frac{d\overline{u}^{\mathrm{vD}}}{dy^\star} = \Phi(y^\star)\,. \tag{4.6}$$

This allows us to replace $dy^\star/dy$ in equation (4.6) by taking the derivative of $y^\star = yRe_\tau^\star/h$ with respect to y, to obtain

$$\left(1 + \frac{y}{Re_\tau^\star} \frac{dRe_\tau^\star}{dy}\right) \frac{d\overline{u}^{\mathrm{vD}}}{dy^\star} = \Phi(y^\star). \tag{4.7}$$

Equation (4.7) thus provides the scaling law for the mean streamwise velocity, which we will denote as $\overline{u}^\star$. Hence, $d\overline{u}^\star$ and $d\overline{u}^{\mathrm{vD}}$ are related through

$$d\overline{u}^\star = \left(1 + \frac{y}{Re_\tau^\star} \frac{dRe_\tau^\star}{dy}\right) d\overline{u}^{\mathrm{vD}} = \Phi(y^\star)dy^\star. \tag{4.8}$$

Note, it can be shown that the transformation proposed by Trettel & Larsson (2016) is equivalent when substituting the definitions of $Re_\tau^\star$ and $d\overline{u}^{\mathrm{vD}}$ into equation (4.8). Their transformation, which is expressed in terms of density and viscosity gradients, was obtained by equating the transformed log-law velocity gradient with the velocity gradient obtained from the stress-balance equation,

assuming that the Reynolds shear stress is similar for compressible and constant property cases. The present derivation follows an alternative route. It is based on rescaling the Navier–Stokes equations using the local mean properties and semi-local friction velocity, which naturally suggests that the viscous terms are scaled by the semi-local Reynolds number $Re_\tau^\star$ to account for changes in viscous scales due to property variations. The transformation expressed in terms of equation (4.8) thus emphasises the fact that, similar to turbulence statistics, the transformation is also governed by the $Re_\tau^\star$ profiles, rather than individual density and viscosity profiles.

The derived velocity transformation $\overline{u}^\star = \int_0^{\overline{u}^{\mathrm{vD}}} \left(1 + \left(y/Re_\tau^\star\right) dRe_\tau^\star/dy\right) d\overline{u}^{\mathrm{vD}}$, is shown in figure 4.3(a) as a function of $y^\star$. It can be seen that $\overline{u}^\star$ is perfectly able to collapse the velocity profiles for all cases over the entire $y^\star$ range. In the previous chapter we showed that similar turbulence statistics and van Driest mean velocity profiles $\overline{u}^{\mathrm{vD}}$ are obtained for cases with similar $Re_\tau^\star$ distributions, even if their individual mean density and viscosity profiles substantially differ. Here, we derive a transformation that accounts for gradients in $Re_\tau^\star$ in order to extend the van Driest transformation.

Using the derived velocity transformation it is also possible to explain the collapse of the diagnostic function as a function of $y^\star$, as mentioned earlier. The definitions in equations (4.5) and (4.8) can be expressed as

$$\frac{h}{Re_\tau^\star}\frac{d\overline{u}^{\mathrm{vD}}}{dy} = \frac{d\overline{u}^\star}{dy^\star} = \Phi(y^\star)\,. \tag{4.9}$$

Substituting $h/Re_\tau^\star = y/y^\star$ in equation (4.9) we can obtain the correlation between the diagnostic function and the newly derived velocity scale $u^\star$ as

$$y\frac{d\overline{u}^{\mathrm{vD}}}{dy} = y^\star\frac{d\overline{u}^\star}{dy^\star} = y^\star\Phi(y^\star)\,, \tag{4.10}$$

which explains the collapse of the diagnostic function in figure 4.1(d).

The invariance of Φ as a function of $y^\star$ can further be quantified by expressing it in terms of turbulence mixing length. Following Huang & Coleman (1994), the Reynolds shear stress can be written in terms of the velocity gradient using the mixing-length theory as

$$l_m^2 = \frac{-\widetilde{u''v''}}{\left(d\overline{u}/dy\right)^2} = \frac{-\widehat{u''}\widehat{v''}}{\left(d\overline{u}^{\mathrm{vD}}/dy\right)^2}\,. \tag{4.11}$$

Substituting the Reynolds shear stress in equation (4.4) using equation (4.11) results in a quadratic equation for $d\overline{u}^{\mathrm{vD}}/dy$, which, when solved and simplified,
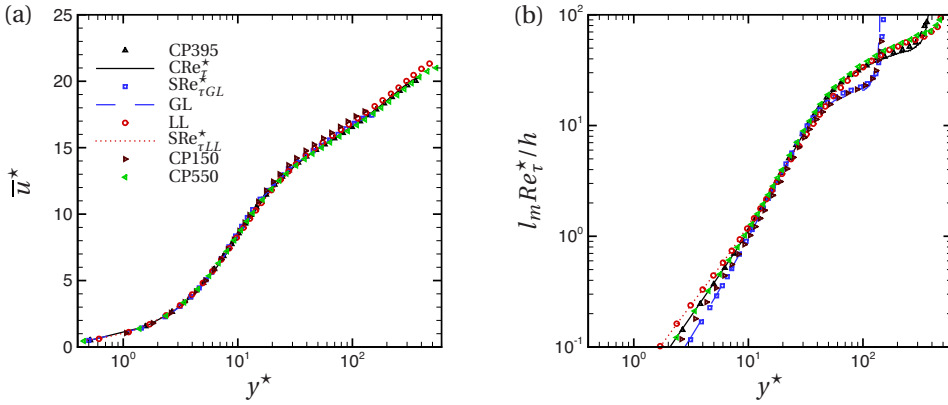
Figure 4.3: (a) Transformed velocity $\overline{u}^\star$ and (b) mixing length $l_m Re_\tau^\star / h$ as a function of $y^\star$.

gives

$$\Phi(y^\star) = \frac{2\tau/\tau_w}{1 + \sqrt{1 + 4\tau/\tau_w \left(l_m Re_\tau^\star/h\right)^2}} \, . \tag{4.12}$$

The above expression naturally suggests that l_m scales with the semi-local length scale $h/Re_\tau^\star$. Figure 4.3(b) shows $l_m Re_\tau^\star/h$ as a function of $y^\star$. A satisfactory collapse is obtained for almost the entire inner layer, except very close to wall where small deviations occur. These deviations stem from turbulence modulation caused by strong $Re_\tau^\star$ gradients, which we will discuss in detail in section 5.1 and 5.2. However, close to the wall the viscous stress dominates and small values of mixing length do not alter the velocity scaling.

In the following, we will investigate if the scaling can also be successfully applied for supersonic adiabatic flows, for which the van Driest scaling already shows a satisfying collapse. For this, we will use a DNS database for adiabatic supersonic boundary layers from Pirozzoli & Bernardini (2011); Bernardini & Pirozzoli (2011) and data for an incompressible boundary layer from Jiménez *et al.* (2010). The investigated compressible cases are with Mach numbers Ma=2, 3 and 4 and corresponding Reynolds numbers are Re_τ=450, 400 and 400, respectively. The incompressible boundary layer is at Re_τ=450. Figure 4.4(a) shows the $Re_\tau^\star$ distribution for these cases as a function of $y^\star$. Note, in contrast to the heated and cooled channel flows, the gradient of $Re_\tau^\star$ at the wall is negligible. The largest $Re_\tau^\star$ variation is obtained for the Ma=4 case, where $Re_\tau^\star$ at the edge of the boundary layer is more than four times as large than at the wall. The van Driest mean velocity $\overline{u}^{vD}$ is plotted as a function of y^+ in figure 4.4(b). A satisfying
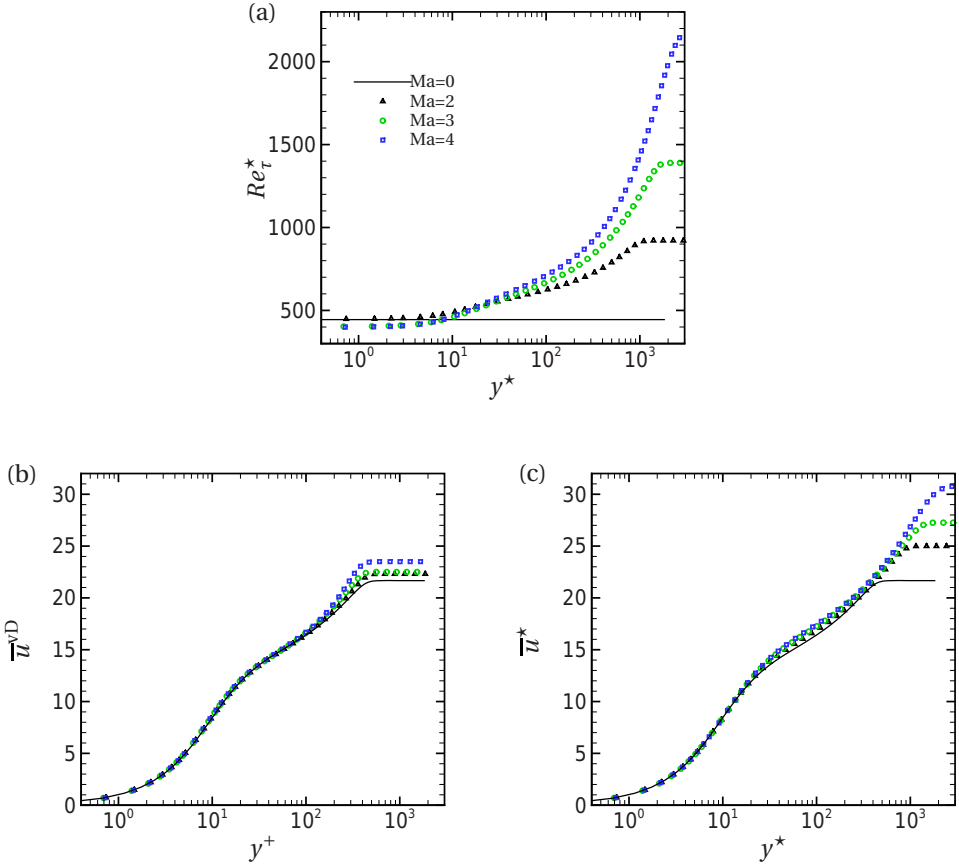
Figure 4.4: (a) $Re_\tau^\star$ shown as a function of $y^\star$, (b) van Driest velocity $\overline{u}^{\mathrm{vD}}$ shown as a function of y^+, (c) transformed velocity $\overline{u}^\star$ shown as a function of $y^\star$ for adiabatic supersonic boundary layers obtained from Pirozzoli & Bernardini (2011); Bernardini & Pirozzoli (2011), compared with reference boundary layer data from Jiménez *et al.* (2010).
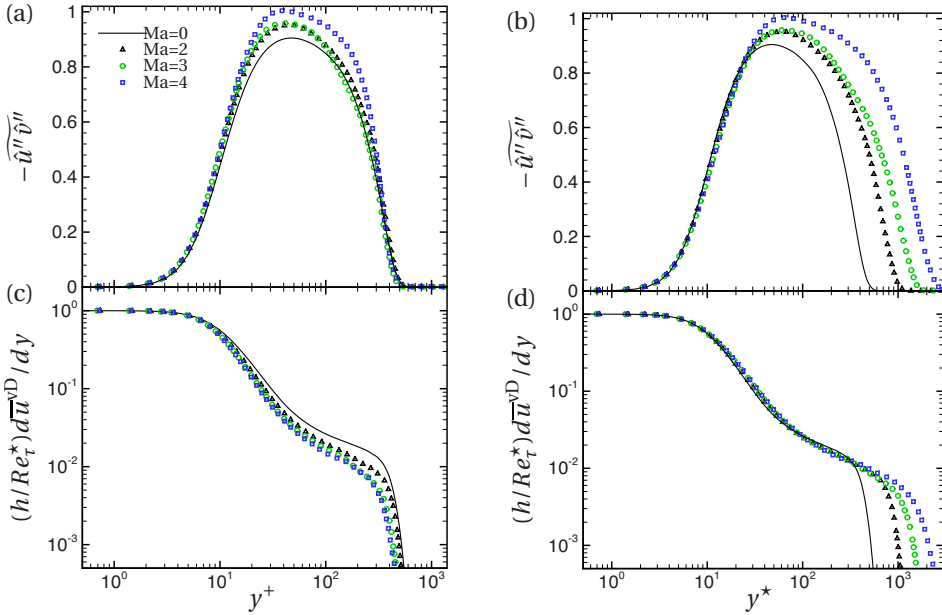
Figure 4.5: (a) and (b) Reynolds shear stress $-\widetilde{\hat{u}''\hat{v}''}$, (c) and (d) viscous shear stress $(h/Re_\tau^\star)d\overline{u}^{vD}/dy$ shown as a function of y^+ (left side) and $y^\star$ (right side) for adiabatic supersonic boundary layers obtained from Pirozzoli & Bernardini (2011); Bernardini & Pirozzoli (2011), compared with boundary layer data from Jiménez *et al.* (2010).

collapse for the compressible and incompressible boundary layer is obtained, except in the wake region, which has been studied in more detail by Zhang *et al.* (2012). The transformed velocity $\overline{u}^\star$ as a function of $y^\star$ is shown in figure 4.4(c). Also here, a reasonable collapse for the $\overline{u}^\star$ velocity profiles is obtained. However, small deviations with respect to the incompressible boundary layer occur in the buffer and logarithmic region. Interestingly, also Trettel & Larsson (2016) have found a similar disagreement for cooled turbulent boundary layers. One of the plausible reasons for these deviations could be related to the location of the maximum of the $Re_\tau^\star$ gradient, which for adiabatic supersonic boundary layer occurs in the buffer layer. In contrast, for our simulations as well as for supersonic channel flows, the maximum of the $Re_\tau^\star$ gradient is at the wall. While the influence of the $Re_\tau^\star$ gradient on the mixing length was limited to regions with $y^\star < 10$ in channel flows, in adiabatic supersonic boundary layers its influence might be of relevance in turbulence dominated regions and should be investigated in more detail.

The implication of the above mean velocity scaling characteristics on the stress balance relation for these turbulent boundary layers is discussed next. The Reynolds shear and viscous stresses are shown in figure 4.5 as a function of y^+ and $y^\star$. Both stresses show a superior collapse if they are plotted as a function of $y^\star$. Analogous to the plot of $\overline{u}^\star$ vs $y^\star$ in figure 4.4(c), also the viscous stresses of the compressible cases slightly deviate from the incompressible case, as can be seen in figure 4.5(d). On the other hand, if the stresses are plotted as a function of y^+, it can be seen that the turbulent shear stress profiles increase and the viscous stress profiles decrease with Mach number, see figure 4.5(a) and figure 4.5(c). This Mach number dependence of the stresses as a function of y^+ can be shown mathematically by writing the stress-balance equation (4.4) for the incompressible and compressible boundary layer as,

$$\left. \left(\widetilde{u''\hat{v}''} + \frac{\tau}{\tau_w} \right) \right|_{\text{incomp}} = \left. \frac{h}{Re_\tau} \frac{d\overline{u}^{\text{vD}}}{dy} \right|_{\text{incomp}} \quad \text{for the incompressible BL,} \quad (4.13)$$

$$\left. \frac{Re_\tau^\star}{Re_\tau} \left(\widetilde{u''\hat{v}''} + \frac{\tau}{\tau_w} \right) \right|_{\text{comp}} = \left. \frac{h}{Re_\tau} \frac{d\overline{u}^{\text{vD}}}{dy} \right|_{\text{comp}} \quad \text{for the compressible BL.} \quad (4.14)$$

In the constant stress layer $(\tau/\tau_w)_{\text{comp}} = (\tau/\tau_w)_{\text{incomp}} = 1$ and due to the collapse of $\overline{u}^{\text{vD}}$ as a function of y^+, equations (4.13) and (4.14) can be equated as,

$$\left. \left(\widetilde{u''\hat{v}''} + 1 \right) \right|_{\text{incomp}} = \left. \frac{Re_\tau^\star}{Re_\tau} \left(\widetilde{u''\hat{v}''} + 1 \right) \right|_{\text{comp}}. \quad (4.15)$$

Therefore, if $Re_\tau^\star > Re_\tau$ it follows that $\left. \left(-\widetilde{u''\hat{v}''} \right) \right|_{\text{comp}} > \left. \left(-\widetilde{u''\hat{v}''} \right) \right|_{\text{incomp}}$, which explains the Mach number dependence of the stresses. The increase in shear

stress for the supersonic cases also explains the corresponding increase in turbulence intensities when compared with incompressible cases (Pirozzoli *et al.*, 2004; Bernardini & Pirozzoli, 2011), due to the increase in the turbulence kinetic energy production. The partial success of both y^+ and $y^\star$ in adiabatic supersonic boundary layers, thus warrants future studies. The semi-local scaling utilizes the invariance of $(h/Re_\tau^\star)d\overline{u}^{\mathrm{vD}}/dy$ as a function of $y^\star$ to obtain $\overline{u}^\star$, while adiabatic boundary layers exhibit invariance of a more fundamental variable, namely the wall-normalized van Driest transformed mean spanwise vorticity $\overline{\omega}_z^{\mathrm{vD}}/(\overline{\omega}_z^{\mathrm{vD}})_w = d\overline{u}^{\mathrm{vD}}/dy^+ = (h/Re_\tau)d\overline{u}^{\mathrm{vD}}/dy$ as a function of y^+. The significance of mean vorticity is discussed in the next chapter.

4.4. SUMMARY

Strong near-wall gradients in $Re_\tau^\star$ result in a failure to collapse the van Driest transformed mean velocity $\overline{u}^{\mathrm{vD}}$ as a function of y^+. An extension of the van Driest transformation that accounts for the gradients in $Re_\tau^\star$ is derived based on the compelling collapse of the viscous stresses $(h/Re_\tau^\star)d\overline{u}^{\mathrm{vD}}/dy$ for all cases when plotted as a function of the semi-local wall coordinate $y^\star$. A successful collapse of $\overline{u}^\star$ when plotted as a function of $y^\star$ is obtained for all the investigated cases. The robustness of the transformation is further investigated using the mixing length, which also shows a good collapse in the entire inner layer except in regions close to the wall ($y^\star < 10$), where cases with $Re_\tau^\star$ gradients deviate. However, close to the wall the viscous stress dominates and small values of mixing length do not alter the velocity scaling. The applicability of the transformation is also tested on adiabatic supersonic boundary layers of Bernardini & Pirozzoli (2011); Pirozzoli & Bernardini (2011), which are known to show an excellent agreement of $\overline{u}^{\mathrm{vD}}$ as a function of y^+. The new transformed velocity collapses supersonic cases at different Mach numbers. However, the supersonic cases showed a small increase in the log-law additive constant when compared to an incompressible turbulent boundary layer. In a recent work Trettel & Larsson (2016) derived a similar transformation in terms of density and viscosity gradients, and applied it successfully to supersonic channel flows with isothermal cooled walls.

5

TURBULENCE MODULATION

5.1. INFLUENCE OF $Re_\tau^\star$ GRADIENTS ON NEAR-WALL TURBULENCE STATISTICS

Turbulence statistics are strongly influenced by near-wall modifications of turbulence. Near-wall turbulence modifications for variable property flows can be classified into two main mechanisms: (i) changes in viscous scales, and (ii) structural changes of turbulence. The semi-local scaling is successful in collapsing turbulence statistics, such as mean velocity (see figure 4.3(a)), Reynolds and viscous shear stress (see figure 4.2(b) and (d)), because it accommodates the change in viscous scales using local quantities, and because these quantities are not significantly affected by structural changes and non-local effects very close to the wall. On the other hand, the semi-local scaling fails for turbulence statistics that are sensitive to strong non-local interactions of the buffer layer vortical structures with the sublayer region, e.g., statistics of vorticity fluctuations. Furthermore, the semi-local scaling also fails for turbulence statistics that contain direct information of turbulence structure, e.g., turbulence anisotropy (Foysi *et al.*, 2004).

We first study the gradient of the van Driest transformed mean velocity $\overline{u}^{\mathrm{vD}}$, which we will refer to as the van Driest transformed mean spanwise vorticity $\overline{\omega}_z^{\mathrm{vD}}$. $\overline{u}^{\mathrm{vD}}$ is the analogue to the mean velocity in a variable density flow, and therefore a study of its gradients allows us to draw conclusions on the stability of the flow. We then discuss turbulent vorticity fluctuations and turbulence anisotropy to emphasize the failure of the semi-local scaling due to non-locality and changes in turbulence structure, respectively.

5.1.1. MEAN SPANWISE VORTICITY

The wall-normalized van Driest transformed mean spanwise vorticity $\overline{\omega}_z^{\mathrm{vD}}/(\overline{\omega}_z^{\mathrm{vD}})_w$ $= d\overline{u}^{\mathrm{vD}}/dy^+ = (h/Re_\tau)d\overline{u}^{\mathrm{vD}}/dy$ is plotted as a function of y^+ and $y^\star$ in figure 5.1(a) and figure 5.1(b), respectively. Unlike for adiabatic walls, where $\overline{\omega}_z^{\mathrm{vD}}/(\overline{\omega}_z^{\mathrm{vD}})_w$ is invariant as a function of y^+ in the inner layer (e.g., Pirozzoli & Bernardini, 2011), $\overline{\omega}_z^{\mathrm{vD}}/(\overline{\omega}_z^{\mathrm{vD}})_w$ is neither a function of y^+ nor $y^\star$ for non-adiabatic walls. Based on Eyink (2008) vorticity generated at the wall is transported outward, first diffused by viscosity and subsequently advected by turbulence. Strong gradients in viscosity in the viscous dominated region thus change the vorticity transport and consequently the mean velocity profile. The change in mean velocity profile then directly influences turbulence. Equivalently, in variable density flows, strong gradients in $Re_\tau^\star$ (since $Re_\tau^\star$ characterizes the viscous scale), influence the van Driest transformed mean velocity profile. It
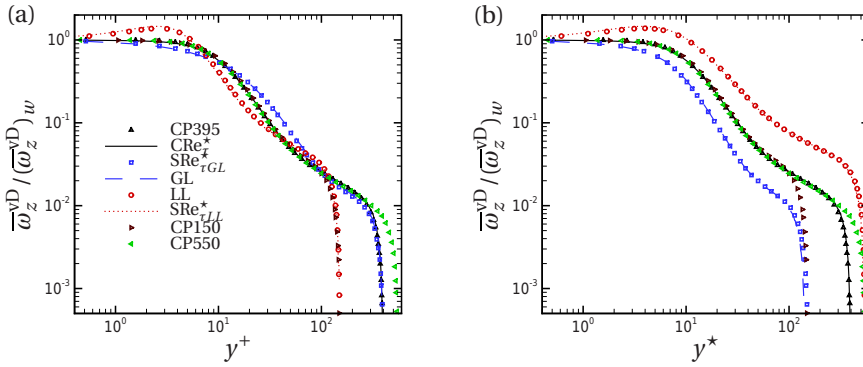
Figure 5.1: Wall-normalized van Driest transformed mean spanwise vorticity $\overline{\omega}_z^{\text{vD}}/(\overline{\omega}_z^{\text{vD}})_w$ shown as a function of (a) y^+ and (b) $y^\star$.

is clearly visible in figure 5.1 that $\overline{\omega}_z^{\text{vD}}/(\overline{\omega}_z^{\text{vD}})_w$ shows a local maximum for cases with $dRe_\tau^\star/dy > 0$ (red line and symbols). This maximum implies an inflection point in the velocity profile, which also indicates a more unstable flow condition. The reverse happens for cases with $dRe_\tau^\star/dy < 0$ (blue line and symbols) where the velocity profile becomes fuller (higher negative curvature of $d^2\overline{u}^{\text{vD}}/dy^2$), causing the flow to become more stable (Gad-el Hak, 1990). This effect is similar to flow control techniques that change the curvature of the velocity profile at the wall by introducing, e.g., wall motion, suction/injection, streamwise pressure-gradients, or wall-normal viscosity-gradients (Gad-el Hak, 1990). For example, in an adverse-pressure-gradient region (decelerated flow) the appearance of an inflection point is known to increase the wall-burst rate (Bushnell & McGinley, 1989). The opposite is observed for flows with favorable-pressure-gradient, where the base velocity state mitigates the formation of localised near-wall inflections (Bushnell & McGinley, 1989). Marquillie *et al.* (2011) performed a linear stability analysis about the mean base profile of a turbulent boundary layer with adverse-pressure-gradient, and showed a higher streak instability for cases with a pronounced wall-normal inflection point. This fact has an important implication on near-wall turbulent structures and is discussed in more detail in section 5.2.

5.1.2. TURBULENT VORTICITY FLUCTUATIONS

The *rms* of the semi-locally scaled turbulent vorticity fluctuations $\hat{\boldsymbol{\omega}}' = \nabla \times \hat{\mathbf{u}}'$ for streamwise ($\hat{\omega}_x'$), wall-normal ($\hat{\omega}_y'$) and spanwise ($\hat{\omega}_z'$) directions are shown in fig-
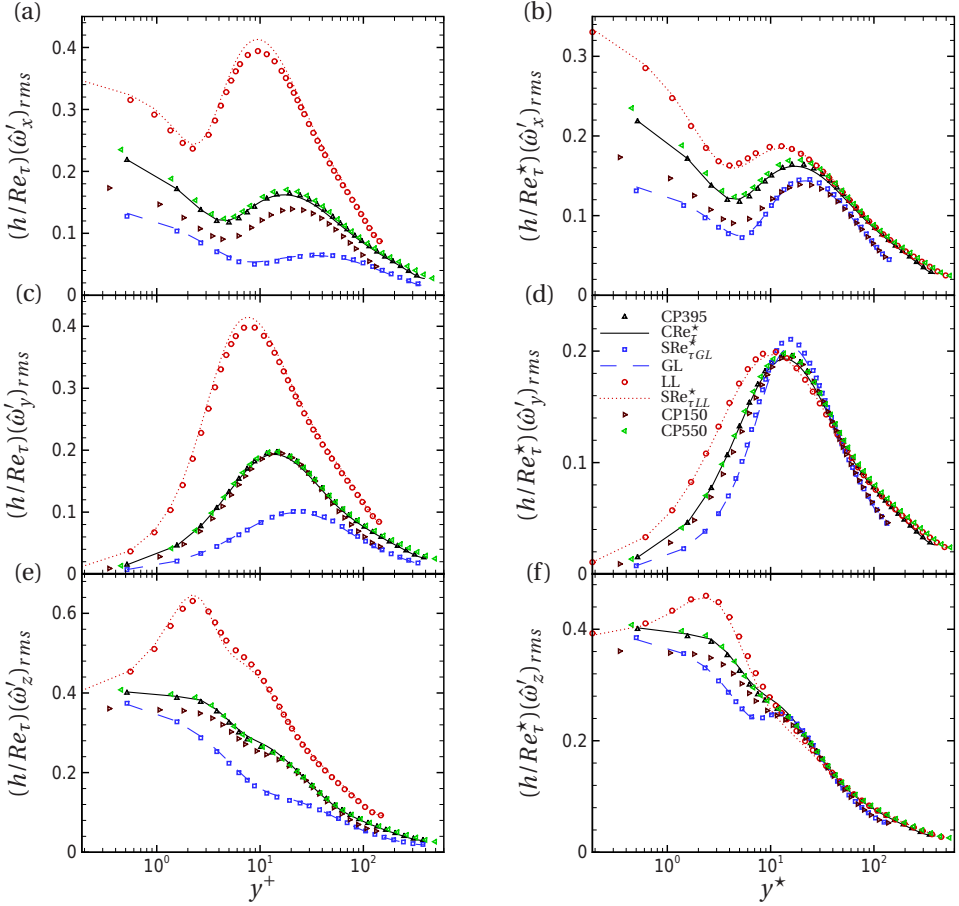
Figure 5.2: Root mean square *rms* vorticity fluctuations of (a) and (b) streamwise ($\hat{\omega}'_x$), (c) and (d) wall-normal ($\hat{\omega}'_y$), (e) and (f) spanwise components ($\hat{\omega}'_z$), normalized by and plotted using wall-based scales (left side) and semi-local scales (right side).

ure 5.2. Figure 5.2(a), 5.2(c) and 5.2(e) shows the vorticity normalised by the wall-based viscous scale h/Re_τ as a function of y^+, whereas the vorticity normalised by the semi-local viscous scale $h/Re_\tau^\star$ as a function of $y^\star$ is shown in figure 5.2(b), 5.2(d) and 5.2(f). In accordance with previous turbulence statistics, quasi-similar vorticity statistics are obtained for cases with quasi-similar $Re_\tau^\star$ profiles, even though the individual density and viscosity profiles differ. Comparing cases with different $Re_\tau^\star$ gradients in figure 5.2(a), 5.2(c) and 5.2(e) shows considerable differences both in terms of magnitude and wall-normal location of peak values. On the other hand, the semi-local normalisation (figure 5.2(b), 5.2(d) and 5.2(f)) provides a reasonable collapse in regions away from the wall for comparable $Re_{\tau\,c}^\star$, and it is also able to preserve the wall-normal locations of the peaks. However, in the near-wall region the semi-local scaling with $h/Re_\tau^\star$ fails and does not provide a collapse of the vorticity profiles, even though the van Driest transformed mean spanwise vorticity scales well with $h/Re_\tau^\star$ (see figure 4.2(d)). In the following, we will make several comments on statistics of semi-locally normalised vorticity fluctuations.

1. It is known that even for constant property cases the x and z vorticity fluctuation components increase with Reynolds number, whereas the y component shows Re_τ independence (Antonia & Kim, 1994). This Re_τ dependence is particularly prominent for the low Reynolds number case CP150 (brown triangles).

2. For the variable property cases, it is interesting to see that the cases with $dRe_\tau^\star/dy > 0$ have the highest magnitude of the semi-locally scaled $\hat\omega'_x$ in the near-wall region, although their Re_τ values are the lowest ($Re_\tau = 150$). The opposite occurs for cases with decreasing $Re_\tau^\star$ away from the wall. There, the streamwise vorticity fluctuations are the lowest, even for comparatively high values of $Re_\tau = 395$. This is clearly a variable property effect that is in contrast to the Reynolds number dependence as discussed in point (i). Similar observations can be made for the y and z components. The semi-locally scaled rms values of $\hat\omega'_y$ and $\hat\omega'_z$ are the highest in the near-wall region for cases with $dRe_\tau^\star/dy > 0$ and vice versa for cases with $dRe_\tau^\star/dy < 0$.

3. For cases with $dRe_\tau^\star/dy > 0$, the z component has a maximum at approximately the same location where the van Driest transformed mean spanwise vorticity also shows a maximum. This is in agreement to the inflection point of the van Driest transformed mean velocity, which causes the flow to become more unstable as mentioned in section 5.1.1. For cases with $dRe_\tau^\star/dy < 0$ the fluctuations fall off rapidly away from the wall.
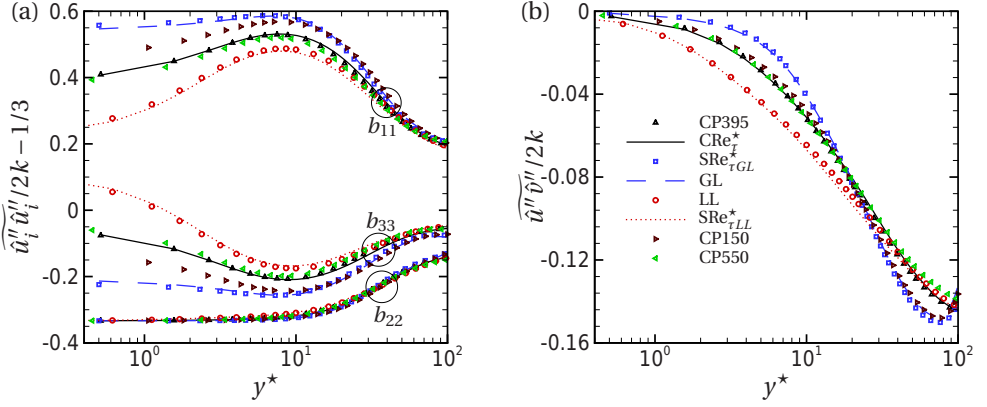
Figure 5.3: (a) Normal Reynolds stress anisotropies, (b) Reynolds shear stress anisotropy as a function of $y^\star$.

The failure of the semi-local scaling is presumably caused by both structural changes in turbulence and strong non-local interactions between structures in the buffer and the viscous sublayer that will be discussed in detail in section 5.2.

5.1.3. TURBULENT STRESS ANISOTROPY

Gradients of $Re_\tau^\star$ have a large effect on inter-component energy transfer and thus on turbulence anisotropy. The anisotropy tensor is defined as,

$$b_{ij} = \frac{\widetilde{\hat{u}_i'' \hat{u}_j''}}{2k} - \delta_{ij}\frac{1}{3},$$
(5.1)

with the turbulence kinetic energy $k = \widetilde{\hat{u}_k'' \hat{u}_k''}/2$ and δ_{ij} the Kronecker delta. Figure 5.3(a) shows that for cases with $dRe_\tau^\star/dy < 0$ an increase in streamwise component b_{11} and a decrease in spanwise component b_{33} occurs in the near-wall region if compared to cases with $dRe_\tau^\star/dy = 0$. The opposite is seen for cases with $dRe_\tau^\star/dy > 0$. The wall-normal component b_{22}, however, is not influenced by gradients in $Re_\tau^\star$. The increase in b_{11} for cases with $dRe_\tau^\star/dy < 0$ indicates a decrease in the redistribution of turbulence energy from the streamwise direction to the other two directions. The component b_{12}, which is the ratio of turbulent shear stress and turbulence kinetic energy, is shown in figure 5.3(b). It decreases for cases with $dRe_\tau^\star/dy < 0$, indicating a reduced momentum transfer in spite of higher turbulence kinetic energy, while the reverse is true for cases with $dRe_\tau^\star/dy > 0$. The same quantities are also shown in figure 5.4 for the adiabatic
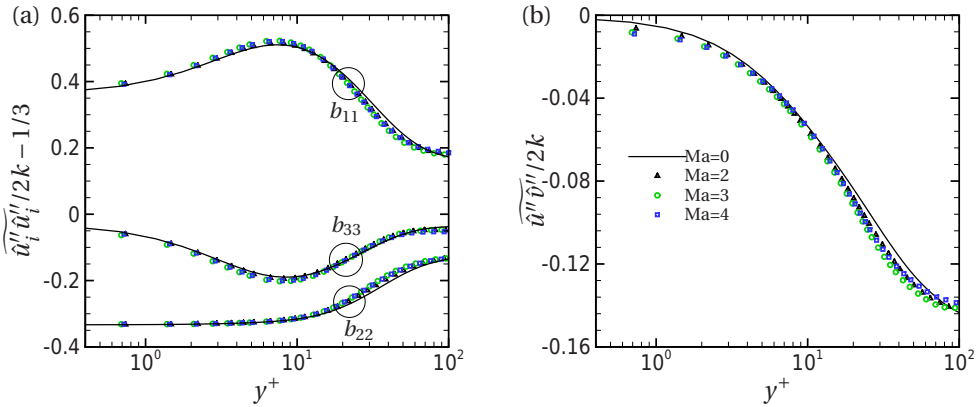
Figure 5.4: (a) Normal Reynolds stress anisotropies, (b) Reynolds shear stress anisotropy as a function of y^+ for adiabatic supersonic boundary layers obtained from Pirozzoli & Bernardini (2011); Bernardini & Pirozzoli (2011) and compared with reference boundary layer data from Jiménez *et al.* (2010).

supersonic turbulent boundary layer cases from Pirozzoli & Bernardini (2011); Bernardini & Pirozzoli (2011) and compared with reference boundary layer data from Jiménez *et al.* (2010). No significant changes in anisotropy are noticeable since $dRe_\tau^\star/dy \approx 0$ in the near-wall region. The change in anisotropy for cases with $dRe_\tau^\star/dy \neq 0$ is linked to modifications in turbulent structures that will be discussed next.

5.2. INFLUENCE OF RE$_\tau^\star$ GRADIENTS ON NEAR-WALL TURBULENT STRUCTURES

Here we investigate the influence of near-wall $Re_\tau^\star$ gradients on the characteristics of near-wall streaks and quasi-streamwise vortices, which are both known to be the dominant structures in near-wall turbulence, in order to provide a mechanistic description for the modulated statistics.

5.2.1. NEAR-WALL STREAKS

Coleman *et al.* (1995); Duan *et al.* (2010); Lagha *et al.* (2011*a*) observed increased streamwise coherence (longer streaks) for supersonic turbulent boundary layers with cooled walls, while shorter streaks were observed for heated walls by Lagha *et al.* (2011*a*). These streak modifications were quantified in terms of wall-

Figure 5.5: Pre-multiplied 1D streamwise spectra of the density weighted stream-wise velocity fluctuation at $y^\star \approx 13$ plotted as function of (a) k_x^+ and (b) $k_x^\star$ for cases CP395, GL, LL2 and CP150.

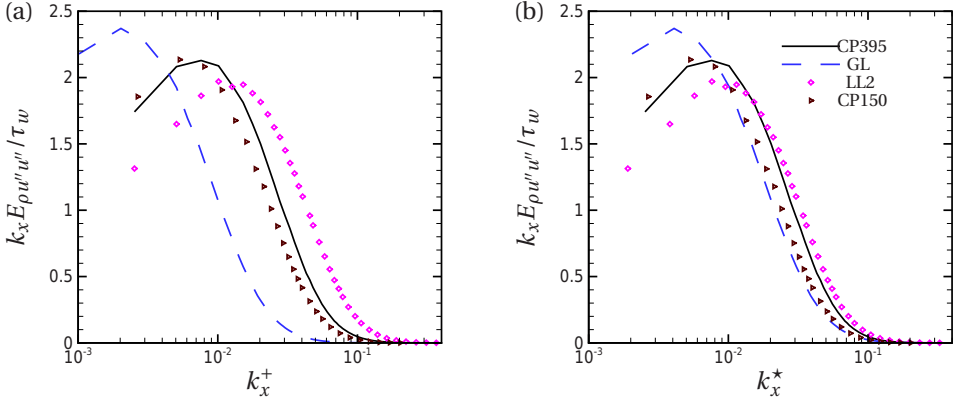based viscous units. Morinishi *et al.* (2004) used two-point correlations to conclude that near-wall streaks do not become more coherent and are independent of heated or cooled walls, when semi-local scaling is taken into account.

We revisit some of these conclusions and in addition provide further insights into turbulence modulation, by examining 1D streamwise and spanwise energy spectra, contour plots of $\sqrt{\rho}u''/\sqrt{\tau_w}$ and joint-pdfs of $\sqrt{\rho}u''/\sqrt{\tau_w}$ and $\sqrt{\rho}v''/\sqrt{\tau_w}$. Figure 5.5 shows the pre-multiplied streamwise 1D spectra of the density weighted streamwise velocity fluctuation at $y^\star \approx 13$ as a function of both classically ($k_x^+ = k_x/Re_\tau$) and semi-locally scaled ($k_x^\star = k_x/Re_\tau^\star$) wave-numbers for cases CP395, GL, LL2 and CP150. Using the classically scaled coordinates, it can be seen that the spectra for case GL are shifted to lower wave numbers, while they are shifted to higher wave numbers for case LL2. Thus, the structures appear elongated for case GL and shortened for case LL2, as also concluded by Coleman *et al.* (1995); Duan *et al.* (2010); Lagha *et al.* (2011*a*). However, using semi-local coordinates, an approximate collapse over a wide wave number range can be obtained, and the peaks of spectra occur at approximately the same $k_x^\star$ location for both cases (note, the peak of spectra for GL in figure 5.5(b) is at a slightly lower wave number due to low-Reynolds number effect which can be seen by comparing with case CP150). Additionally, figure 5.6 shows the pre-multiplied spanwise 1D spectra at the same $y^\star$ location as a function of $k_z^\star$ and k_z^+, to emphasize that also the mean spacing of streamwise streaks remains unaltered as a function of $k_z^\star$. In other words, the modulation of streak spacing
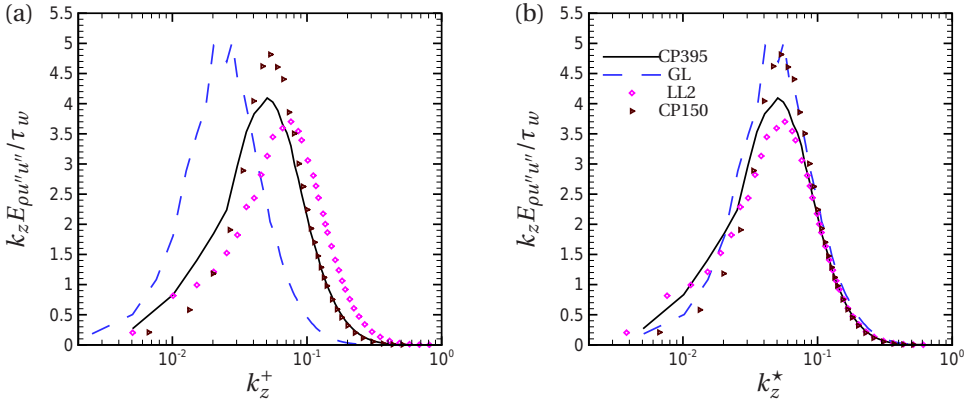
Figure 5.6: Pre-multiplied 1D spanwise spectra of the density weighted stream-wise velocity fluctuation at $y^\star \approx 13$ plotted as function of (a) k_z^+ and (b) $k_z^\star$ for cases CP395, GL, LL2 and CP150.

observed at $y^\star \approx 13$ using classical wall scaling is misleading and exclusively quantified by semi-local scales only.

The pre-multiplied streamwise spectra provide additional insights with respect to previous findings. It can be seen that for case GL the energy containing low wave-number scales strengthen (see peak magnitude of spectra), while they weaken for case LL2. The pre-multiplied streamwise 1D spectra for case $\text{SRe}_{\tau GL}^\star$ (see figure 3.7(b)) exhibited similar strengthening at large wavelengths as case GL. The strengthening and weakening of these large scale anisotropic structures seem to be independent of individual density or viscosity profiles, and thus depend on the $Re_\tau^\star$ profile only. The previously mentioned increase in streamwise Reynolds stress anisotropy for case with $dRe_\tau^\star/dy < 0$ is associated with strengthening of these large-scale streamwise structures, while the vice versa is true for case with $dRe_\tau^\star/dy > 0$.

A visual impression of these large scale structures can be obtained by means of contour plots of instantaneous flow fields as given in figure 5.7 and 5.8. Figure 5.7 shows streamwise velocity fluctuations $\sqrt{\rho}u''/\sqrt{\tau_w}$ in a plane parallel to the wall at $y^\star \approx 15$ for case CP395, LL2 and $\text{SRe}_{\tau GL}^\star$. Even though all three cases are constant density flows (see table 3.1), we suggest to use ρ, instead of $\overline{\rho}$, for the normalization ($\sqrt{\rho}u''/\sqrt{\tau_w}$) in these plots. The reason for this suggestion is that the magnitude of the streaks is modulated by the preferential concentration of high density fluid in a low-speed streak, and vice versa (see discussion for figure 3.8(d)-3.8(f)). For cases LL2 and $\text{SRe}_{\tau GL}^\star$ both, semi-local ($x^\star = xRe_\tau^\star/h$
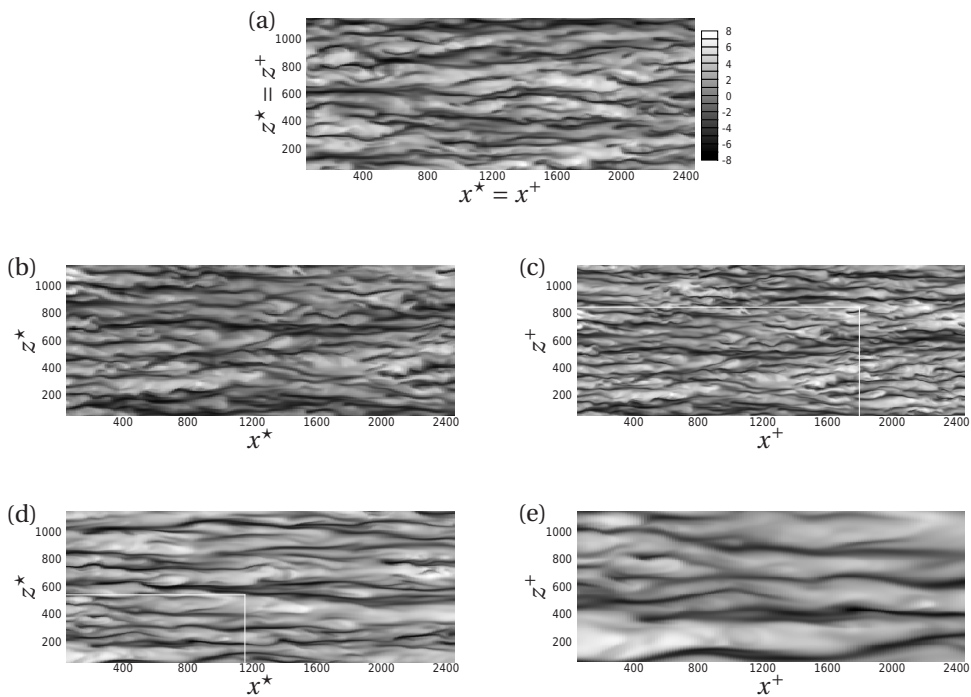
Figure 5.7: Instantaneous streamwise velocity fluctuations $\sqrt{\bar{\rho}}u''/\sqrt{\tau_w}$ in a $x-z$ plane at $y^\star \approx 15$ (a) case CP395, (b) case LL2 using $x^\star - z^\star$ coordinates, (c) case LL2 using $x^+ - z^+$ coordinates, (d) case SRe$^\star_{\tau GL}$ using $x^\star - z^\star$ coordinates and (e) case SRe$^\star_{\tau GL}$ using $x^+ - z^+$ coordinates. The white box in figure (c) corresponds to figure (b) and box in figure (d) corresponds to figure (e).
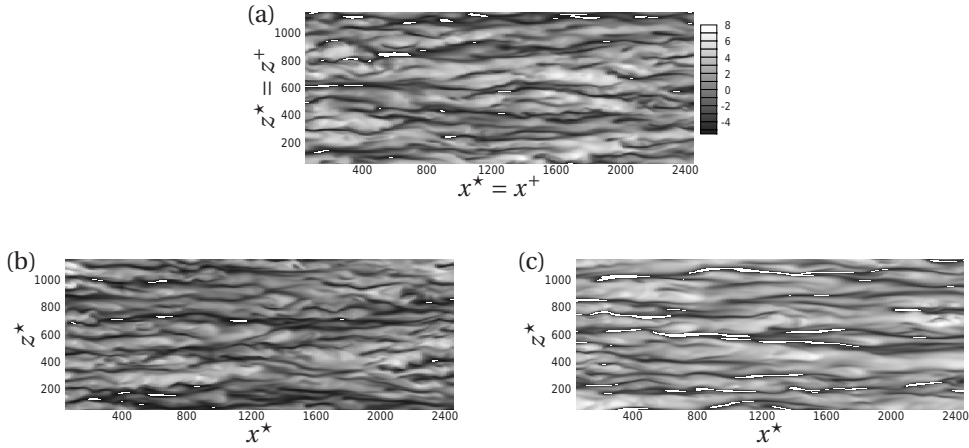
Figure 5.8: Instantaneous streamwise velocity fluctuations $\sqrt{\overline{\rho}}u''/\sqrt{\tau_w}$ in $x^\star - z^\star$ plane at $y^\star \approx 15$. Contour for $\sqrt{\overline{\rho}}u''/\sqrt{\tau_w} < -5.5$ are cut-off (seen as white) (a) case CP395, (b) case LL2, (c) case $\text{SRe}_{\tau GL}^\star$.

and $z^\star = zRe_\tau^\star/h$) and classical ($x^+ = xRe_\tau/h$ and $z^+ = zRe_\tau/h$) wall units are shown. The box size in all visualisations is 2400×1100, based on corresponding non-dimensional coordinates $x^\star \times z^\star/x^+ \times z^+$. Scale separation becomes more prominent for case LL2 (figure 5.7(b) and 5.7(c)) and less prominent for case $\text{SRe}_{\tau GL}^\star$ (figure 5.7(d) and 5.7(e)) when compared with the constant property case (figure 5.7(a)). The comparison of semi-locally scaled variable property contours (figure 5.7(b) and 5.7(d)) with constant property contours (figure 5.7(a)) show a similar mean spanwise spacing between the streaks for all cases. A similar comparison using classical wall coordinates (figure 5.7(c) and 5.7(e)) show decreased spacing for case LL2, and an increased spacing for case $\text{SRe}_{\tau GL}^\star$. The white box in figure 5.7(c) and figure 5.7(d) indicates the domain size of figure 5.7(b) and figure 5.7(e), respectively, in order to outline the scaling of the structures. The strengthening (for a case with $dRe_\tau^\star/dy < 0$) and weakening (for a case with $dRe_\tau^\star/dy > 0$) of near-wall structures with respect to the constant property case can be visualised in figure 5.8. The $\sqrt{\overline{\rho}}u''/\sqrt{\tau_w}$ contours are taken at the same plane and time as figure 5.7. The low-speed streaks are cut-off below a threshold value of $\sqrt{\overline{\rho}}u''/\sqrt{\tau_w} = -5.5$, thus highlighting the more energetic structures. It can be seen that for case LL2 (figure 5.8(b)) the energetic spots reduce in comparison to case CP395 (figure 5.8(a)). On the other hand, the energetic spots in case of $\text{SRe}_{\tau GL}^\star$ (figure 5.8(c)) become more prominent. The large-scale streamwise structures are low-speed streaks which become strengthened for case $\text{SRe}_{\tau GL}^\star$, while weakening for case LL2. Since these structures scale with semi-local wall

Figure 5.9: Joint pdf of $\sqrt{\overline{\rho}}u''/\sqrt{\tau_w}$ and $\sqrt{\overline{\rho}}v''/\sqrt{\tau_w}$ with contours of probability weighted Reynolds shear stress $\rho u''v''/\tau_w P(\sqrt{\overline{\rho}}u''/\sqrt{\tau_w}, \sqrt{\overline{\rho}}v''/\sqrt{\tau_w})$, for (a,b) case GL, (c,d) case SRe$^{\star}_{\tau GL}$ and (e,f) case LL2 (all lines), compared with case CP395 (filled contours). Left column $y^{\star} \approx 8.5$; right column $y^{\star} \approx 15$.

units, their modulation is not related with outer layer motions.

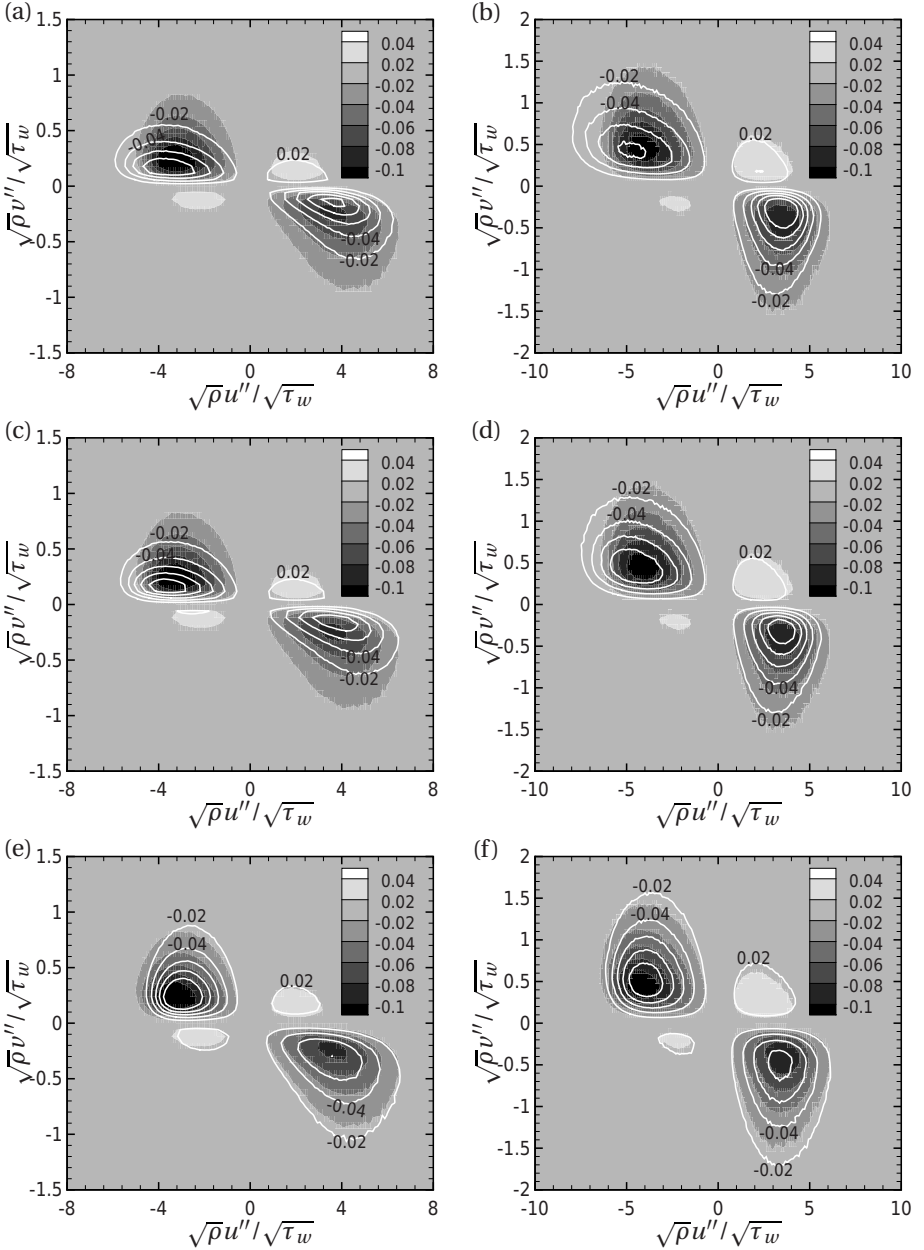Another way to quantify the turbulent structure is by means of probability density functions (pdfs). Figure 5.9 shows joint-pdfs of $\sqrt{\rho}u''/\sqrt{\tau_w}$ and $\sqrt{\rho}v''/\sqrt{\tau_w}$ as contour plots for the probability-weighted Reynolds shear stress $\rho u''v''/\tau_w P(\sqrt{\rho}u''/\sqrt{\tau_w}, \sqrt{\rho}v''/\sqrt{\tau_w})$ at $y^\star \approx 8.5$ and $y^\star \approx 15$. Since these plots are also affected by the preferential concentration of high density fluid in a low-speed streak, and vice versa, we use ρ instead of $\overline{\rho}$ for normalization. Each contour plot divides the probability-weighted Reynolds shear stress into four quadrants, according to the sign of u'' and v''. The most energetic events, which are responsible for generating the Reynolds shear stress, occur in quadrants Q2 and Q4 and are referred to as ejection ($u'' < 0$ and $v'' > 0$) and sweep ($u'' > 0$ and $v'' < 0$) events, respectively. The first observation that can be made from figure 5.9(a), 5.9(c) and 5.9(e) is that in comparison to CP395, case LL2 shows a larger Reynolds shear stress, while cases GL and case $\mathrm{SRe}_{\tau GL}^\star$ show a smaller Reynolds shear stress, as can be clearly seen from the spread of iso-contour lines. An additional observation is related to the Reynolds shear stress generation mechanism. For case GL and $\mathrm{SRe}_{\tau GL}^\star$ the pdfs in Q2 are clearly broader in streamwise- and flatter in wall-normal direction. Thus, stronger negative streamwise fluctuations and weaker positive wall-normal fluctuations appear. In other words, low-speed streaks are stabilised and do not lift as intensely for cases GL and $\mathrm{SRe}_{\tau GL}^\star$ ($dRe_\tau^\star/dy < 0$) when compared to CP395. The reverse happens for case LL2 ($dRe_\tau^\star/dy > 0$) where low-speed streaks weaken and lift more intensely away from the wall.

For constant property cases, the near-wall streak spacing in the viscous sublayer remains remarkably constant over a wide range of Reynolds numbers (Klewicki *et al.*, 1995). Figure 5.10(a) shows the normalised pre-multiplied spanwise spectra of the density weighted streamwise velocity fluctuation at $y^\star \approx 0.5$ (top) and $y^\star \approx 13$ (bottom) as a function of semi-locally scaled wavelength $\lambda_z^\star = \lambda_z Re_\tau^\star/h$. The peak location of the spectra represents the mean streak spacing and it can be seen that at $y^\star \approx 13$ the spacing is the same for all cases ($\lambda_z^\star \approx 120$). This is one of the few similarities that variable property and constant property cases share. On the other hand, at $y^\star \approx 0.5$ only the constant property cases (CP395, CP150, CP550) and the variable property case $\mathrm{CRe}_\tau^\star$ show a similar streak spacing of $\lambda_z^\star = \lambda_z^+ \approx 110$, whereas the variable property cases with $dRe_\tau^\star/dy \neq 0$ show a modulation in streak spacing. The cases GL and $\mathrm{SRe}_{\tau GL}^\star$ with $dRe_\tau^\star/dy < 0$ (blue lines and symbols) show an increased streak spacing of $\lambda_z^\star \approx 220$, while $\lambda_z^\star \approx 50$ for cases LL and $\mathrm{SRe}_{\tau LL}^\star$ with $dRe_\tau^\star/dy > 0$ (red lines and symbols). Figure 5.10(b) gives an overview of the near-wall streak spacing as a function of $y^\star$. The lines in the plot indicate the boundaries where $k_z E_{\rho u''u''}/\overline{\rho u''u''}$ is 96% of the peak value at a certain $y^\star$ location. It can be seen
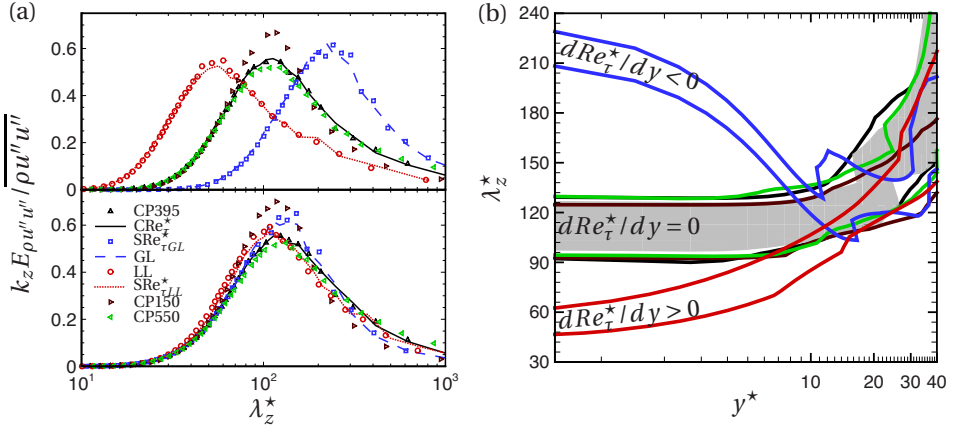
Figure 5.10: (a) Normalised pre-multiplied spanwise spectra $k_z E_{\rho u'' u''} / \overline{\rho u'' u''}$ as a function of $\lambda_z^\star$ at $y^\star \approx 0.5$ (top) and $y^\star \approx 13$ (bottom). (b) $\lambda_z^\star$ as a function of $y^\star$ obtained using bands of $k_z E_{\rho u'' u''} / \overline{\rho u'' u''}$ with values larger than 96% of its maximum value; black, brown, green, blue and red lines correspond to case CP395, CP150, CP550, GL and LL, respectively; the grey region corresponds to case $CRe_\tau^\star$.

that the mean streak spacing appears to become universal after $y^\star \approx 12 - 13$, while it deviates significantly in the viscous sublayer for cases with $dRe_\tau^\star / dy \neq 0$. This deviation is not surprising, because of the fact that the sublayer flow is known to be induced by advecting dominant structures in the buffer layer (Kim & Hussain, 1993). The wall-normal location of the dominant structures is also found to be universal in semi-local units, as shown by Pei *et al.* (2013), using a vorticity-velocity correlation in supersonic channel flows with isothermal walls at different Mach numbers. The strong non-local influence of turbulence structures in the buffer layer on the near-wall region creates a disparity between the semi-local scales and the actual turbulence scales in the sublayer.

5.2.2. VORTICAL STRUCTURES

The three-dimensional swirling strength $\Lambda_{ci}(x, y, z)$, which is based on the imaginary part of the complex eigenvalue of the velocity gradient tensor (Zhou *et al.*, 1999), is used to identify the near-wall vortical structures. The swirling strength separates swirling- from shearing motion, and it can be evaluated using the gradient tensor of the instantaneous- or the fluctuating velocity field. Note, it has been analytically shown that it is not possible to decouple the

mean shear from the instantaneous field (Chen *et al.*, 2014). In our investigations we evaluate the swirling strength using the instantaneous velocity gradient tensor, because the local shear depends on the instantaneous field. Similar to Wu & Christensen (2006), we normalise the local swirling strength with its corresponding wall-normal root-mean-square $\Lambda_{ci}^{rms}(y)$ value, such that $\acute{\Lambda}_{ci}(x,y,z) = \Lambda_{ci}(x,y,z)/\Lambda_{ci}^{rms}(y)$.

Figure 5.11(a) shows the top-view of an iso-surface of $\acute{\Lambda}_{ci} = 1.5$ for case CP395 in the near-wall region up to $y^+ \approx 50$. As stated in previous studies (Jeong *et al.*, 1997; Robinson, 1991), the near-wall region is mostly populated by quasi-streamwise vortices. The iso-surfaces are coloured by the sign of their streamwise vorticity, where red denotes positive and blue negative vorticity. The figure also shows a slice of low-speed streaks at $y^+ = 13$ (seen as light blue). A small section (black box) of the same instantaneous flow field is shown in an isometric view in figure 5.11(b), in order to show the inclination and elevation of these structures with respect to the wall (the grey shades are projections of the iso-surfaces onto the wall). As noted by Jeong *et al.* (1997), the structures with positive vorticity tend to tilt in negative direction, and those with negative vorticity tend to tilt in positive direction with respect to the streamwise direction within the x-z plane. This tilting is correlated with the waviness of streaks and it is associated with transferring of streamwise turbulence energy to spanwise and wall-normal components (Jeong *et al.*, 1997). Therefore, studying the orientation of these structures can clarify the changes in anisotropy that occur in flows with gradients in $Re_\tau^\star$.

The orientation of the vortical structures can be characterized by the real eigenvector v_r of the velocity gradient tensor, which is able to differentiate the swirling direction from the vorticity direction (Gao *et al.*, 2011; Pirozzoli *et al.*, 2008). However, before evaluating the vortex orientation we must first find the vortex centre. This is done by performing the following steps. First, all the grid points that correspond to the local maxima of the swirling strength Λ_{ci} are flagged in all $y - z$ planes of the numerical domain. Next the real eigenvector v_r of these points is used to check if the projection angles in the perpendicular planes, which define the lift and the tilt and are denoted as θ_{xy} and θ_{xz}, are within $\pm45°$. If this condition is met, the points are retained, otherwise they are discarded. These steps are repeated to also find the vortex centres in the $z - x$ and $x - y$ planes of the computational domain. Finally, only the points with $\acute{\Lambda}_{ci} \geq 1.5$ are kept and used as the vortex centres. Note, most of vortex centres were found in the $y - z$ plane, showing the dominance of quasi-streamwise vortices. An outcome of this eduction procedure is given in figure 5.11(b), where the vortex centres with their corresponding eigenvectors are shown. Since eigenvectors can have either of the two opposing directions, its positive direction is chosen

(a)

(b)
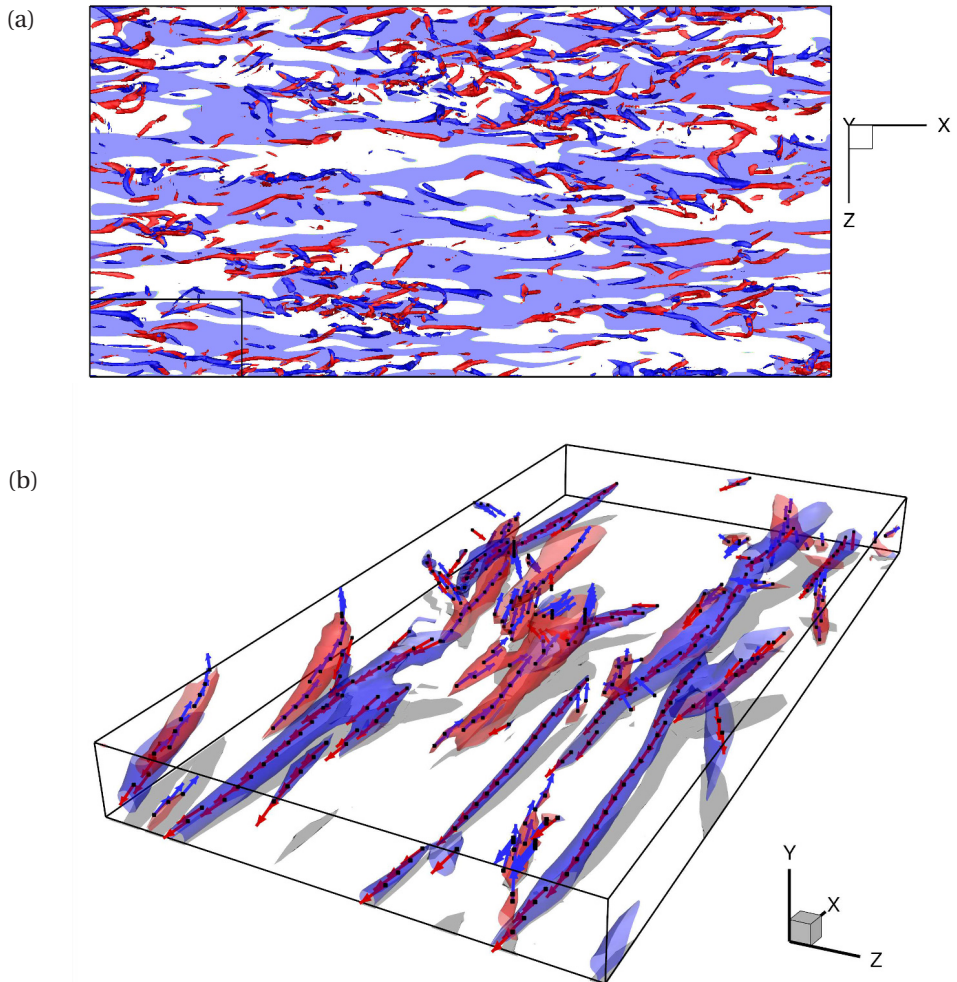
Figure 5.11: (a) Iso-surfaces of swirling strength seen from top, red iso-surfaces correspond to positive voriticity while blue denotes negative vorticity; contours show the low speed-streaks; rectangular box corresponds to figure b (b) isometric view of structures with real eigen-vectors at the vortex centre- the grey color corresponds to projection of the structures at wall, vectors corresponding to positive vorticity shown as blue while red denotes negative vorticity.
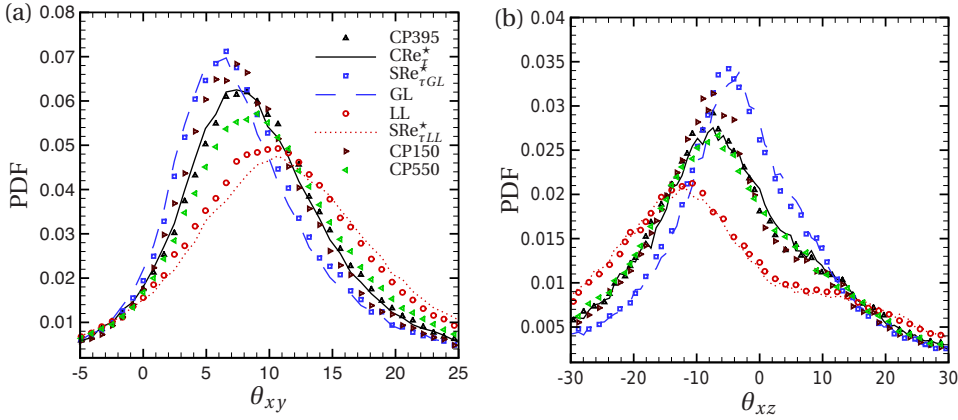
Figure 5.12: Probability density function of projection angle of eigenvector v_r at $y^\star = 13$ (a) inclination angle θ_{xy} (b) tilting angle θ_{xz}.

such that the dot product with the the vorticity vector is positive. As evident, the eigenvectors v_r provide an excellent measure of the orientation axis of the vortical structures. We will now apply this procedure to obtain statistics of the inclination and tilting angle to draw conclusions on turbulence modulation for all constant and variable property cases investigated in this work.

The probability-density-functions (pdf) of the inclination θ_{xy} and tilting angle θ_{xz} of the vortical structures at $y^\star = 13$ are shown in figure 5.12. Similar to turbulence statistics, the orientation of vortical structures for cases with quasi-similar Re$_\tau^\star$ profiles also shows quasi-similarity and is therefore independent of individual density and viscosity profiles. As shown in figure 5.12(a), an increase in Re$_\tau$ from 150 to 550 for the constant property cases, increases the mode of the pdf from 7° to 8° and broadens the pdf showing an increase in standard deviation. The variable property cases with $dRe_\tau^\star/dy < 0$ (blue line and symbols) show a decrease in the mode of the pdf (6°) and a decrease in standard deviation. The opposite is seen for cases with $dRe_\tau^\star/dy > 0$ (red line and symbols), which show an increase in the mode (10°) and a broadening of the distribution. These results show that lifting of coherent vortical structures reduces for cases with $dRe_\tau^\star/dy < 0$, and increases for $dRe_\tau^\star/dy > 0$. These results are in agreement with findings in previous subsection, where we observed that the streaks were stabilised and do not lift as intensely for cases with $dRe_\tau^\star/dy < 0$, while they lift more intensely for cases with $dRe_\tau^\star/dy > 0$.

The tilting of the structures is indicated in figure 5.12(b). Because the direction of the tilting is coupled to the sign of the streamwise vorticity, and the

events related to positive and negative streamwise vorticity are symmetric, we only show tilting angles for positive streamwise vorticity. Only small changes can be seen for the constant property cases with the mode at approximately $\pm 8°$. For cases with $dRe_\tau^\star/dy < 0$, the mode of the pdf's occurs at $\pm 5°$ and the distributions narrow. The reverse happens for cases with $dRe_\tau^\star/dy > 0$, with the mode at $\pm 11°$ and broader distributions.

We will now summarise the effects related to flows with variable properties and provide a mechanistic description to explain the observed turbulence modulations. In order to avoid switching between different cases, we will only use cases with $dRe_\tau^\star/dy > 0$ (the effects for cases with $dRe_\tau^\star/dy < 0$ are exactly opposite). The increase in magnitude of van Driest transformed mean spanwise vorticity $-d\overline{u}^{\mathrm{vD}}/dy$ increases the mean forcing in spanwise direction, causing the increased tilting of vortical structures. The increased tilting results in stronger streak waviness, which then leads to an increased turbulence activity, enabling the evolution of near-wall structures and the generation of stronger shear layers (Johansson *et al.*, 1991). The increased lifting of both streaks and vortical structures is therefore closely associated with an increase in tilting of the structures. This also explains the increase in shear stress anisotropy, which increases momentum transfer in spite of lower turbulence kinetic energy. Furthermore, the increase in tilting angle also provides a structural interpretation for the increase in the pressure-strain correlation, which acts as a sink in the budget of the streamwise energy equation and therefore redistributes the streamwise turbulence energy in the other two directions. From Jeong *et al.* (1997) it is known that the preferential alignment of structures with respect to streamwise vorticity produces positive values of $\partial u'/\partial x$ within the structure and since p' is negative within the structure, $p'\partial u'/\partial x$ is also negative. Additionally, the spanwise asymmetry results in internal shear layers, where high-speed fluid collides with low-speed fluid, causing a positive p' and a negative $\partial u'/\partial x$, and hence in $p'\partial u'/\partial x < 0$. The modulation in tilting of the structures therefore provides a physical interpretation of the modulated turbulence statistics.

5.3. SUMMARY

Near-wall gradients in $Re_\tau^\star$ result in turbulence modification when compared to constant property cases with similar Re_τ values. Partial success in accounting for this change in turbulence is obtained using the semi-local scaling, which accommodates the changes in viscous scales using local fluid properties. The success of the semi-local scaling is evident for the profiles of Reynolds shear stress and viscous shear stress. However, statistics like rms of vorticity fluctuations,

which are sensitive to the strong non-local interactions of the buffer layer vor-
tical structures with the viscous sublayer, show a poor collapse in the near-wall
region using the semi-local scaling. These strong non-local interactions are ev-
ident from the semi-locally scaled streak spacing that tends to become univer-
sal after $y^\star \approx 12 - 13$, while it deviates significantly in the viscous sublayer for
cases with $dRe_\tau^\star/dy \neq 0$. Furthermore, the failure of the semi-local scaling to
provide a universal collapse also occurs due to structural changes in turbulence
that affect lifting and tilting of quasi-streamwise vortices. These changes influ-
ence the Reynolds stress generation mechanism and the inter-component en-
ergy transfer for turbulent stresses. This fact is evident from the statistics of tur-
bulence anisotropy and joint pdfs of streamwise and wall-normal fluctuations,
both of which shows deviation when comparing cases with different $Re_\tau^\star$ pro-
files. For cases with $dRe_\tau^\star/dy < 0$ the near-wall streamwise anisotropy increases,
while decreasing for cases with $dRe_\tau^\star/dy > 0$. This change in anisotropy is not
a Reynolds number effect, as highlighted by comparison with constant property
turbulent flows at different Re_τ values. The increase in streamwise anisotropy for
cases with $dRe_\tau^\star/dy < 0$ is associated with strengthening of large scale low-speed
streaks in the buffer layer, while the reverse is true for cases with $dRe_\tau^\star/dy >
0$. The joint pdfs of streamwise and wall-normal fluctuations reveals that the
Reynolds shear stress generation is modified for cases with $dRe_\tau^\star/dy \neq 0$. We
showed that low-speed streaks are stabilised and do not lift as intensely for cases
with $dRe_\tau^\star/dy < 0$. The reverse happens for cases with $dRe_\tau^\star/dy > 0$, with low-
speed streaks weakening and lifting more intensely away from the wall.

These changes in Reynolds stress generation mechanism are further moti-
vated by investigating the influence of $Re_\tau^\star$ gradients on near-wall vortical struc-
tures. The orientation of these structures is determined using real eigenvector
of the instantaneous velocity gradient tensor at the vortex centre. Similar to tur-
bulence statistics, the orientation of these structures is also strongly governed
by $Re_\tau^\star$ profile and their dependence on individual density and viscosity profile
is negligible. Cases with $dRe_\tau^\star/dy > 0$ show an inflection point in $\overline{u}^{\mathrm{vD}}$, causing
a higher strain with respect to the wall. This higher strain increases the mean
forcing in spanwise direction, which results in an increase in tilting of quasi-
streamwise vortices. The increased tilting of the structures increases the asym-
metry of the streaks, which are known to play an important role in maintain-
ing the near-wall cycle and generation of strong shear layers (Johansson *et al.*,
1991). This increased turbulence activity also causes an increased lifting of the
structures and explains why cases with $dRe_\tau^\star/dy > 0$ show an increased momen-
tum transfer in spite of lower turbulence kinetic energy. The increase in tilting of
the structures also provides a physical interpretation for the increase in negative
pressure-strain, which enables transfer of streamwise fluctuation energy towards

spanwise and wall-normal components (Jeong *et al.*, 1997). The opposite is true for cases with $dRe_\tau^\star/dy < 0$. It should be noted that although semi-local scaling fails to provide a universal collapse for the above mentioned statistics, the reasons behind this failure are very well incorporated in the framework developed in Chapter 3, which only suggests universality for a given $Re_\tau^\star$ profile.

6

SCALING CHARACTERISTICS OF SCALAR FIELD

6.1. Introduction

One of the important aspects in understanding turbulent scalar transport is to determine the analogy between scalar and momentum transport. This results in a simple modeling approach where the turbulent scalar flux is determined using the turbulent eddy/momentum viscosity μ_t and a turbulent Prandtl number Pr_t (or turbulent Schmidt number Sc_t, if the scalar is a concentration field), which is defined as the ratio of eddy viscosity μ_t to eddy conductivity α_t. A significant amount of research effort has, therefore, been devoted in determining the turbulent Prandtl/Schmidt number in flows with passive scalars. DNS has enabled scalar statistics in the near-wall region to be determined more accurately which is challenging to measure with experiments. Kim & Moin (1989) performed DNS of channel flows with Prandtl numbers of $Pr_w = 0.1, 0.71, 2$ and a friction Reynolds number of $Re_\tau = 180$. They observed that Pr_t does not change significantly for cases with $Pr_w = 0.71$ and 2. Kawamura *et al.* (1998) performed DNS of turbulent heat transfer in a channel for various Prandtl numbers, ranging from $Pr_w = 0.025$ to 5 at $Re_\tau = 180$. For fluids with $Pr_w > 0.1$, the turbulent Prandtl number was found to be independent of Pr_w, with values of the order of unity in the regions away from the centre. Schwertfirm & Manhart (2007) performed DNS with Schmidt number Sc_w up to 50 and found that near the wall Sc_t increases for higher Sc_w. However, this increase is in regions where turbulent transport is negligible and therefore not important for mean scalar profiles. Kawamura *et al.* (1999) studied the effect of varying $Re_\tau (=180,395)$ and $Pr_w (=0.025, 0.2, 0.71)$ in a channel and found that Pr_t is independent of Re_τ and Pr_w, if $Pr_w > 0.2$. Pirozzoli *et al.* (2016) extended DNS of passive scalars in channel flows to $Re_\tau \approx 4000$, with $Pr_w = 0.2, 0.71, 1$. The turbulent Prandtl number was found to be nearly constant in the lower 50% of the half-channel, regardless of the Reynolds and Prandtl number. The slope of the log-law for the mean scalar profile, which also is directly related to the turbulent Prandtl number, was found to be $1/0.46$.

In applications with large temperature differences, the variations of temperature dependent thermophysical property can be strong. In such cases the thermophysical property variations can modulate turbulence and the traditional approach of treating temperature as a passive scalar no longer holds. Although turbulence modulation in a turbulent channel flow due to variable thermophysical properties has been investigated in great detail in high-Mach number flows (Coleman *et al.*, 1995; Lechner *et al.*, 2001; Foysi *et al.*, 2004; Modesti & Pirozzoli, 2016) and in low-Mach number flows (Zonta *et al.*, 2012; Nicoud & Poinsot, 1999), the effect of property variations on scalar transport is not well understood. Lee *et al.* (2014) studied the influence of wall-heating on turbulent thermal bound-

ary layers with variable viscosity and observed variations in mean scalar, scalar fluctuation and scalar flux, relative to a reference isothermal flow. In order to account for an inhomogeneous Prandtl number distribution, they proposed to modify Kader's relation (Kader, 1981) for the mean scalar profile by incorporating both the local Prandtl number and the Prandtl number at the the inner edge of the log-layer.

In the previous chapters, it was shown that the leading order effects of property variations on near-wall turbulence are well parametrized using the semi-local friction Reynolds number $Re_\tau^\star$. It accounts for changes in viscous scales due to property variations and also provides a measure of near-wall turbulence modulation with respect to a constant property case. For example, cases with $dRe_\tau^\star/dy < 0$ in the near-wall region show an increased streamwise anisotropy, which alters the Reynolds-stress generation mechanism and modifies the near-wall universality of turbulence. The influence of this structural change on the universality of the viscous shear stress as a function of semi-local wall coordinate $y^\star$ was shown to be negligible, which was then used to derive a universal velocity transformation. In this chapter, we discuss the influence of variable properties on scaling of turbulent temperature statistics.

6.2. CASE DESCRIPTION

In addition to the previous simulations with variable density and viscosity, we introduce cases where also the thermal conductivity changes as a function of temperature. A summary of these cases is given in table 6.1. The functional relations for ρ/ρ_w, μ/μ_w and λ/λ_w as a function of T/T_w are given in the second, third and fourth columns, respectively. The fifth column reports the value of the local mean Prandtl number

$$Pr^\star = Pr_w \frac{(\overline{\mu}/\mu_w)}{\left(\overline{\lambda}/\lambda_w\right)}, \qquad (6.1)$$

at the channel centre and is denoted as $Pr_c^\star$. The semi-local Reynolds number at the channel centre, denoted as $Re_{\tau\,c}^\star$, is given in the sixth column. Note, at the wall $Re_{\tau\,w}^\star = Re_\tau$ and $Pr_w^\star = Pr_w$. For all simulations, c_p is considered to be constant and the reference Reynolds number Re_τ is taken to be 395. The reference Pr_w for all variable property cases is taken to be unity. Cases CP395$_{Pr1}$ and CP395$_{Pr4}$ correspond to constant property cases with a Prandtl number of 1 and 4, respectively. C$Re_\tau^\star$ refers to a variable property case whose density and viscosity are proportional to $1/T$ and $\sqrt{1/T}$, respectively, such that $Re_\tau^\star$ remains constant across the whole channel. Case C$Re_\tau^\star$CPr* has a similar temperature

Case	ρ/ρ_w	μ/μ_w	λ/λ_w	$Pr_c^\star$	$Re_{\tau\,c}^\star$
$CP395_{Pr1}$	1	1	1	1	395
$CRe_\tau^\star$	$(T/T_w)^{-1}$	$(T/T_w)^{-0.5}$	1	0.71	395
$CRe_\tau^\star CPr^\star$	$(T/T_w)^{-1}$	$(T/T_w)^{-0.5}$	$(T/T_w)^{-0.5}$	1	395
$SRe_{\tau GL}^\star$	1	$(T/T_w)^{1.2}$	1	2.6	152
GL	$(T/T_w)^{-1}$	$(T/T_w)^{0.7}$	1	1.8	142
$GLCPr^\star$	$(T/T_w)^{-1}$	$(T/T_w)^{0.7}$	$(T/T_w)^{0.7}$	1	159
LL	1	$(T/T_w)^{-1}$	1	0.56	703
$V\lambda SPr_{LL}^\star$	1	1	(T/T_w)	0.56	395
$CP395_{Pr4}$	1	1	1	4	395

Table 6.1: Simulation parameters for all cases. $CP395_{Pr1}$ - constant property case with $Re_\tau = 395$ and $Pr_w = 1$; $CRe_\tau^\star$ - variable property case with constant $Re_\tau^\star$ (= 395) across the channel; $CRe_\tau^\star CPr^\star$ - variable property case with constant $Re_\tau^\star$ (= 395) and $Pr^\star$ (= 1) across the channel; GL - case with gas-like density and viscosity variation; $SRe_{\tau GL}^\star$ - variable property case with $Re_\tau^\star$ similar to case GL; $GLCPr^\star$ - case with gas-like density and viscosity variations and constant $Pr^\star$ (= 1) across the channel; LL - case with liquid-like viscosity variations; $V\lambda SPr_{LL}^\star$ - case with variable thermal conductivity and $Pr^\star$ similar to case LL; $CP395_{Pr4}$ - constant property case with $Re_\tau = 395$ and $Pr_w = 4$.

Case	$(\Delta x/\eta_\theta)_{max}$	$(\Delta(y)_{min}/\eta_\theta)_{max}$	$(\Delta(y)_{max}/\eta_\theta)_{max}$	$(\Delta z/\eta_\theta)_{max}$
$CP395_{Pr1}$	6.98	0.69	0.89	3.49
$CRe_\tau^\star$	7	0.7	0.74	3.5
$CRe_\tau^\star CPr^\star$	7	0.7	0.88	3.5
$SRe_{\tau GL}^\star$	10.78	0.64	0.69	4.31
GL	10.8	0.64	0.55	4.31
$GLCPr^\star$	10.82	0.65	0.45	4.32
LL	5.6	0.68	0.77	2.8
$V\lambda SPr_{LL}^\star$	6.98	0.69	0.66	3.49
$CP395_{Pr4}$	10.35	0.75	1.34	5.17

Table 6.2: Maximum spatial resolution, normalized by the Batchelor scale $\eta_\theta = \eta/\sqrt{Pr^\star}$.
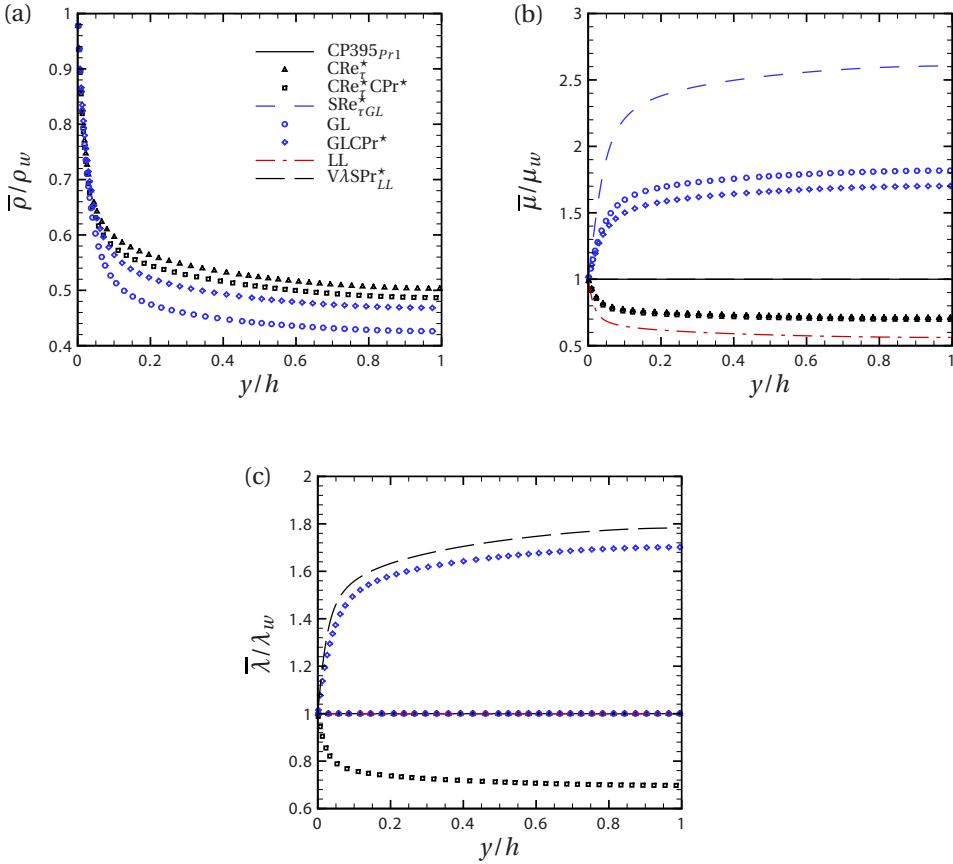
Figure 6.1: Averaged (a) density $\overline{\rho}/\rho_w$, (b) viscosity $\overline{\mu}/\mu_w$, and (c) thermal conductivity $\overline{\lambda}/\lambda_w$ as a function of wall-normal distance y/h.

dependency for ρ and μ as case $CRe_\tau^\star$, while also allowing thermal conductivity to be temperature dependent and equal to viscosity, making the local mean Prandtl number constant across the whole channel. GL corresponds to a gas-like density and viscosity variation. Case $GLCPr^\star$ has a similar temperature dependency for ρ and μ as case GL and in addition has a constant $Pr^\star$ across the channel. $SRe_{\tau GL}^\star$ refers to a case that has a similar $Re_\tau^\star$ distribution as case GL. LL corresponds to a case with a liquid-like μ variation. $V\lambda SPr_{LL}^\star$ corresponds to a case with thermal conductivity directly proportional to temperature, such that its $Pr^\star$ varies but is similar to that of case LL.

Table 6.2 lists the maximum grid spacing in terms of the Batchelor scale $\eta_\theta = \eta/\sqrt{Pr^\star}$ (with η the Kolmogorov scale) for all cases. The values are within the
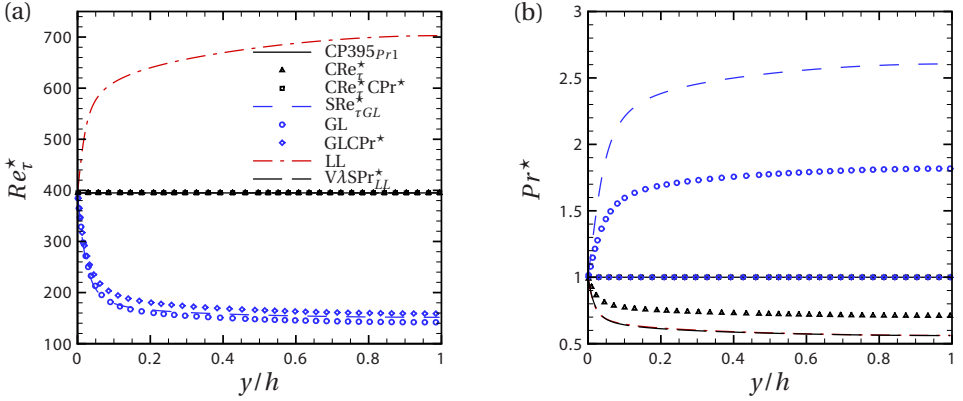
Figure 6.2: (a) Semi-local Reynolds number $Re_\tau^\star$ and (b) local Prandtl number $Pr^\star$ as a function of wall-normal distance y/h.

resolution requirements of $\Delta x < 12\eta_\theta$, $\Delta y < 2\eta_\theta$, $\Delta z < 6\eta_\theta$, as also reported in other DNS studies (Zonta *et al.*, 2012; Lee *et al.*, 2013).

Figure 6.1 shows the distributions of averaged density, viscosity and thermal conductivity for all cases (except CP395$_{Pr4}$). Considerable variations in ρ, μ and λ are obtained. Cases with variable density are shown as symbols and cases with constant density are shown as lines. Figure 6.2 shows the distributions of $Re_\tau^\star$ and $Pr^\star$. Cases CP395$_{Pr1}$, CP395$_{Pr4}$, CRe$_\tau^\star$, CRe$_\tau^\star$CPr* and VλSPr$_{LL}^\star$ with constant $Re_\tau^\star$ across the channel are shown in black. Cases SRe$_{\tau GL}^\star$, GL and GLCPr* with $Re_\tau^\star$ decreasing away from the wall are shown in blue. Case LL with $Re_\tau^\star$ increasing away from the wall is shown in red.

6.3. Scalar statistics

As shown in Chapter 4, the semi-local wall coordinate $y^\star$ is effective in accommodating changes in viscous scales due to variable properties, thus providing a meaningful representation for the velocity statistics. Therefore, all wall-normal profiles are plotted as a function of $y^\star$ in the present chapter.

Conventional mean scalar scaling

The profile of mean transformed temperature

$$\theta = T - T_w, \tag{6.2}$$

Figure 6.3: (a) Mean temperature normalized by friction temperature and (b) van Driest transformed temperature, plotted as a function of $y^\star$.

normalized by the friction temperature

$$\theta_\tau = \frac{q_w}{\rho_w c_{pw} u_\tau},$$ (6.3)

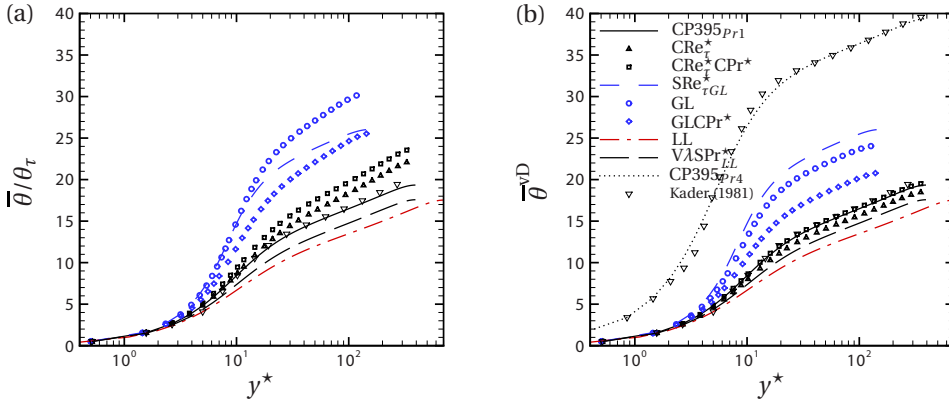where q_w is the wall heat flux, is shown in figure 6.3(a) for all cases (except CP395$_{Pr4}$). The constant property case CP395$_{Pr1}$ compares well with the correlation from Kader (1981), while all other cases deviate significantly. Using the van Driest transformed temperature profile $\overline{\theta}^{\text{vD}} = \int_0^{\overline{\theta}/\theta_\tau} \sqrt{\overline{\rho}/\rho_w} d\left(\overline{\theta}/\theta_\tau\right)$, shown in figure 6.3(b), case CRe$_\tau^\star$CPr* (for which both $Re_\tau^\star$ and $Pr^\star$ are a constant) shows a good collapse with case CP395$_{Pr1}$. Unlike the $\overline{u}^{\text{vD}}$ profiles, which for cases with constant $Re_\tau^\star$ collapse with constant property cases, a collapse of $\overline{\theta}^{\text{vD}}$ additionally requires $Pr^\star$ to remain constant. This can be seen for case CRe$_\tau^\star$ and VλSPr$_{LL}^\star$, for which $Re_\tau^\star$ is a constant but $Pr^\star$ varies, therefore showing deviation from case CP395$_{Pr1}$. A Prandtl-number-dependent shift also occurs when comparing profiles of $\overline{\theta}/\theta_\tau$ for constant property cases at different Prandtl numbers as can be seen by comparing case CP395$_{Pr1}$ with CP395$_{Pr4}$ (also see for e.g. Kawamura *et al.*, 1998). Similar to $\overline{u}^{\text{vD}}$, which does not collapse for cases with $Re_\tau^\star$ gradients, $\overline{\theta}^{\text{vD}}$ also deviates significantly for cases with $Re_\tau^\star$ gradients. This can be seen for the case GLCPr*, for which $Pr^\star$ is constant and $Re_\tau^\star$ varies. Cases SRe$_{\tau GL}^\star$, GL and LL experience the combined effect of variations in both $Pr^\star$ and $Re_\tau^\star$.

Lee *et al.* (2014), who investigated heated turbulent boundary layers with variable viscosity, proposed a modification to Kader's original relation (Kader,

1981) for the mean scalar distribution by accounting for variations in local Prandtl number. The relation is given as

$$\overline{\theta}^{vD} = Pr^{\star} y^{\star} \exp\left(-\Gamma\right) + \left\{2.12\ln\left[\left(1+y^{\star}\right)\frac{1.5\left(2-y/h\right)}{1+2\left(1-y/h\right)^2}\right] + \beta(Pr_v)\right\}\exp(-1/\Gamma),$$
(6.4)

with

$$\beta(Pr_v) = \left(3.85 Pr_v^{1/3} - 1.3\right)^2 + 2.12\ln Pr_v$$
(6.5)

and

$$\Gamma = \frac{10^{-2}\left(Pr^{\star} y^{\star}\right)^4}{1+5Pr^{\star 3}y^{\star}} \quad \text{and} \quad Pr_v = Pr^{\star}(y^{\star} \approx 30).$$
(6.6)

They proposed that except for the definition of β, all Pr values in the original relation by Kader should be replaced by $Pr^{\star}$ and the inner-scaled wall coordinate should be $y^{\star}$ instead of y^+. For defining β, which determines the elevation of the log-law, they proposed to use the Prandtl number at the start of the log region $Pr_v = Pr^{\star}(y^{\star} \approx 30)$. A comparison of the proposed relation for selected cases is shown in figure 6.4(a). A close approximation is provided for cases with decreasing $Re_{\tau}^{\star}$ and increasing $Pr^{\star}$ (SRe$_{\tau GL}^{\star}$, GL) or vice versa (LL). The prediction for cases where only one of the parameters ($Re_{\tau}^{\star}$ or $Pr^{\star}$) varies (CRe$_{\tau}^{\star}$, GLCPr*, VλSPr$_{LL}^{\star}$) is in general poor. This can be clearly seen for case GLCPr*, where because of constant $Pr^{\star}$, equation (6.4) provides a similar distribution as case CP395$_{Pr1}$. However, $\overline{\theta}^{vD}$ for GLCPr* is much higher. This non-universal behavior can be attributed to the fact that equation (6.4) assumes that the slope of the log-law is unaffected by property variations, which is not the case for cases with $Re_{\tau}^{\star}$ gradients as can be seen by the diagnostic function that is related with the inverse of the slope of the log-law k_{θ} as

$$\frac{1}{k_{\theta}} = y^{\star}\frac{d\overline{\theta}^{vD}}{dy^{\star}}.$$
(6.7)

A plot of k_{θ} is shown in figure 6.4(b). It is noticeable that k_{θ} increases with increasing $Re_{\tau}^{\star}$ and decreases with decreasing $Re_{\tau}^{\star}$. Clearly, the distribution of $\overline{\theta}^{vD}$ is influenced by $Re_{\tau}^{\star}$ gradients.

$Re_{\tau}^{\star}$ INVARIANT MEAN SCALAR SCALING

In order to account for $Re_{\tau}^{\star}$ variations and to further investigate the characteristics of mean temperature profiles, we first introduce the mean heat flux equation. The relation for the wall-normal turbulent heat flux and conductive heat
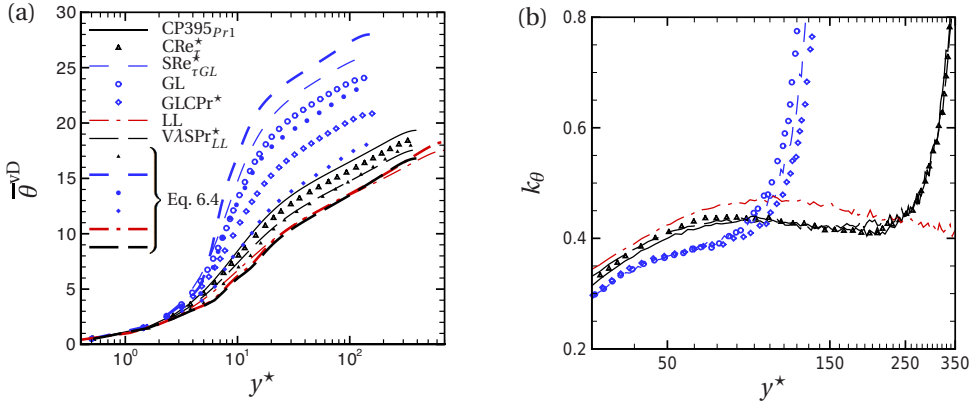
Figure 6.4: (a) van Driest transformed temperature compared with the modified Kader correlation as suggested by Lee *et al.* (2014) and (b) von Karman constant k_θ for the van Driest transformed temperature profile, plotted as a function of $y^\star$.

flux can be obtained by integrating the mean energy equation, which for a fully developed turbulent channel flow, can be written as

$$-\frac{\overline{\rho\widetilde{v''\theta''}}}{\rho_w u_\tau \theta_\tau} + \frac{h}{Re_\tau Pr_w}\left(\frac{\overline{\lambda}}{\lambda_w}\right)\frac{d\left(\overline{\theta}/\theta_\tau\right)}{dy} + \frac{h}{Re_\tau}\overline{\left(\frac{\lambda'}{\lambda_w}\right)\frac{d\left(\theta'/\theta_\tau\right)}{dy}} = \left(1-\frac{y}{h}\right). \qquad (6.8)$$

Neglecting the thermal conductivity fluctuations in equation (6.8) gives

$$-\frac{\overline{\rho\widetilde{v''\theta''}}}{\rho_w u_\tau \theta_\tau} + \frac{h}{Re_\tau Pr_w}\left(\frac{\overline{\lambda}}{\lambda_w}\right)\frac{d\left(\overline{\theta}/\theta_\tau\right)}{dy} \approx \left(1-\frac{y}{h}\right). \qquad (6.9)$$

Using the turbulent eddy conductivity

$$\alpha_t = -\frac{\overline{\rho\widetilde{v''\theta''}}}{\left(\frac{d\overline{\theta}}{dy}\right)}, \qquad (6.10)$$

equation (6.9) can be written as,

$$\left(\frac{\alpha_t}{\mu_w} + \frac{1}{Pr_w}\left(\frac{\overline{\lambda}}{\lambda_w}\right)\right)\frac{h}{Re_\tau}\frac{d\left(\overline{\theta}/\theta_\tau\right)}{dy} \approx \left(1-\frac{y}{h}\right). \qquad (6.11)$$

Figure 6.5: (a) Conductive heat flux and (b) turbulent eddy conductivity normalized by mean viscosity, plotted as a function of $y^\star$.

The above equation can then further be expressed in terms of semi-local parameters, $Re_\tau^\star$ and $Pr^\star$, and the van Driest mean temperature increment as

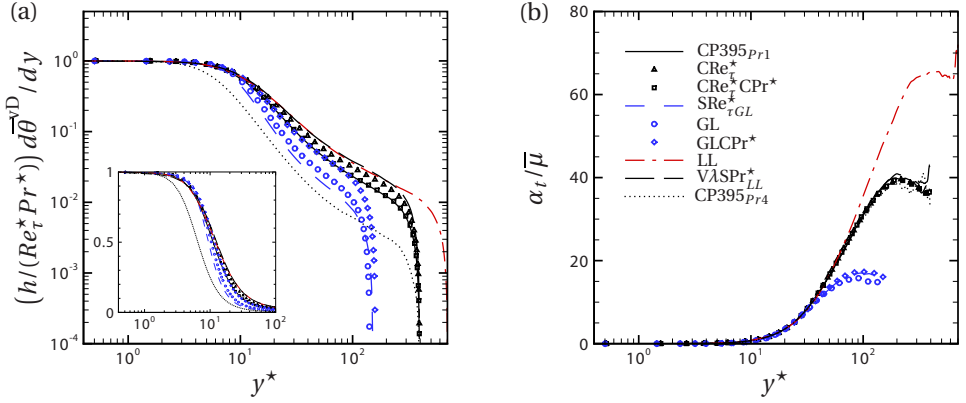$$d\overline{\theta}^{\text{vD}} = \sqrt{\frac{\overline{\rho}}{\rho_w}} d\left(\frac{\overline{\theta}}{\theta_\tau}\right),$$

(6.12)

to give

$$\left(\frac{\alpha_t}{\overline{\mu}} + \frac{1}{Pr^\star}\right)\frac{h}{Re_\tau^\star}\frac{d\overline{\theta}^{\text{vD}}}{dy} \approx \left(1 - \frac{y}{h}\right).$$

(6.13)

A plot of the conductive heat flux $\left(h/(Re_\tau^\star Pr^\star)\right)d\overline{\theta}^{\text{vD}}/dy$, as a function of $y^\star$ is shown in figure 6.5(a). The plot provides a measure of the conductive sublayer thickness. For constant property cases, it can be clearly seen that the conduction dominated region reduces for case CP395_{Pr4}, when compared with case CP395_{Pr1}. For variable property cases, an increase in $Pr^\star$ towards the channel centre (cases $\text{SRe}_{\tau GL}^\star$ and GL) reduces the thickness of the conduction dominated region in terms of $y^\star$, while the reverse happens when $Pr^\star$ decreases (cases $\text{CRe}_\tau^\star$, LL and $\text{V}\lambda\text{SPr}_{LL}^\star$). The case $\text{GLCPr}^\star$ with constant $Pr^\star = 1$ and variable $Re_\tau^\star$, shows a good collapse with case CP395_{Pr1} over the entire inner layer. This behavior is similar to constant property cases with the same Pr_w, but different Re_τ values (see for e.g. Kawamura *et al.*, 1999). Similarly, cases LL and $\text{V}\lambda\text{SPr}_{LL}^\star$, which exhibit quasi-similar $Pr^\star$ profiles, also show quasi-similar conductive heat flux profiles, despite the different $Re_\tau^\star$ profiles. All the above observations can be summarized mathematically by investigating the scaling characteristics of the turbulent eddy conductivity. A plot of $\alpha_t/\overline{\mu}$ as a function of

$y^\star$ in figure 6.5(b), shows a reasonable collapse in the inner layer for all cases. While we will discuss this collapse later in more detail, the direct implication of this collapse will be discussed first. Since, in the overlap region, located between the buffer layer and the channel core, the turbulent mixing dominates (i.e., $\alpha_t/\overline{\mu} \gg 1/Pr^\star$, and the inner scaling applies), equation (6.13) and figure 6.5(b) gives

$$\frac{h}{Re_\tau^\star} \frac{d\overline{\theta}^{\mathrm{vD}}}{dy} = \Phi(y^\star), \tag{6.14}$$

where Φ is an unknown function of $y^\star$. A plot of the van Driest temperature gradient normalized by the semi-local length scale is shown in figure 6.6(a) as a function of $y^\star$. A good collapse is obtained in the entire inner layer, except in regions where molecular effects are dominant ($y^\star < 30$ for the present cases). The effectiveness of this collapse can be used to extend the van Driest transformed temperature to provide a temperature profile that exhibits similar characteristics as the ones of a constant property case. Following a similar procedure we used to derive $\overline{u}^\star$, equation (6.14) can be written as

$$\frac{h}{Re_\tau^\star} \left(\frac{dy^\star}{dy}\right) \frac{d\overline{\theta}^{\mathrm{vD}}}{dy^\star} = \Phi(y^\star). \tag{6.15}$$

$dy^\star/dy$ can be obtained by taking the derivative of $y^\star = yRe_\tau^\star/h$ with respect to y, to obtain

$$\left(1 + \frac{y}{Re_\tau^\star} \frac{dRe_\tau^\star}{dy}\right) \frac{d\overline{\theta}^{\mathrm{vD}}}{dy^\star} = \Phi(y^\star). \tag{6.16}$$

Equation (6.16) can then be written in terms of the extended van Direst temperature profile $d\overline{\theta}^\star$ as

$$\frac{d\overline{\theta}^\star}{dy^\star} = \left(1 + \frac{y}{Re_\tau^\star} \frac{dRe_\tau^\star}{dy}\right) \frac{d\overline{\theta}^{\mathrm{vD}}}{dy^\star} = \Phi(y^\star). \tag{6.17}$$

The last equality in this equation is valid only in the overlap region. In the region close to the wall (assuming a constant heat flux region), $d\overline{\theta}^\star/dy^\star$ is given as

$$\frac{d\overline{\theta}^\star}{dy^\star} = \frac{h}{Re_\tau^\star} \frac{d\overline{\theta}^{\mathrm{vD}}}{dy} = \frac{1}{\left(\frac{\alpha_t}{\overline{\mu}} + \frac{1}{Pr^\star}\right)}. \tag{6.18}$$

Therefore, $\overline{\theta}^\star = \int_0^{\overline{\theta}^{\mathrm{vD}}} \left(1 + \left(y/Re_\tau^\star\right) dRe_\tau^\star/dy\right) d\overline{\theta}^{\mathrm{vD}}$ (obtained by integrating from the wall), exhibits a $Pr^\star$ dependent shift. A plot of $\overline{\theta}^\star$, as a function of $y^\star$, is shown in figure 6.6(b). It can be seen that all cases with $Pr^\star = 1$ (CP395$_{Pr1}$,
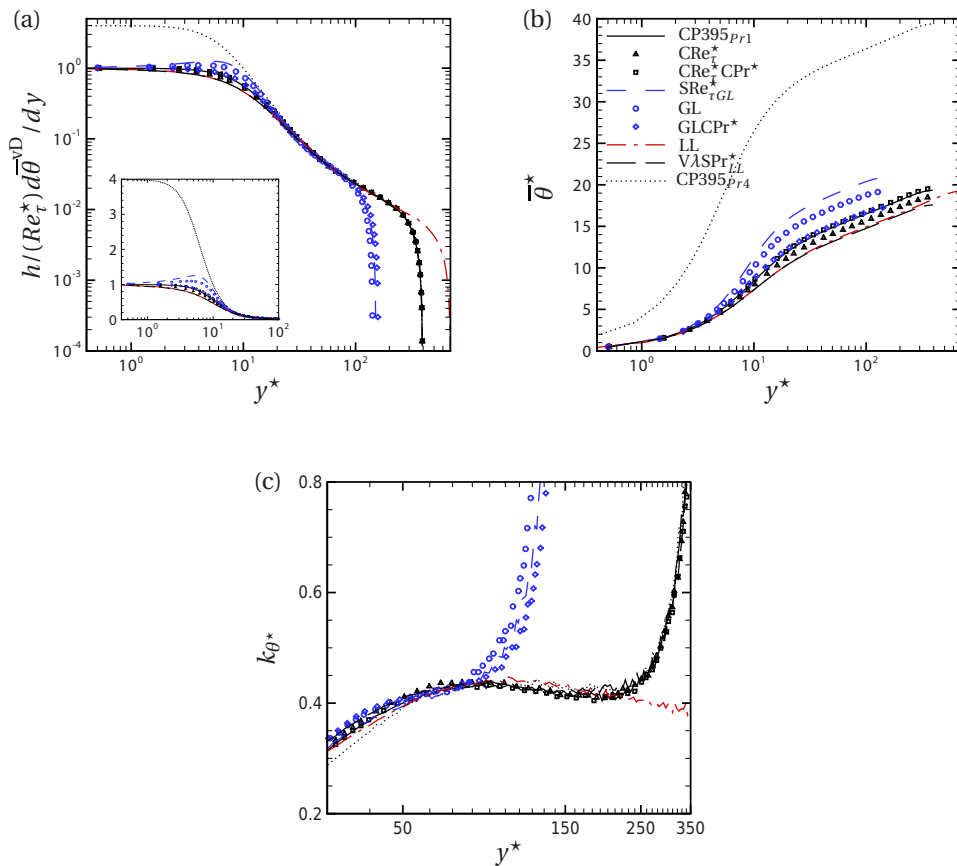
Figure 6.6: (a) van Driest temperature gradient normalized by the semi-local viscous length scale, (b) extended van Driest transformed temperature and (c) von Karman constant $k_{\theta\star}$ for the extended van Driest transformed temperature profile, plotted as a function of $y^\star$.

$\text{CRe}_\tau^\star\text{CPr}^\star$ and GLCPr*) show a reasonable collapse, irrespective of the $Re_\tau^\star$ profile. Similarly, case LL and VλSPr$_{LL}^\star$, with quasi-similar $Pr^\star$ variations, exhibit similar $\overline{\theta}^\star$ profiles. Additionally, all cases exhibit a similar slope in the log-law region, which can be seen by the plot of the inverse of the log-law slope $k_{\theta^\star}$, given by

$$\frac{1}{k_{\theta^\star}} = y^\star \frac{d\overline{\theta}^\star}{dy^\star}, \tag{6.19}$$

which is shown in figure 6.6(c). $\overline{\theta}^\star$ therefore exhibits all characteristics of a constant property scalar distribution (for $Pr_w > 0.2$), which also have a Prandtl-number-dependent shift and similar slope in the log-law region, irrespective of their Re_τ and Pr_w values. The origin of the log-law region in terms of $y^\star$, is also found to remain invariant for the cases presented herein.

TURBULENT PRANDTL NUMBER

The success of the extended van Driest transformed temperature $\overline{\theta}^\star$ is further investigated by studying the analogy between momentum and scalar transfer. In chapter 4 we showed that the viscous stress $h/Re_\tau^\star(d\overline{u}^{\text{vD}}/dy)$ collapses reasonably well when plotted as a function of $y^\star$. For the near wall constant stress layer, this collapse can be written in terms of the turbulent eddy viscosity μ_t as

$$\frac{h}{Re_\tau^\star} \frac{d\overline{u}^{\text{vD}}}{dy} = \frac{1}{\left(\frac{\mu_t}{\overline{\mu}} + 1\right)} = \Psi(y^\star), \tag{6.20}$$

where Ψ is an unknown function of $y^\star$. This results in $\mu_t/\overline{\mu}$ to be a universal function of $y^\star$ in the inner layer. A plot of $\mu_t/\overline{\mu}$ is shown along with $\alpha_t/\overline{\mu}$ as a function of $y^\star$ in figure 6.7(a). It can be seen that the profiles of $\mu_t/\overline{\mu}$ and $\alpha_t/\overline{\mu}$ behave similar, showing a strong analogy between turbulent momentum and scalar transfer. This is also seen in figure 6.7(b), where the turbulent Prandtl number Pr_t is shown. Pr_t varies slightly around unity in the inner layer, indicating again the strong analogy between momentum and scalar transport. This, along with the universal behavior of $\overline{u}^\star$, is the reason for the success of $\overline{\theta}^\star$.

A closer inspection of the near-wall behavior of $\mu_t/\overline{\mu}$ and $\alpha_t/\overline{\mu}$ shows deviation in the region $y^\star < 10$ for cases with $Re_\tau^\star$ gradients. This deviation in $\mu_t/\overline{\mu}$ was noted earlier in Chapter 4 as a deviation in mixing length and stems from turbulence modulation occurring in cases with $Re_\tau^\star$ gradients, which influence the anisotropy of the turbulence and also alters the Reynolds stress generation mechanism. The influence of this deviation in $\mu_t/\overline{\mu}$ on scaling of $\overline{u}^\star$ was found to be negligible for the present cases, since the deviations were limited to the
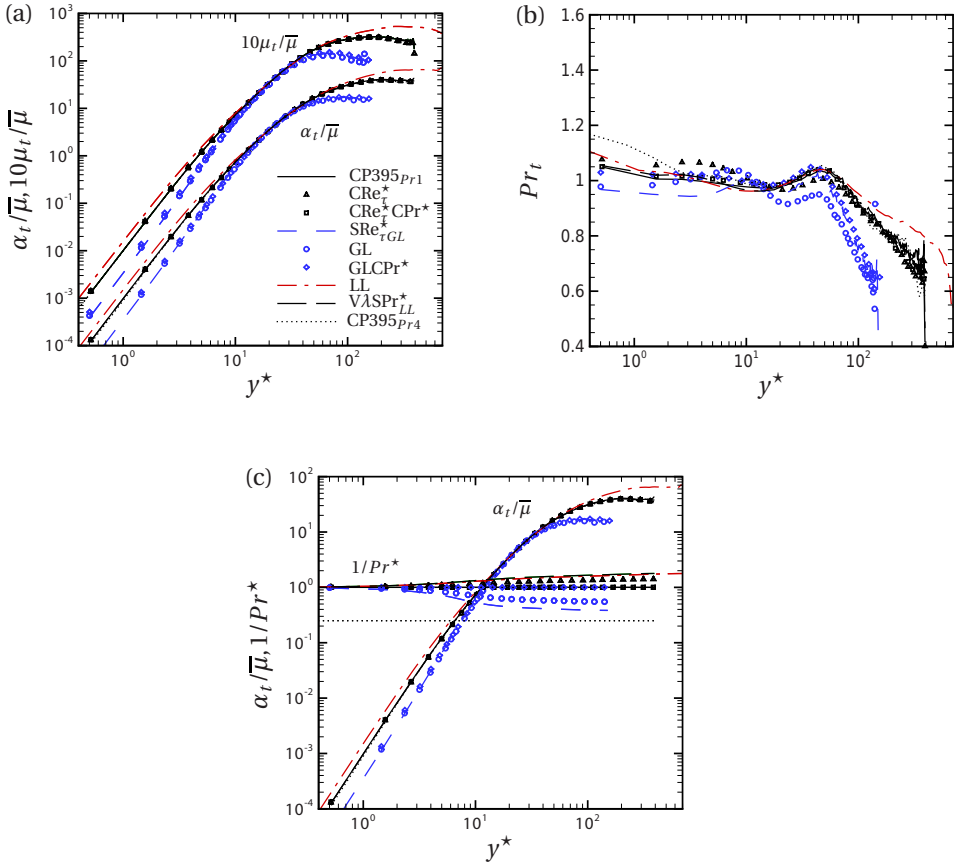
Figure 6.7: (a) Turbulent eddy conductivity and turbulent eddy viscosity (multiplied by 10 for visualization purposes) normalized by mean viscosity, (b) turbulent Prandtl number and (c) turbulent eddy conductivity normalized by mean viscosity and inverse of local mean Prandtl number, plotted as a function of $y^\star$.
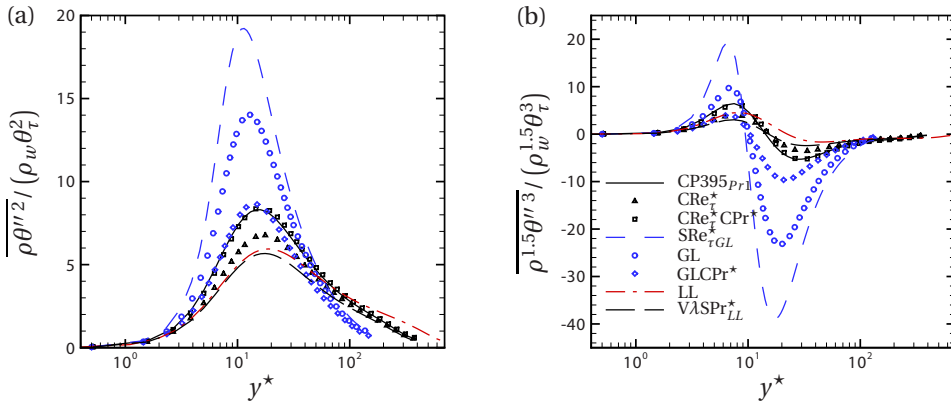
Figure 6.8: (a) Second order and (b) third order temperature fluctuations, plotted as a function of $y^\star$.

viscous dominated region. A similar analysis is done for $\overline{\theta}^\star$ in figure 6.7(c) by comparing $\alpha_t/\overline{\mu}$ with $1/Pr^\star$. It can be seen that for the present cases the influence of turbulence modulation does not influence $\overline{\theta}^\star$ and its shift in the overlap layer is only because of $Pr^\star$. However, this change in near-wall behavior of $\alpha_t/\overline{\mu}$ for cases with $Re_\tau^\star$ gradients could play a crucial role in scalar transport for high Prandtl number fluids, for which the cross-over point between $1/Pr^\star$ and $\alpha_t/\overline{\mu}$ moves closer to the wall.

HIGHER ORDER SCALAR STATISTICS

Higher order statistics of the scalar field will be discussed next. Using the semi-local framework, the appropriate form of second and third order temperature fluctuations involve a density weighted correction and are given by $\overline{\rho\theta''^2}/\left(\rho_w\theta_\tau^2\right)$ (figure 6.8(a)) and $\overline{\rho^{1.5}\theta''^3}/\left(\rho_w^{1.5}\theta_\tau^3\right)$ (figure 6.8(b)), respectively. From constant property studies (Kawamura *et al.*, 1999) it is known that the scalar fluctuation statistics show a strong Prandtl number dependency, while the Reynolds number dependency, although present, is weak. A similar behavior can be seen for the present cases, where for cases with increasing $Pr^\star$ (SRe$_{\tau GL}^\star$ and GL) the peaks become more pronounced, while the reverse happens for cases with decreasing $Pr^\star$ (CRe$_\tau^\star$, LL, VλSPr$_{LL}^\star$). The statistics for cases with constant $Pr^\star$ show a good collapse only when the $Re_\tau^\star$ profiles are also similar (see for e.g. cases CP395$_{Pr1}$ and CRe$_\tau^\star$CPr*), while small deviations are observed when $Re_\tau^\star$ differs (see for e.g. CP395$_{Pr1}$ and GLCPr*). This $Re_\tau^\star$ dependent deviation is even more pro-

nounced for third order statistics. Similar observations can be made for cases
LL and VλSPr$^\star_{LL}$, which have quasi-similar $Pr^\star$ but different $Re^\star_\tau$. Although not
shown here, it should be noted that similar to statistics of velocity fluctuations,
it was found that $\overline{\rho\theta''^2} \approx \overline{\rho}\,\overline{\theta''^2}$, but $\overline{\rho^{1.5}\,\theta''^3} \neq \overline{\rho^{1.5}}\,\overline{\theta''^3}$. This importance of in-
corporating density fluctuations in third order moments occurs because of the
functional relation of density with temperature, which results in a preferential
concentration of a high density fluid in a low temperature streak, and vice versa.

6.4. SUMMARY

Variable property cases with different relations for density, viscosity and ther-
mal conductivity as a function of temperature are studied to analyze scal-
ing of a turbulent scalar field. In addition to the distribution of the semi-
local Reynolds number $Re^\star_\tau$, the distribution of the local Prandtl number
$Pr^\star \equiv Pr_w(\overline{\mu}/\mu_w)/(\overline{\lambda}/\lambda_w)$ plays an important role in scaling of scalar statis-
tics. The van Driest transformed mean temperature profiles $\overline{\theta}^{\text{vD}}$, for variable
property cases collapse with the constant property mean scalar distribution
(with Prandtl number Pr_w) only when their $Re^\star_\tau$ and $Pr^\star$ distributions are con-
stant across the channel. Near-wall gradients in $Re^\star_\tau$ result in deviations of $\overline{\theta}^{\text{vD}}$,
even if $Pr^\star$ is constant. An extended van Driest transformation for the mean
temperature profile, $d\overline{\theta}^\star = \left(1 + \left(y/Re^\star_\tau\right)dRe^\star_\tau/dy\right)d\overline{\theta}^{\text{vD}}$ is derived, which is able
to collapse cases with varying $Re^\star_\tau$ and constant $Pr^\star$. For cases with varying
$Pr^\star$ profiles, the thickness of the conduction dominated region changes. The
turbulent diffusivity, however, shows a good collapse in the inner layer (except
in regions with $y^\star < 10$) for all cases, irrespective of $Re^\star_\tau$ and $Pr^\star$ profiles. The
modulation in turbulent diffusivity in regions with $y^\star < 10$ occurs for cases with
gradients in $Re^\star_\tau$ and is associated with modulations in turbulence. However, for
the present cases the influence of this turbulence modulation on $\overline{\theta}^\star$ is negligible
and its shift in the overlap layer is only caused by $Pr^\star$ variations. The $\overline{\theta}^\star$ trans-
formation is analogous to the $\overline{u}^\star$ transformation and follows from the strong
analogy between momentum and scalar transfer, as seen with the turbulent
Prandtl number, which varies slightly around unity in the inner layer. Higher
order statistics also show quasi-similarity for cases with similar $Re^\star_\tau$ and $Pr^\star$
distributions.

7

TURBULENCE MODELING

7.1. INTRODUCTION

The observations made in the previous chapters can be utilized to improve the performance of turbulence models. It was seen that the profile of semi-local Reynolds number $Re_\tau^\star$ governs the wall-normal gradient of van Driest velocity and follows the relation

$$\frac{h}{Re_\tau^\star} \frac{d\overline{u}^{\mathrm{vD}}}{dy} = \Phi(y^\star). \tag{7.1}$$

The wall-normal gradient of van Driest velocity in turn governs the production of semi-locally scaled turbulent fluctuations. Additionally it was seen that the $Re_\tau^\star$ profile also provides a good scaling for the Kolmogorov length scale which is governed by the dissipation of turbulence kinetic energy. These observations suggest that the conventional turbulence model which uses transport equation for turbulence kinetic energy k and dissipation ϵ can be improved to account for variable property effects. We therefore begin by first deriving the transport equation for semi-locally scaled turbulence kinetic energy (SLS TKE) which is consistent with the semi-local framework and has all the features discussed above. We will then use the modeled form of SLS TKE to simulate several fully developed turbulent flows, ranging from volumetrically heated flows at low Mach (Ma) numbers to a fully compressible Ma=4 case in a channel with isothermal walls provided by Trettel & Larsson (2016).

7.2. SEMI-LOCALLY SCALED TURBULENCE KINETIC ENERGY EQUATION (SLS TKE)

As done in Chapter 3, we apply a scaling transformation to the Navier-Stokes equations using semi-local quantities such that the rescaled density, dynamic viscosity, velocity, pressure and spatial coordinate are defined as

$$\hat{\rho} = \frac{\rho}{\overline{\rho}}, \ \hat{\mu} = \frac{\mu}{\overline{\mu}}, \ \hat{u}_i = \frac{u_i}{u_\tau^\star}, \ \hat{p} = \frac{p}{\overline{\rho}u_\tau^{\star 2}}, \text{ and } \hat{x}_i = \frac{x_i}{h}, \tag{7.2}$$

respectively. Assuming that the averaged wall shear stress τ_w is constant or changes slowly in streamwise direction, the semi-locally scaled continuity equation can then be written as

$$t_\tau^\star \frac{\partial \hat{\rho}}{\partial t} + \frac{\partial \hat{\rho}\hat{u}_i}{\partial \hat{x}_i} = -\frac{\hat{\rho}\hat{u}_i}{\overline{\rho}u_\tau^\star} \frac{\partial \overline{\rho}u_\tau^\star}{\partial \hat{x}_i} = -\hat{\rho}\hat{u}_i \underbrace{\frac{1}{2}\frac{1}{\overline{\rho}}\frac{\partial \overline{\rho}}{\partial \hat{x}_i}}_{d_i}, \tag{7.3}$$

where $t_\tau^\star = h/u_\tau^\star$ is the corresponding time scale. The additional term with d_i is a result of the scaling transformation using semi-local quantities, which contains the gradient of the Reynolds averaged density. Accordingly, the semi-locally scaled momentum equations read

$$\hat{\rho} t_\tau^\star \frac{\partial \hat{u}_i}{\partial t} + \hat{\rho} \hat{u}_j \frac{\partial \hat{u}_i}{\partial \hat{x}_j} - \hat{\rho} \hat{u}_i \hat{u}_j d_j = -\frac{\partial \hat{p}}{\partial \hat{x}_i} + \frac{\partial \hat{\tau}_{ij}}{\partial \hat{x}_j} - \frac{\partial \hat{D}_{ij}}{\partial \hat{x}_j}, \qquad (7.4)$$

with the stress tensor $\hat{\tau}_{ij} = \hat{\mu}/Re_\tau^\star \left[(\partial \hat{u}_i/\partial \hat{x}_j + \partial \hat{u}_j/\partial \hat{x}_i) - 2/3(\partial \hat{u}_k/\partial \hat{x}_k)\delta_{ij} \right]$ and $\hat{D}_{ij} = \hat{\mu}/Re_\tau^\star \left[(\hat{u}_i d_j + \hat{u}_j d_i) - 2/3(\hat{u}_k d_k)\delta_{ij} \right]$. Compared to the conventional form, two additional terms appear that result from the scaling transformation using semi-local quantities. Also note that the effective viscosity in the viscous term is proportional to $1/Re_\tau^\star$.

Given equations (7.3) and (7.4), we can now derive the semi-locally scaled turbulence kinetic energy equation (SLS TKE) using a standard procedure by first multiplying the momentum equation (7.4) with the Favre fluctuating velocity $\hat{u}_i''$ and then Reynolds averaging the product. The Reynolds decomposition is used for density, viscosity, pressure and stress tensor, while the Favre decomposition is used for the velocity. To highlight distinct differences in the derivation when using the semi-locally scaled Navier-Stokes equations, this procedure is outlined for the terms on the left-hand-side of equation (7.4),
For the unsteady term we obtain

$$\overline{\hat{u}_i'' \hat{\rho} t_\tau^\star \frac{\partial \hat{u}_i}{\partial t}} = t_\tau^\star \frac{\partial \overbrace{\frac{1}{2}\hat{\rho}\hat{u}_i''\hat{u}_i''}^{\overline{\hat{\rho}\hat{k}} = \tilde{k}}}{\partial t} - \underbrace{\hat{k} t_\tau^\star \frac{\partial \hat{\rho}}{\partial t}}_{(I)}, \qquad (7.5)$$

with the definition of the turbulence kinetic energy $\hat{k} = \hat{u}_i'' \hat{u}_i''/2$. Using Favre averaging, it follows that $\overline{\hat{\rho}\hat{k}} = \overline{\rho \hat{k}}/\overline{\rho} = \tilde{k}$. For the convection term we get,

$$\overline{\hat{\rho}\hat{u}_i''\hat{u}_j \frac{\partial \hat{u}_i}{\partial \hat{x}_j}} = \widetilde{\hat{u}_i''\hat{u}_j''} \frac{\partial \widetilde{\hat{u}_i}}{\partial \hat{x}_j} + \frac{\partial}{\partial \hat{x}_j}\left(\tilde{k}\tilde{u}_j + \widetilde{\hat{u}_j''\hat{k}} \right) - \underbrace{\hat{k}\frac{\partial \overline{\hat{\rho}\hat{u}_j}}{\partial \hat{x}_j}}_{(II)}. \qquad (7.6)$$

The partial derivative of the semi-locally scaled mean velocity in the first term on the right-hand-side of equation (7.6) can be expressed in terms of the van Driest transformed velocity $\partial \tilde{u}_i^{\mathrm{vD}} = \sqrt{\overline{\rho}/\rho_w}\,\partial(\tilde{u}_i/u_{\tau w})$ by using the identity $\sqrt{\rho_w}u_{\tau w} = \sqrt{\overline{\rho}}u_\tau^\star$, which results in

$$\frac{\partial \widetilde{\hat{u}_i}}{\partial \hat{x}_j} = \frac{\partial \frac{\overline{\tilde{u}_i}}{u_\tau^\star}}{\partial \hat{x}_j} = \frac{\partial \sqrt{\frac{\overline{\rho}}{\rho_w}}\frac{\tilde{u}_i}{u_{\tau w}}}{\partial \hat{x}_j} = \frac{\sqrt{\frac{\overline{\rho}}{\rho_w}}\partial\frac{\tilde{u}_i}{u_{\tau w}}}{\partial \hat{x}_j} + \frac{\frac{\tilde{u}_i}{u_{\tau w}}\partial\sqrt{\frac{\overline{\rho}}{\rho_w}}}{\partial \hat{x}_j} = \frac{\partial \tilde{u}_i^{\mathrm{vD}}}{\partial \hat{x}_j} + \widetilde{\hat{u}_i}d_j. \qquad (7.7)$$

The first term on the right-hand-side of equation (7.6) can then be written as the sum of two terms, namely,

$$\widetilde{\hat{u}''_i \hat{u}''_j} \frac{\partial \widetilde{\hat{u}_i}}{\partial \hat{x}_j} = \underbrace{\widetilde{\hat{u}''_i \hat{u}''_j} \frac{\partial \widetilde{u}_i^{\mathrm{vD}}}{\partial \hat{x}_j}}_{-\hat{P}_k} + \underbrace{\widetilde{\hat{u}''_i \hat{u}''_j} \widetilde{u}_i d_j}_{\text{(III)}}, \tag{7.8}$$

with $\hat{P}_k$ as the product of Reynolds stress and van Driest velocity gradient, and an additional term (III) that can be large in magnitude, as it is the product of Reynolds stress, Favre averaged velocity and density gradient. However, as we will see later, this term will cancel. The third term in the momentum equation, multiplied by $\hat{u}''_i$ and Reynolds averaged, gives

$$-\overline{\hat{u}''_i \hat{\rho} \hat{u}_i \hat{u}_j} d_j = -\underbrace{\widetilde{\hat{u}''_i \hat{u}''_j} \widetilde{u}_i d_j}_{\text{(IV)}} - 2\widetilde{\hat{k}} \widetilde{u}_j d_j - 2\widetilde{\hat{u}''_j \hat{k}} d_j \tag{7.9}$$

We can now proceed and sum the individual terms. For example, the addition of (I) + (II) allows to substitute the continuity equation (7.3) and we get

$$-\overline{\hat{k} \left(t_\tau^\star \frac{\partial \hat{\rho}}{\partial t} + \frac{\partial \hat{\rho} \hat{u}_j}{\partial \hat{x}_j} \right)} = \widetilde{\hat{k}} \widetilde{u}_j d_j + \widetilde{\hat{u}''_j \hat{k}} d_j. \tag{7.10}$$

Furthermore, terms (III) and (IV) cancel. Summing up all remaining terms, including the pressure and the viscous terms, results in the semi-locally scaled turbulence kinetic energy equation, given as

$$
\begin{aligned}
t_\tau^\star \frac{\partial \widetilde{\hat{k}}}{\partial t} + \frac{\partial \widetilde{\hat{k}} \widetilde{u}_j}{\partial \hat{x}_j} \;=\; & -\widetilde{\hat{u}''_i \hat{u}''_j} \frac{\partial \widetilde{u}_i^{\mathrm{vD}}}{\partial \hat{x}_j} - \overline{\hat{\tau}'_{ij} \frac{\partial \hat{u}'_i}{\partial \hat{x}_j}} + \frac{\partial}{\partial \hat{x}_j} \left(\overline{\hat{u}'_i \hat{\tau}'_{ij}} - \widetilde{\hat{u}''_j \hat{k}} - \overline{\hat{p}' \hat{u}'_i} \right) \\
& + \overline{\hat{p}' \frac{\partial \hat{u}'_j}{\partial \hat{x}_j}} - \overline{\hat{u}''_j} \frac{\partial \overline{\hat{p}}}{\partial \hat{x}_j} + \overline{\hat{u}''_i} \frac{\partial \overline{\hat{\tau}_{ij}}}{\partial \hat{x}_j} \\
& + \left(\widetilde{\hat{k}} \widetilde{u}_j + \widetilde{\hat{u}''_j \hat{k}} \right) d_j - \overline{\hat{u}''_i} \frac{\partial \overline{\hat{D}_{ij}}}{\partial \hat{x}_j},
\end{aligned}
\tag{7.11}
$$

where we use the conventional decomposition for the pressure and the viscous terms. Considering fully developed turbulent channel flows, equation (7.11) can be simplified, since $\widetilde{v}$, $\widetilde{w}$ and derivatives in homogeneous directions are zero. The budget equation for the SLS TKE is then

$$\hat{P}_k - \hat{\epsilon}_k + \hat{T}_k + \hat{C}_k + \hat{\mathscr{D}}_k = 0, \tag{7.12}$$

where the terms are, production $\hat{P}_k = -\widetilde{\widehat{u''v''}}\partial\widetilde{u}^{\text{vD}}/\partial\hat{y}$, dissipation per unit volume $\hat{\epsilon}_k = \overline{\widetilde{\hat{\tau}'_{ij}\partial\hat{u}'_i/\partial\hat{x}_j}}$, diffusion (viscous diffusion, turbulent transport, and pressure diffusion) $\hat{T}_k = \partial(\overline{\hat{u}'_i\hat{\tau}'_{iy}} - \widetilde{\hat{v}''\hat{k}} - \overline{\hat{p}'\hat{v}'})/\partial\hat{y}$, compressibility $\hat{C}_k = \overline{\hat{p}'\partial\hat{u}'_j/\partial\hat{x}_j} - \overline{\hat{u}''_j\partial\overline{\hat{p}}/\partial\hat{x}_j} + \overline{\hat{u}''_i\partial\overline{\hat{\tau}}_{iy}/\partial\hat{y}}$, and terms related to the mean density gradient $\hat{\mathscr{D}}_k = \widetilde{\hat{v}''\hat{k}}d_y - \overline{\hat{u}''_i\partial\hat{D}_{ij}/\partial\hat{x}_j}$. The result is an evolution equation in which the varying density has been absorbed into the van Driest velocity for the production $\hat{P}_k$, and the semi-local Reynolds number in the dissipation $\hat{\epsilon}_k$ and viscous diffusion. The TKE equation is thus essentially equivalent to its incompressible form, except the terms $\hat{C}_k$ and $\hat{\mathscr{D}}_k$ which can be considered small as we will show later. Therefore, our derivation demonstrates that the evolution of the turbulence kinetic energy is mainly governed by the semi-local Reynolds number and the gradient of the van Driest velocity. However, as we showed in Chapter 4, the van Driest velocity is not an independent quantity, since the viscous shear stress, expressed in semi-local parameters $h/Re_\tau^\star(d\overline{u}^{\text{vD}}/dy)$, is a universal function in the inner layer. This concludes that the "leading order effect" in variable property flows can be mainly characterized by the semi-local Reynolds number.

Another conclusion that can be made is that the TKE equation can be used in its incompressible form to model variable property turbulent channel flows, if the velocity in the TKE production term and the viscosity in the viscous terms are expressed by the van Driest transformed velocity and the semi-local Reynolds number, respectively. Next we will consider simple cases of fully developed turbulent channel flows with variable properties to test this statement.

7.3. Case Description and SLS TKE budgets

In order to highlight the improvement obtained using the suggested framework, we simulate cases with even higher gradients in density and viscosity as compared to the cases discussed in previous chapters. A summary of five cases used in the present chapter is given in table 7.1. The first case CP corresponds to a reference flow with constant properties at $Re_\tau = 395$. The case $\text{CRe}_\tau^\star$ corresponds to a flow for which density and viscosity are decreasing away from the wall, such that the semi-local Reynolds number $Re_\tau^\star$ is constant across the whole channel height, meaning $\sqrt{\overline{\rho}/\rho_w} = \overline{\mu}/\mu_w$. Cases GL and LL are flows with gas-like and liquid-like property variations that both have large gradients in $Re_\tau^\star$. The last case in table 7.1 (case T&L) is a fully compressible turbulent channel flow with isothermal walls, a bulk Mach number of 4, and a wall-based friction Reynolds number of 1017 (Trettel & Larsson, 2016). The largest decrease of density ($\rho_w/\rho_c \approx 8.5$) is obtained for case $\text{CRe}_\tau^\star$, while for case GL and T&L the den-

Case	ρ/ρ_w	μ/μ_w	$Re_{\tau\,w}^\star$	$Re_{\tau\,c}^\star$
CP	1	1	395	395
$CRe_\tau^\star$	$(T/T_w)^{-1}$	$(T/T_w)^{-0.5}$	395	395
GL	$(T/T_w)^{-1}$	$(T/T_w)^{0.7}$	950	137
LL	1	$(T/T_w)^{-1}$	150	943
T&L ($M_b = 4$)	$\propto p(T/T_w)^{-1}$	$(T/T_w)^{0.75}$	1017	203

Table 7.1: Investigated cases. CP - constant property case with $Re_\tau = 395$; $CRe_\tau^\star$ - variable property case with constant $Re_\tau^\star$ (= 395) across the channel; GL - case with gas-like property variations; LL - case with liquid-like property variations; T&L - fully compressible turbulent channel flow with a bulk Mach number of $Ma = 4$ from Trettel & Larsson (2016). The columns report the constitutive relations for density ρ and viscosity μ as a function of temperature T. The semi-local Reynolds numbers based on wall and channel centre values are given by $Re_{\tau\,w}^\star$ and $Re_{\tau\,c}^\star$, respectively.
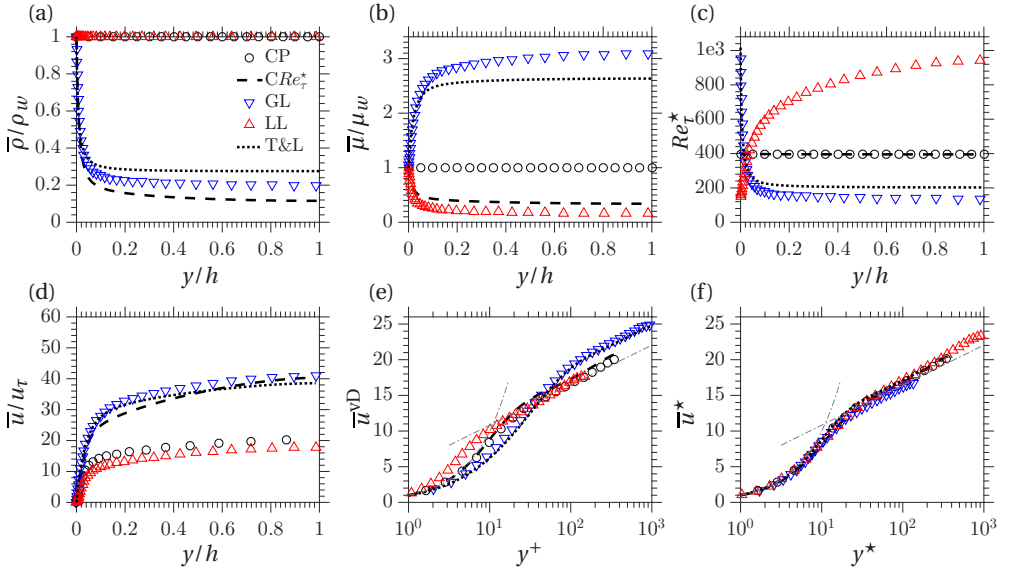

Figure 7.1: Averaged profiles for (a) density, (b) viscosity, (c) semi-local Reynolds number, (d) mean streamwise velocity, (e) van Driest transformed velocity, and (f) extended van Driest transformed velocity for DNS cases presented in table 7.1.
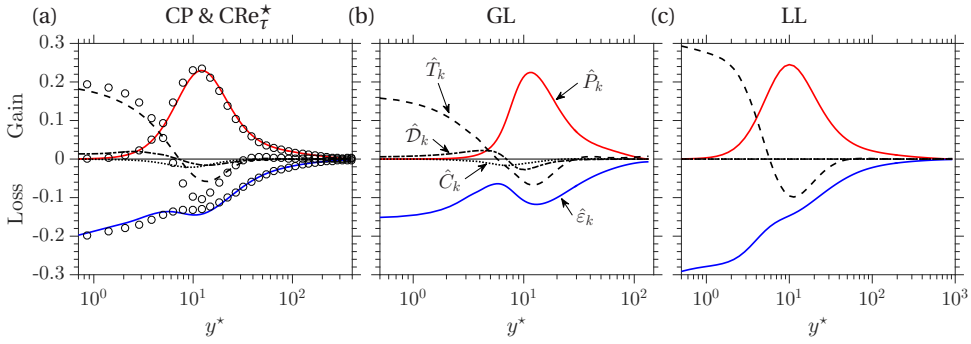
Figure 7.2: Semi-locally scaled turbulence kinetic energy budgets, equation (7.12), for cases (a) CP (symbols) and CRe$_\tau^\star$ (lines), (b) GL, and (c) LL.

sity decreases approximately by a factor 5 and 3.6, respectively (figure 7.1(a)). The profiles for viscosity are shown in figure 7.1(b). However, the most important parameter to characterize variable property flows is the semi-local Reynolds number shown in figure 7.1(c). It can be seen that the case GL and T&L show similar decreasing $Re_\tau^\star$ profiles, while $Re_\tau^\star$ for case LL increases. The case CRe$_\tau^\star$ has a constant Re$_\tau^\star$ profile by construction and collapses with the constant property case CP. The velocity profiles are shown in figure 7.1(d-f). Note, even if the velocity $\overline{u}$ for case CRe$_\tau^\star$ is considerably higher than for case CP, the van Driest velocity transformation is capable to provide a collapse with the constant property universal velocity profile. This is not the case for flows that have gradients in Re$_\tau^\star$ (GL, LL, and T&L) since the viscous scales are changing. On the other hand, the universal velocity scaling proposed by Trettel & Larsson (2016), and later independently derived by us in Chapter 4 provides a good collapse for all cases (figure 7.1(f)).

The budgets of the SLS TKE for the cases CP, CRe$_\tau^\star$, GL and LL are shown in figure 7.2, where they have been scaled by $Re_\tau^\star$. Despite the large variations in density and viscosity in case CRe$_\tau^\star$, $\hat{P}_k$ and $\hat{\epsilon}_k$ are overlapping with case CP (symbols in figure 7.2(a)), since for both cases the $Re_\tau^\star$ profiles are the same. This confirms that also turbulence production and dissipation are similar for cases with similar $Re_\tau^\star$ profiles. However, the diffusion is slightly affected by strong property gradients at the location of the production peak at $y^\star \approx 12$. In general however, $\hat{C}_k$ and $\hat{\mathcal{D}}_k$ are small for cases CRe$_\tau^\star$ and GL, and for case CP and LL they are zero, since density is constant. Based on this observation we can assume that the additional terms, $\hat{\mathcal{D}}_k$ and $\hat{C}_k$, have a minor effect on the evolution of the SLS TKE for the cases presented herein.

7.4. TURBULENCE MODELING

We first introduce the turbulence model that we will use in its conventional form. Most of the turbulence models are based on the k-ϵ model. However, the standard $k-\epsilon$ model gives unacceptable results for the turbulent shear stress in the near wall region. These models are therefore supplemented using wall damping functions f_μ in order to capture turbulence damping effects in the near wall region. In the present study, we use two turbulence models. First is a low-Reynolds number $k-\epsilon$ model of Myong & Kasagi (1990) (MK) in which f_μ is a strong function of the non-dimensional wall distance y^+. The second model is the v^2-f model of Durbin (1995) which is able to correct for turbulence damping with the help of two additional equations namely, a transport equation for the wall normal velocity fluctuation, v'^2, which is an appropriate velocity scale for turbulent transport towards the wall, and an elliptic relaxation equation that essentially models the pressure strain correlation that appears in the evolution equation for v'^2. For a fully developed turbulent flow in a channel, the equations for k, ϵ, v'^2 and f in compressible notation read,

$$-\frac{\partial}{\partial y}\left[\left(\overline{\mu}+\frac{\mu_t}{\sigma_k}\right)\frac{\partial}{\partial y}k\right] = P_k - \overline{\rho}\epsilon \tag{7.13}$$

$$-\frac{\partial}{\partial y}\left[\left(\overline{\mu}+\frac{\mu_t}{\sigma_\epsilon}\right)\frac{\partial}{\partial y}\epsilon\right] = \frac{1}{T}\left(C_{\epsilon1}f_1 P_k - C_{\epsilon2}f_2\overline{\rho}\epsilon\right). \tag{7.14}$$

The additional two equations used for v^2-f model are given as

$$L^2\frac{\partial^2 f}{\partial y^2} - f = \frac{1}{T}\left[(C_1-6)\frac{v'^2}{k}-\frac{2}{3}(C_1-1)\right]-C_2\frac{P_k}{\overline{\rho}k} \tag{7.15}$$

$$-\frac{\partial}{\partial y}\left[\left(\overline{\mu}+\frac{\mu_t}{\sigma_k}\right)\frac{\partial}{\partial y}v'^2\right] = \overline{\rho}kf-6\overline{\rho}v'^2\frac{\epsilon}{k}, \tag{7.16}$$

where the time scale T for MK and v^2-f are

$$T = \frac{k}{\epsilon} \quad \text{and} \quad T = \max\left(\frac{k}{\epsilon}, 6\sqrt{\frac{\overline{\mu}}{\overline{\rho}\epsilon}}\right), \tag{7.17}$$

respectively. In equation (7.15), $C_1 = 1.4$ and $C_2 = 0.3$ and the length scale L is given as

$$L = 0.23\max\left(\frac{k^{3/2}}{\epsilon}, 70\sqrt[4]{\frac{(\mu/\rho)^3}{\epsilon}}\right). \tag{7.18}$$

Model	C_μ	$C_{\epsilon 1}$	$C_{\epsilon 2}$	σ_k	σ_ϵ
MK	0.09	1.40	1.80	1.4	1.3
$v^2 - f$	0.22	1.40	1.90	1.0	1.3

Table 7.2: Constants in turbulence models

Model	f_μ	f_1	f_2
MK	$[1 - e^{(-\frac{y^+}{70})}](1 + \frac{3.45}{Re_t^{0.5}})$	1.0	$[1 - \frac{2}{9}e^{(-(\frac{Re_t}{6})^2)}](1 - e^{(-\frac{y^+}{5})})^2$
$v^2 - f$	$v'^2 T/(k^2/\epsilon)$	$1 + 0.045\sqrt{\frac{k}{v'^2}}$	1.0

Table 7.3: Functions in turbulence models, where $Re_t = \overline{\rho}k^2/\overline{\mu}\epsilon$

Model	Wall Boundary Condition
MK	$k_w = 0, \epsilon_w = \frac{\mu_w}{\rho_w}\frac{\partial^2}{\partial y^2}k$
$v^2 - f$	$k_w = 0, \epsilon_w = \frac{\mu_w}{\rho_w}\frac{\partial^2}{\partial y^2}k, v'^2_w = 0, f_w = 0$

Table 7.4: Wall boundary conditions

The turbulent viscosity is then calculated as,

$$\mu_t = \overline{\rho}C_\mu f_\mu \frac{k^2}{\epsilon}. \tag{7.19}$$

and using the Boussinesq approximation

$$P_k = \mu_t \left(\frac{\partial \tilde{u}}{\partial y}\right)^2. \tag{7.20}$$

In Equation (7.13)–(7.19) $C_\mu, C_{\epsilon_1}, C_{\epsilon_2}, \sigma_k, \sigma_\epsilon$ are empirical constants, while f_μ, f_1 and f_2 are functions used to incorporate wall effects. The values of all these parameters depend on the turbulence model and are summarized along with the wall boundary condition in table 7.2–7.4. The turbulent viscosity could then be used to obtain the turbulent shear stress in the averaged streamwise momentum equation given by

$$\frac{\partial}{\partial y}\left[(\overline{\mu} + \mu_t)\frac{\partial}{\partial y}\overline{u}\right] = \frac{\partial \overline{p}}{\partial x}, \tag{7.21}$$

in order to obtain the mean velocity. Since the aim of this study is to investigate the effect of variable properties on velocity statistics, we do not consider the energy equation. Instead we directly prescribe the averaged density and viscosity profiles from DNS. This approach allows to perform an isolated study on

how variable properties affect turbulence without including errors that originate from modeling the wall-normal turbulent heat flux in the energy equation, commonly approximated by the ratio of the eddy viscosity and the turbulent Prandtl number. Equations (7.13)-(7.21) can thus be used to model the turbulent statistics in variable property channel flows - if the density and viscosity profiles are provided as an input from the DNS.

On the other hand, instead of using the conventional compressible formulation of the turbulence model, we can solve the turbulence model in its semi-locally scaled form. Following a pragmatic approach, we assume that analogous to the turbulence kinetic energy equation (7.11), the supporting model equations can be expressed in their semi-local formulation. In addition we make all the common modeling assumptions, such as $\mu' \ll \overline{\mu}$, that the molecular and turbulent diffusion can be approximated by the gradient diffusion hypothesis, and the additional assumption that the influence of $\hat{C}_k$ and $\hat{\mathscr{D}}_k$ on turbulence statistics is small. Then, the only changes that need to be made to solve a turbulence model in semi-locally scaled form, are to

- set $\overline{\rho} = 1$,

- replace $\overline{\mu}$ by $1/Re_\tau^\star$,

- replace $\partial \tilde{u}$ in P_k by $\partial \tilde{u}^{\mathrm{vD}}$,

- and, if a model makes use of y^+, replace it by $y^\star$.

The corresponding momentum equation can either be solved in its conventional (7.21) or in its semi-locally scaled form, i.e.,

$$\frac{\partial}{\partial \hat{y}}\left[\left(\frac{1}{Re_\tau^\star} + \hat{\mu}_t\right)\frac{\partial}{\partial \hat{y}}\overline{u}^{\mathrm{vD}}\right] = -1. \tag{7.22}$$

In the latter, it can be seen that indeed, the only parameter that governs the turbulence model and the momentum equation is $Re_\tau^\star$. If the momentum equation is solved in its conventional form, the semi-locally scaled eddy viscosity $\hat{\mu}_t$, which is provided by the turbulence model, has to be transformed to the conventionally scaled form by $\mu_t = \overline{\rho} h u_\tau^\star \hat{\mu}_t$. This relation can be obtained using the same normalization as introduced in equation (7.2). Nevertheless, it can be shown that both formulations of the momentum equation lead to equivalent results.

The results for MK model using both formulations, the conventional compressible form (red dashed dotted lines) and the semi-locally scaled form (blue solid line) are shown and compared with DNS data (circles) in figure 7.3. Considerable improvement is obtained using the semi-local based MK model. It should

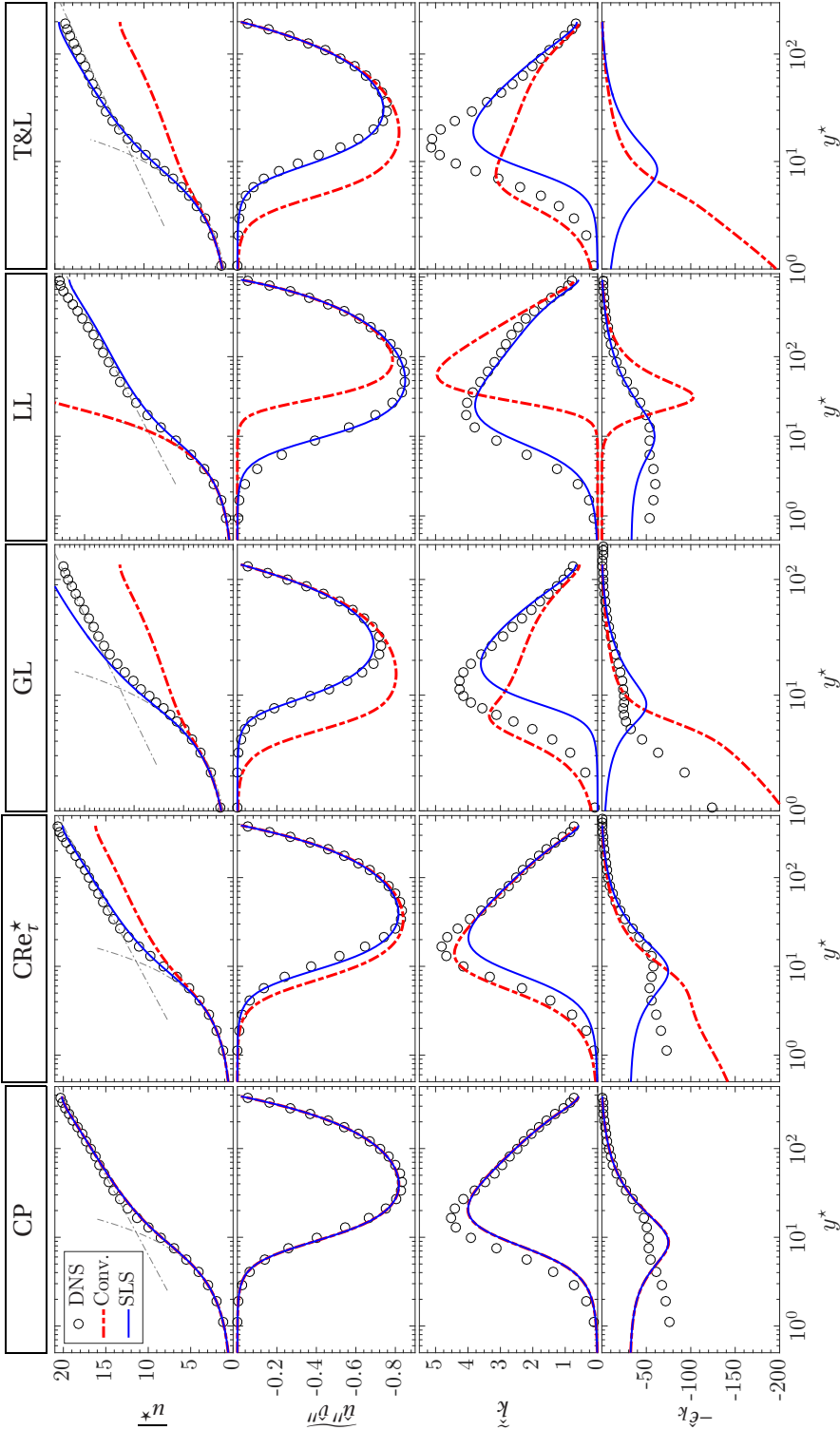Figure 7.3: DNS results (symbols) compared to conventional (red dashed-line) and semi-locally scaled (blue solid line) MK model for the cases (columns) introduced in table 7.1. The rows correspond to the extended van Driest transformed velocity $\overline{u}^\star$, semi-locally scaled profiles for turbulent shear stress $\widetilde{u''v''}$, turbulence kinetic energy $\tilde{k}$ and dissipation $\hat{\epsilon}_k$.

Figure 7.4: DNS results (symbols) compared to conventional (red dashed-line) and semi-locally scaled (blue solid line) $\overline{v^2} - f$ model for the cases (columns) introduced in table 7.1. The rows correspond to the extended van Driest transformed velocity $\overline{u^\star}$, semi-locally scaled profiles for turbulent shear stress $\widehat{u''\hat{v}''}$, turbulence kinetic energy $\widetilde{k}$ and dissipation $\hat{\epsilon}_k$.
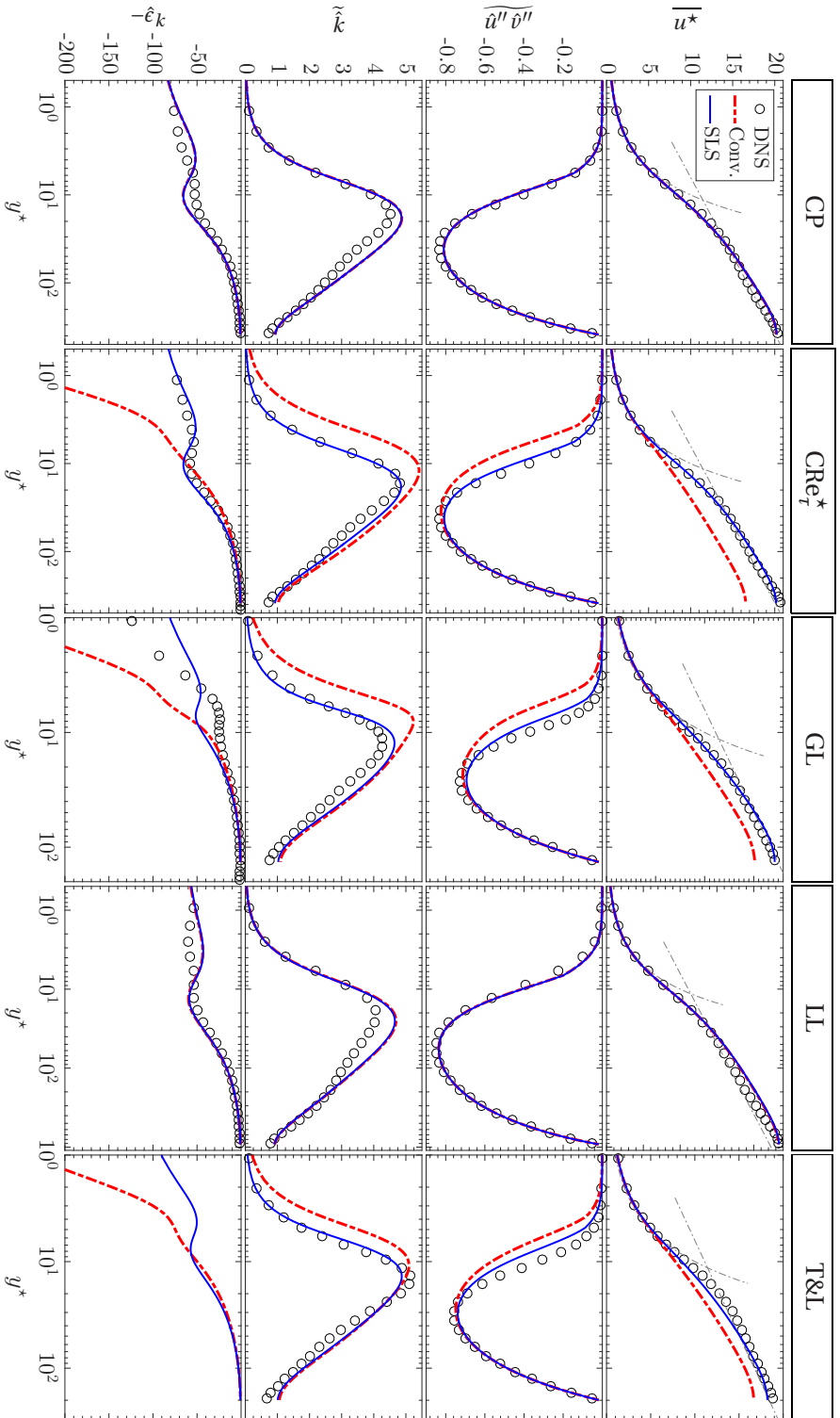
be noted that the MK model is known to under predict the k and ϵ in order to predict the Reynolds shear stress correctly. This can be appreciated by observing the constant property case CP for which both k and ϵ are below the DNS data, while the Reynolds shear stress and corresponding velocity profile match the DNS data closely. As stated above, MK model uses a damping function which is a strong function of non-dimensional wall distance y^+. However, only changing the non-dimensional coordinate from y^+ to $y^\star$ does not necessarily improve the model performance. This can be seen using case $CRe_\tau^\star$ for which $y^\star = y^+$, yet significant differences can be seen between conventional model and DNS data. Other cases also show significant improvement using the proposed improvements. It can also be seen that case GL shows similar behavior as the compressible case from Trettel & Larsson (2016). The comparison of the results for the $v^2 - f$ model using both conventional and semi-local form is shown in figure 7.4. Again significant improvement is obtained for cases with density gradients (i.e all cases except LL). The semi-local form of the $v^2 - f$ model in addition also provides a good estimate of the turbulence kinetic energy.

7.5. SUMMARY

We derived an alternative form of the turbulence kinetic energy for wall bounded flows with strong near-wall variations in density and viscosity. This alternative form clearly indicates that the "leading order effect" of variable properties on turbulence can be characterized by the semi-local Reynolds number, and that higher-order effects, such as solenoidal dissipation, pressure -work, -diffusion and -dilatation indeed are small and play a minor role in modulating turbulence for the cases investigated herein. We showed that if a turbulence model is solved in semi-local form, excellent agreements with DNS are obtained for low-Mach and supersonic channel flows.

8
CONCLUSION

The aim of this work was to characterize wall-bounded turbulence for fluids that have large near-wall gradients in thermophysical properties. The focus was on the variable inertia effects at the low-Mach number limit without the influence of buoyancy. A scaling transformation applied to the Navier–Stokes equations, that is based on local mean values of density $\overline{\rho}$, viscosity $\overline{\mu}$ and semi-local friction velocity $u_\tau^\star = \sqrt{\tau_w/\overline{\rho}}$ (τ_w is the wall shear stress), suggests that the leading order effect of varying properties on turbulence can effectively be characterized by the semi-local Reynolds number. The semi-local Reynolds number is defined as $Re_\tau^\star \equiv \sqrt{(\overline{\rho}/\rho_w)}/(\overline{\mu}/\mu_w)Re_\tau$ (Re_τ is the friction Reynolds number based on wall values). The derived equations also provide a theoretical framework for the semi-local scaling that has been proposed based on heuristic arguments by Huang *et al.* (1995). In order to test the proposed framework and to further analyse the scaling of turbulence statistics, direct numerical simulations of a fully developed internally heated channel flow were performed with different relations for density ρ, viscosity μ and thermal conductivity λ as a function of temperature. Based on the scaling transformation and the performed DNS, the following main conclusions can be made:

- The semi-local Reynolds number $Re_\tau^\star$ accounts for changes in viscous length scales due to property variations.

- Turbulence statistics, such as the van Driest transformed velocity $\overline{u}^{\mathrm{vD}}$, the Reynolds stresses and their anisotropies, the Kolmogorov scales, mixing length, and turbulent vorticity fluctuations are indeed strongly governed by $Re_\tau^\star$ profiles, and their dependence on individual density and viscosity profiles is minor.

- Similar to turbulence statistics, the characteristics of turbulent structures, such as streamwise velocity streaks and quasi-streamwise vortices, are also strongly governed by the wall-normal distribution of $Re_\tau^\star$.

- While $\overline{u}^{\mathrm{vD}}$ depends highly on the $Re_\tau^\star$ distribution, the viscous stress given as $(h/Re_\tau^\star)\,d\overline{u}^{\mathrm{vD}}/dy$, shows a good universal collapse in the inner layer for all cases when plotted as a function of the semi-local wall coordinate $y^\star$. This universal collapse provides a basis to derive an extension of the van Driest transformation $\overline{u}^\star = \int_0^{\overline{u}^{\mathrm{vD}}} \left(1 + \left(y/Re_\tau^\star\right) dRe_\tau^\star/dy\right) d\overline{u}^{\mathrm{vD}}$, that accounts for gradients in $Re_\tau^\star$ and is therefore able to collapse velocity profiles for all cases as a function of $y^\star$.

- Other turbulence statistics, such as mixing length, turbulence anisotropy, and turbulent vorticity fluctuations, do not show a universal scaling very close to the wall for flows with near-wall gradients in $Re_\tau^\star$. This is attributed

to strong non-local effects and structural changes in turbulence that affect lifting and tilting of quasi-streamwise vortices. These structural changes are responsible for the observed modulations of the Reynolds stress generation mechanism and the inter-component energy transfer in flows with strong near-wall $Re_\tau^\star$ gradients. The influence of these turbulence modulations on the extended van Driest transformation is limited in the viscous dominated region very close to the wall ($y^\star < 10$), and hence does not alter the universality of the extended van Driest transformation.

- $\overline{u}^{\text{vD}}$ of a variable density flow is the analog to the mean velocity of a constant density flow. In other words, turbulence modulations related to changes in mean velocity gradient for constant density flows can be translated to variable density flows by assessing gradient of $\overline{u}^{\text{vD}}$.

- For parameterizing the scaling characteristics of scalar field, the distribution of the local Prandtl number $Pr^\star \equiv Pr_w(\overline{\mu}/\mu_w)/(\overline{\lambda}/\lambda_w)$ (Pr_w is the Prandtl number based on wall values) has to be included, in addition to the $Re_\tau^\star$ profile. Cases with quasi-similar distributions of both $Re_\tau^\star$ and $Pr^\star$, result in a quasi-similar van Driest transformed temperature $\overline{\theta}^{\text{vD}}$ and higher order temperature statistics, irrespective of individual density, viscosity or thermal conductivity profiles.

- Similar to the extended van Driest transformed velocity, an analogous extended van Driest transformed mean temperature profile has been derived $\overline{\theta}^\star = \int_0^{\overline{\theta}^{\text{vD}}} \left(1 + \left(y/Re_\tau^\star\right) dRe_\tau^\star/dy\right) d\overline{\theta}^{\text{vD}}$, which results in a good collapse of the temperature profiles for cases with similar $Pr^\star$ distributions, irrespective of the $Re_\tau^\star$ distribution. This is a result of the strong analogy between momentum and scalar transfer, which can be seen using the turbulent Prandtl number that is close to unity in the inner layer.

- Finally, an alternative form of the turbulent kinetic energy equation, which is consistent with the semi-local framework, is derived using the scaling transformation described earlier. The alternative formulation suggests that the leading order effect of property variations can be incorporated in an incompressible $k - \epsilon$ turbulence model, if the velocity in the turbulence kinetic energy production term and the viscosity in the viscous terms of diffusion and dissipation are expressed by the van Driest transformed velocity and the semi-local Reynolds number, respectively. It has been shown that if a turbulence model is solved in its semi-locally scaled form, the obtained results from the model agree well with results from DNS, while the conventional modeling approach fails.

The conclusions reported in the present work are general in nature and hence are applicable to any Newtonian fluid with heated or cooled wall as long as the basic assumptions made in the work hold. The contemporary definition of Morkovin's hypothesis is that, many of the differences seen between supersonic and constant property boundary layers can be explained by simply accounting for the fluid property variations that are caused by the temperature variation (Smits & Dussauge, 2006). The present work goes one step further and suggests that, the *differences* seen between variable and constant property boundary layers can be explained by the non-dimensional parameters, $Re_\tau^\star$ and $Pr^\star$, which accommodate the combined influence of property variations. The word *differences* is emphasized above, in order to highlight the structural changes that occur due to $Re_\tau^\star$ variations.

Some of the additional questions that should be addressed in future studies include:

- Investigating the applicability of the semi-local framework for more complex configurations, such as

    - developing thermal boundary layer,

    - strongly heated/cooled fluids close to their vapor-liquid critical point, and

    - heated or cooled boundary layers at supersonic speeds.

- Investigating why the near-wall streaks strengthen or weaken for cases with gradients in $Re_\tau^\star$, using a transient growth analysis as proposed by del Álamo & Jiménez (2006) and Pujals *et al.* (2009) for constant property turbulent flows.

- Investigating the dynamics of near-wall cycle for cases with strong property gradients by repeating the numerical experiments carried out in Jiménez & Pinelli (1999) for constant property turbulent flows.

- Investigating the effectiveness of the semi-local wall coordinate in cases where buoyancy aids or opposes the mean flow.

- In the present work the strong property gradients occur in the shear dominated region. Cases where property gradients occur in regions of smaller shear might introduce additional physical mechanisms that could potentially invalidate assumptions made in this work. This should be investigated in more detail.

- Also cases for which the profile of $Re_\tau^\star$ has a local maxima or minima should be investigated with respect to the validity of the derived framework and velocity scaling.

A

DERIVATION OF SEMI-LOCALLY SCALED MOMENTUM EQUATION FOR FLUCTUATING VELOCITY COMPONENTS

The momentum equations for the fluctuating components can be written as,

$$t_\tau^\star \frac{\partial \hat{u}_i''}{\partial t} + \frac{\partial \hat{u}_i'' \hat{u}_j''}{\partial \hat{x}_j} + \frac{\partial \tilde{\hat{u}}_i \hat{u}_j''}{\partial \hat{x}_j} + \frac{\partial \hat{u}_i'' \tilde{\hat{u}}_j}{\partial \hat{x}_j} \approx$$
$$-\frac{\partial \hat{p}'}{\partial \hat{x}_i} + \frac{\partial \widetilde{\hat{u}_i'' \hat{u}_j''}}{\partial \hat{x}_j} + \frac{\partial}{\partial \hat{x}_j}\left(\hat{\tau}_{ij}' - \hat{D}_{ij}\right), \qquad \text{(A.1)}$$

where $\hat{\tau}_{ij}' = \frac{1}{Re_\tau^\star}\left[\left(\frac{\partial \hat{u}_i'}{\partial \hat{x}_j} + \frac{\partial \hat{u}_j'}{\partial \hat{x}_i}\right) - \frac{2}{3}\frac{\partial \hat{u}_k'}{\partial \hat{x}_k}\delta_{ij}\right]$
and $\hat{D}_{ij} = \frac{1}{Re_\tau^\star}\left(\frac{\rho_w}{\overline{\rho}}\right)\left[\frac{\hat{u}_i'}{2}\frac{\partial}{\partial \hat{x}_j}\left(\frac{\overline{\rho}}{\rho_w}\right) + \frac{\hat{u}_j'}{2}\frac{\partial}{\partial \hat{x}_i}\left(\frac{\overline{\rho}}{\rho_w}\right) - \delta_{ij}\frac{\hat{v}'}{3}\frac{\partial}{\partial \hat{y}}\left(\frac{\overline{\rho}}{\rho_w}\right)\right]$. This equation can be
further simplified by applying the product rule in the third and the fourth term

$$t_\tau^\star \frac{\partial \hat{u}_i''}{\partial t} + \frac{\partial \hat{u}_i'' \hat{u}_j''}{\partial \hat{x}_j} + \tilde{\hat{u}}_i \frac{\partial \hat{u}_j''}{\partial \hat{x}_j} + \hat{u}_j'' \frac{\partial \tilde{\hat{u}}_i}{\partial \hat{x}_j} + \hat{u}_i'' \frac{\partial \tilde{\hat{u}}_j}{\partial \hat{x}_j} + \tilde{\hat{u}}_j \frac{\partial \hat{u}_i''}{\partial \hat{x}_j} \approx$$
$$-\frac{\partial \hat{p}'}{\partial \hat{x}_i} + \frac{\partial \widetilde{\hat{u}_i'' \hat{u}_j''}}{\partial \hat{x}_j} + \frac{\partial}{\partial \hat{x}_j}\left(\hat{\tau}_{ij}' - \hat{D}_{ij}\right), \qquad \text{(A.2)}$$

and using the continuity equations (3.15) and (3.21) the equation can be written
for a fully periodic channel flow as

$$t_\tau^\star \frac{\partial \hat{u}_i''}{\partial t} + \frac{\partial \hat{u}_i'' \hat{u}_j''}{\partial \hat{x}_j} - \tilde{\hat{u}}\frac{\hat{v}''}{2}\left(\frac{\rho_w}{\overline{\rho}}\right)\frac{\partial}{\partial \hat{y}}\left(\frac{\overline{\rho}}{\rho_w}\right)\delta_{i1} + \hat{v}''\frac{\partial \tilde{\hat{u}}}{\partial \hat{y}}\delta_{i1} + \tilde{\hat{u}}_j\frac{\partial \hat{u}_i''}{\partial \hat{x}_j} \approx$$
$$-\frac{\partial \hat{p}'}{\partial \hat{x}_i} + \frac{\partial \widetilde{\hat{u}_i'' \hat{u}_j''}}{\partial \hat{x}_j} + \frac{\partial}{\partial \hat{x}_j}\left(\hat{\tau}_{ij}' - \hat{D}_{ij}\right). \quad \text{(A.3)}$$

Replacing $\tilde{\hat{u}}$ with $\sqrt{\frac{\overline{\rho}}{\rho_w}}\frac{\tilde{u}}{u_\tau}$ using equation (3.13), and applying the product rule we
obtain

$$t_\tau^\star \frac{\partial \hat{u}_i''}{\partial t} + \frac{\partial \hat{u}_i'' \hat{u}_j''}{\partial \hat{x}_j} - \tilde{\hat{u}}\frac{\hat{v}''}{2}\left(\frac{\rho_w}{\overline{\rho}}\right)\frac{\partial}{\partial \hat{y}}\left(\frac{\overline{\rho}}{\rho_w}\right)\delta_{i1} + \hat{v}''\delta_{i1}\left(\sqrt{\frac{\overline{\rho}}{\rho_w}}\frac{\partial}{\partial \hat{y}}\left(\frac{\tilde{u}}{u_\tau}\right) + \frac{\tilde{u}}{u_\tau}\frac{\partial}{\partial \hat{y}}\left(\sqrt{\frac{\overline{\rho}}{\rho_w}}\right)\right)$$
$$+ \tilde{\hat{u}}_j\frac{\partial \hat{u}_i''}{\partial \hat{x}_j} \approx -\frac{\partial \hat{p}'}{\partial \hat{x}_i} + \frac{\partial \widetilde{\hat{u}_i'' \hat{u}_j''}}{\partial \hat{x}_j} + \frac{\partial}{\partial \hat{x}_j}\left(\hat{\tau}_{ij}' - \hat{D}_{ij}\right). \quad \text{(A.4)}$$

$\frac{\partial}{\partial \hat{y}}\left(\sqrt{\frac{\overline{\rho}}{\rho_w}}\right)$ can be expressed as $\frac{1}{2}\sqrt{\frac{\rho_w}{\overline{\rho}}}\frac{\partial}{\partial \hat{y}}\left(\frac{\overline{\rho}}{\rho_w}\right)$, and using equation (3.18) and (3.13)
in the fourth and the fifth term we get after algebraic manipulation the final form

of the momentum equations

$$t_\tau^\star \frac{\partial \hat{u}_i''}{\partial t} + \frac{\partial \hat{u}_i'' \hat{u}_j''}{\partial \hat{x}_j} + \hat{v}'' \frac{\partial \tilde{u}^{vd}}{\partial \hat{y}} \delta_{i1} + \tilde{\tilde{u}}_j \frac{\partial \hat{u}_i''}{\partial \hat{x}_j} \approx$$

$$-\frac{\partial \hat{p}'}{\partial \hat{x}_i} + \frac{\partial \widetilde{\hat{u}_i'' \hat{u}_j''}}{\partial \hat{x}_j} + \frac{\partial}{\partial \hat{x}_j} \left(\hat{\tau}_{ij}' - \hat{D}_{ij} \right). \tag{A.5}$$
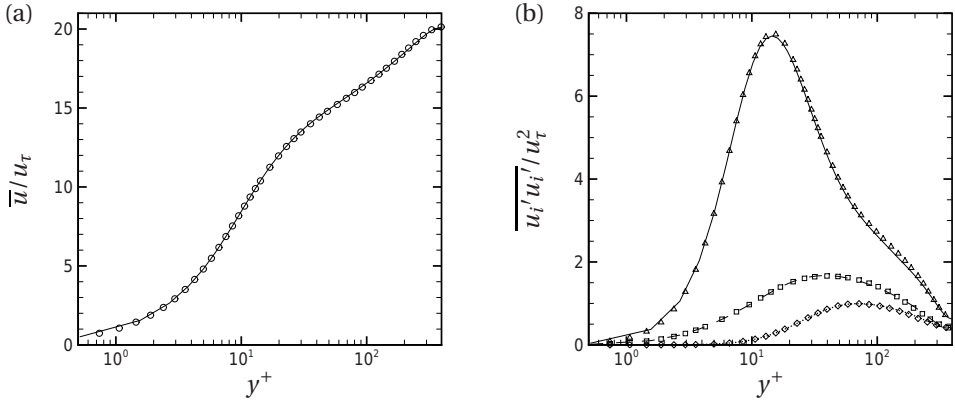
B

VALIDATION

Figure B.1: (a) Mean velocity profile and (b) normal Reynolds stresses. Lines, case CP395; symbols, data from Moser *et al.* (1999). In (b) (——, $\triangle$) $\overline{u'u'}$; (··········, $\diamond$) $\overline{v'v'}$; (– – – , $\square$) $\overline{w'w'}$.

The DNS code is validated with data from Moser *et al.* (1999), Kim & Moin (1989) and Nicoud (2000). Figure B.1 compares our result with data from Moser *et al.* (1999) for mean velocity and normal Reynolds stresses. Figure B.2 shows similar comparison for budgets of turbulence kinetic energy and streamwise Reynolds stress. As can be seen all statistics show excellent agreement with Moser *et al.* (1999). The scalar transport equation for the temperature has been validated with data extracted from Kim & Moin (1989) for passive scalar simulations with $Re_\tau = 180$ and $Pr_w = 0.7$. The comparison of mean temperature and root mean square temperature fluctuation between present code and Kim & Moin (1989) is given in figure B.3, again showing excellent agreement. The variable property influences are validated with data extracted from Nicoud (2000), who used a low-Mach number solver to perform DNS of a turbulent channel flow between two isothermal walls with temperatures T_1 and T_2. The density, viscosity and thermal conductivity are a function of temperature. Two cases corresponding to $T_2/T_1 = 2$ and $T_2/T_1 = 4$ are used for validation. The comparison of velocity profile on both hot and cold walls for two cases is shown in figure B.4. A reasonable collapse is obtained between present code and data from Nicoud (2000).
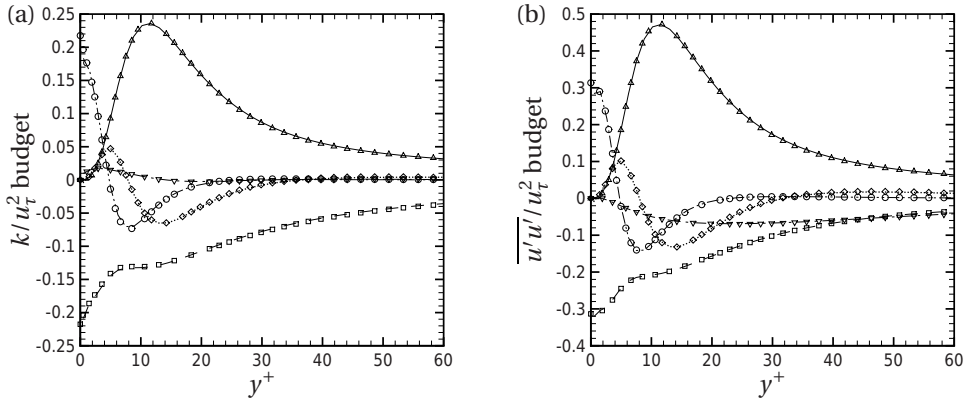
Figure B.2: (a) Turbulence kinetic energy $k = \overline{u_k' u_k'}/2$ budget and (b) streamwise Reynolds stress $\overline{u'u'}$ budget. Lines, case CP395; symbols, data from Moser *et al.* (1999). (———, $\triangle$) production; (– – – , $\square$) dissipation; (·········, $\diamond$) turbulent diffusion; (—··—,$\circ$) viscous diffusion; (—·—,∇) turbulent pressure diffusion in (a) and pressure strain in (b).
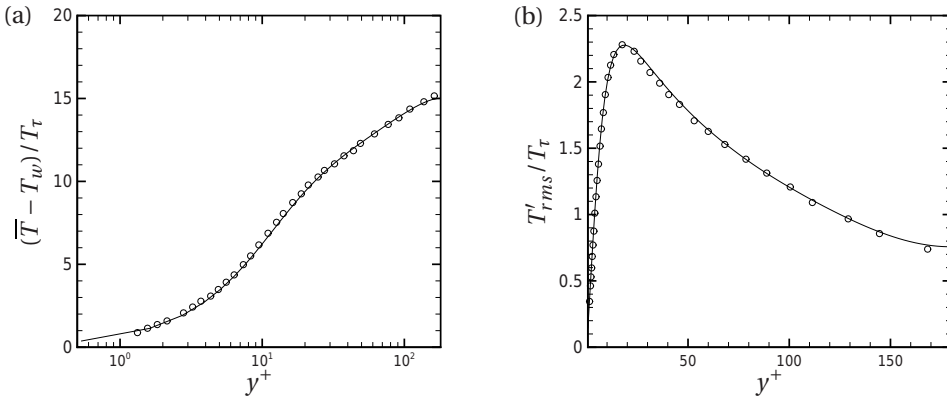

Figure B.3: (a) Mean temperature profile $(\overline{T} - T_w)/T_\tau$ and (b) root mean square of temperature fluctuations T'_{rms}/T_τ, T_τ is friction temperature defined as $T_\tau = q_w/(\rho c_p u_\tau)$. Lines, present code; symbols, data obtained from Kim & Moin (1989).
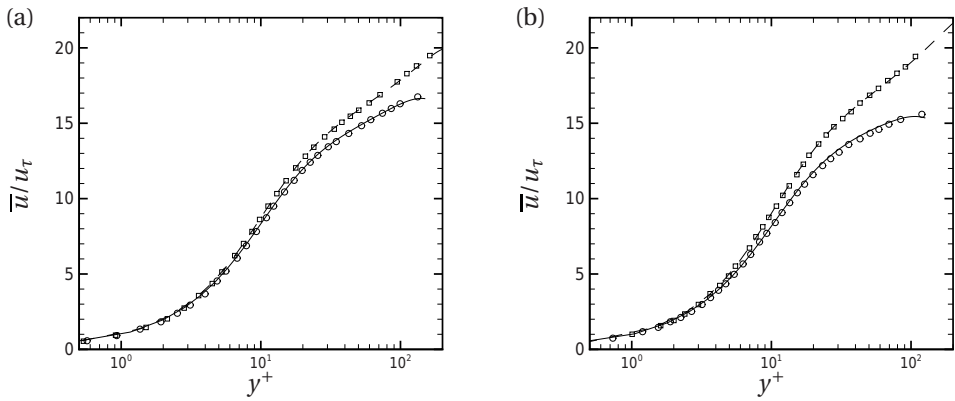
Figure B.4: Mean velocity profile for case with (a) $T_2/T_1 = 2$ and (b) $T_2/T_1 = 4$. Lines, present code; symbols, data obtained from Nicoud (2000). (———, ∘) hot side; (– – – , □) cold side.

REFERENCES

ABE, H., KAWAMURA, H. & CHOI, H. 2004 Very large-scale structures and their effects on the wall shear-stress fluctuations in a turbulent channel flow up to $Re_\tau = 640$. *J. Fluids Eng.* **126** (5), 835–843.

DEL ÁLAMO, J. & JIMÉNEZ, J. 2006 Linear energy amplification in turbulent channels. *J. Fluid Mech.* **559**, 205–213.

ANTONIA, R. & KIM, J. 1994 Low-Reynolds-number effects on near-wall turbulence. *J. Fluid Mech.* **276**, 61–80.

BERNARDINI, M. & PIROZZOLI, S. 2011 Wall pressure fluctuations beneath supersonic turbulent boundary layers. *Phys. Fluids* **23** (8), 085102.

BERNARDINI, M., PIROZZOLI, S. & ORLANDI, P. 2014 Velocity statistics in turbulent channel flow up to $Re\tau = 4000$. *J. Fluid Mech.* **742**, 171–191.

BOERSMA, B. J. 2011 A 6th order staggered compact finite difference method for the incompressible Navier–Stokes and scalar transport equations. *J. Comput. Phys.* **230** (12), 4940–4954.

BRADSHAW, P. 1977 Compressible turbulent shear layers. *Annu. Rev. Fluid Mech.* **9** (1), 33–52.

BUSHNELL, D. M. & MCGINLEY, C. B. 1989 Turbulence control in wall flows. *Annu. Rev. Fluid Mech.* **21** (1), 1–20.

CARLSON, J. A., JAFFE, A. & WILES, A. 2006 *The millennium prize problems*. American Mathematical Soc.

CHEN, H., ADRIAN, R. J., ZHONG, Q. & WANG, X. 2014 Analytic solutions for three dimensional swirling strength in compressible and incompressible flows. *Phys. Fluids* **26** (8), 081701.

CHEN, H., GOSWAMI, D. Y. & STEFANAKOS, E. K. 2010 A review of thermodynamic cycles and working fluids for the conversion of low-grade heat. *Renew. Sustainable Energy Reviews* **14** (9), 3059–3067.

117

CHERNYSHENKO, S. & BAIG, M. 2005 The mechanism of streak formation in near-wall turbulence. *J. Fluid Mech.* **544** (1), 99–131.

COLEMAN, G. N., KIM, J. & MOSER, R. D. 1995 A numerical study of turbulent supersonic isothermal-wall channel flow. *J. Fluid Mech.* **305**, 159–183.

DAS, S. K., CHOI, S. U. & PATEL, H. E. 2006 Heat transfer in nanofluids—a review. *Heat Transfer Eng.* **27** (10), 3–19.

DOSTAL, V., DRISCOLL, M. J. & HEJZLAR, P. 2004 A supercritical carbon dioxide cycle for next generation nuclear reactors. *Massachusetts Institute of Technology., Paper No. MIT-ANP-TR-100* .

DUAN, L., BEEKMAN, I. & MARTIN, M. P. 2010 Direct numerical simulation of hypersonic turbulent boundary layers. Part 2. Effect of wall temperature. *J. Fluid Mech.* **655**, 419–445.

DUAN, L., BEEKMAN, I. & MARTIN, M. P. 2011 Direct numerical simulation of hypersonic turbulent boundary layers. Part 3. Effect of Mach number. *J. Fluid Mech.* **672**, 245–267.

DURBIN, P. A. 1995 Separated flow computations with the k-epsilon-v-squared model. *AIAA J.* **33** (4), 659–664.

ELSINGA, G., ADRIAN, R., VAN OUDHEUSDEN, B. & SCARANO, F. 2010 Three-dimensional vortex organization in a high-Reynolds-number supersonic turbulent boundary layer. *J. Fluid Mech.* **644**, 35–60.

EYINK, G. L. 2008 Turbulent flow in pipes and channels as cross-stream "inverse cascades" of vorticity. *Phys. Fluids* **20** (12), 125101.

FOYSI, H., SARKAR, S. & FRIEDRICH, R. 2004 Compressibility effects and turbulence scalings in supersonic channel flow. *J. Fluid Mech.* **509**, 207–216.

GAO, Q., ORTIZ-DUENAS, C. & LONGMIRE, E. 2011 Analysis of vortex populations in turbulent wall-bounded flows. *J. Fluid Mech.* **678**, 87–123.

GEORGE, W. K. 2013 Lectures in turbulence for the 21st century .

GINZBURG, V. L. 2013 *The Physics of a Lifetime: Reflections on the Problems and Personalities of 20th Century Physics*. Springer Science & Business Media.

GUARINI, S. E., MOSER, R. D., SHARIFF, K. & WRAY, A. 2000 Direct numerical simulation of a supersonic turbulent boundary layer at Mach 2.5. *J. Fluid Mech.* **414**, 1–33.

GAD-EL HAK, M. 1990 Control of low-speed airfoil aerodynamics. *AIAA J.* **28** (9), 1537–1552.

GAD-EL HAK, M. & BANDYOPADHYAY, P. R. 1994 Reynolds number effects in wall-bounded turbulent flows. *Applied Mechanics Reviews* **47** (8), 307–365.

HAMILTON, J. M., KIM, J. & WALEFFE, F. 1995 Regeneration mechanisms of near-wall turbulence structures. *J. Fluid Mech.* **287**, 317–348.

HE, S., KIM, W. & BAE, J. 2008 Assessment of performance of turbulence models in predicting supercritical pressure heat transfer in a vertical tube. *Int. J. Heat Mass Transfer* **51** (19), 4659–4675.

HOYAS, S. & JIMÉNEZ, J. 2006 Scaling of the velocity fluctuations in turbulent channels up to $Re_\tau = 2003$. *Phys. Fluids* **18** (1), 011702.

HOYAS, S. & JIMÉNEZ, J. 2008 Reynolds number effects on the reynolds-stress budgets in turbulent channels. *Phys. Fluids* **20** (10), 101511.

HUANG, P. & COLEMAN, G. N. 1994 Van Driest transformation and compressible wall-bounded flows. *AIAA J.* **32** (10), 2110–2113.

HUANG, P. G., COLEMAN, G. N. & BRADSHAW, P. 1995 Compressible turbulent channel flows: DNS results and modelling. *J. Fluid Mech.* **305**, 185–218.

HUTCHINS, N. & MARUSIC, I. 2007 Large-scale influences in near-wall turbulence. *Philo. Trans. Roy. Soc. Lond.* **365** (1852), 647–664.

IVERSON, B. D., CONBOY, T. M., PASCH, J. J. & KRUIZENGA, A. M. 2013 Supercritical co2 brayton cycles for solar-thermal energy. *Applied Energy* **111**, 957–970.

JEONG, J., HUSSAIN, F., SCHOPPA, W. & KIM, J. 1997 Coherent structures near the wall in a turbulent channel flow. *J. Fluid Mech.* **332**, 185–214.

JIMÉNEZ, J. 2013 Near-wall turbulence. *Phys. Fluids* **25** (10), 101302.

JIMÉNEZ, J., HOYAS, S., SIMENS, M. P. & MIZUNO, Y. 2010 Turbulent boundary layers and channels at moderate Reynolds numbers. *J. Fluid Mech.* **657**, 335–360.

JIMÉNEZ, J. & MOSER, R. D. 2007 What are we learning from simulating wall turbulence? *Philos. Trans. R. Soc., A* **365** (1852), 715–732.

JIMÉNEZ, J. & PINELLI, A. 1999 The autonomous cycle of near-wall turbulence. *J. Fluid Mech.* **389**, 335–359.

JOHANSSON, A. V., ALFREDSSON, P. H. & KIM, J. 1991 Evolution and dynamics of shear-layer structures in near-wall turbulence. *J. Fluid Mech.* **224**, 579–599.

KADER, B. 1981 Temperature and concentration profiles in fully turbulent boundary layers. *Intl J. Heat Mass Transfer* **24** (9), 1541–1544.

KAWAMURA, H., ABE, H. & MATSUO, Y. 1999 Dns of turbulent heat transfer in channel flow with respect to reynolds and prandtl number effects. *Intl J. Heat Fluid Flow* **20** (3), 196–207.

KAWAMURA, H., OHSAKA, K., ABE, H. & YAMAMOTO, K. 1998 Dns of turbulent heat transfer in channel flow with low to medium-high prandtl number fluid. *Intl J. Heat Fluid Flow* **19** (5), 482–491.

KIM, J. & HUSSAIN, F. 1993 Propagation velocity of perturbations in turbulent channel flow. *Phys. Fluids A: Fluid Dynamics (1989-1993)* **5** (3), 695–706.

KIM, J. & LIM, J. 2000 A linear process in wall-bounded turbulent shear flows. *Phys. Fluids* **12** (8), 1885–1888.

KIM, J. & MOIN, P. 1989 Transport of passive scalars in a turbulent channel flow. In *Turbulent Shear Flows 6*, pp. 85–96. Springer.

KLEWICKI, J., METZGER, M., KELNER, E. & THURLOW, E. 1995 Viscous sublayer flow visualizations at $R_\theta = 1\,500\,000$. *Phys. Fluids* **7** (4), 857–863.

KLINE, S., REYNOLDS, W., SCHRAUB, F. & RUNSTADLER, P. 1967 The structure of turbulent boundary layers. *J. Fluid Mech.* **30** (04), 741–773.

KOLMOGOROV, A. N. 1941 The local structure of turbulence in incompressible viscous fluid for very large reynolds numbers. In *Dokl. Akad. Nauk SSSR*, , vol. 30, pp. 301–305. JSTOR.

LAGHA, M., KIM, J., ELDREDGE, J. & ZHONG, X. 2011*a* A numerical study of compressible turbulent boundary layers. *Phys. Fluids* **23** (1), 015106.

LAGHA, M., KIM, J., ELDREDGE, J. D. & ZHONG, X. 2011*b* Near-wall dynamics of compressible boundary layers. *Phys. Fluids* **23** (6), 065109.

LECHNER, R., SESTERHENN, J. & FRIEDRICH, R. 2001 Turbulent supersonic channel flow. *J. Turbulence* **2**, 1–25.

LEE, J., JUNG, S. Y., SUNG, H. J. & ZAKI, T. A. 2014 Turbulent thermal boundary layers with temperature-dependent viscosity. *Intl J. Heat Fluid Flow* **49**, 43–52.

LEE, J., YOON JUNG, S., JIN SUNG, H. & ZAKI, T. A. 2013 Effect of wall heating on turbulent boundary layers with temperature-dependent viscosity. *J. Fluid Mech.* **726**, 196–225.

LEE, M. & MOSER, R. D. 2015 Direct numerical simulation of turbulent channel flow up to. *J. Fluid Mech.* **774**, 395–415.

LELE, S. K. 1992 Compact finite difference schemes with spectral-like resolution. *J. Comput. Phys.* **103** (1), 16–42.

LELE, S. K. 1994 Compressibility effects on turbulence. *Annu. Rev. Fluid Mech.* **26** (1), 211–254.

LENERT, A. & WANG, E. N. 2012 Optimization of nanofluid volumetric receivers for solar thermal energy conversion. *Solar Energy* **86** (1), 253–265.

LOZANO-DURÁN, A. & JIMÉNEZ, J. 2014 Effect of the computational domain on direct simulations of turbulent channels up to $Re_\tau = 4200$. *Phys. Fluids* **26** (1), 011702.

MAEDER, T. 2000 *Numerical investigation of supersonic turbulent boundary layers (Ph.D. Thesis)*. ETH Zürich, Institute of Fluid Dynamics.

MAEDER, T., ADAMS, N. A. & KLEISER, L. 2001 Direct simulation of turbulent supersonic boundary layers by an extended temporal approach. *J. Fluid Mech.* **429**, 187–216.

MAJDA, A. & SETHIAN, J. 1985 The derivation and numerical solution of the equations for zero Mach number combustion. *Combust. Sci. Technol.* **42** (3-4), 185–205.

MARQUILLIE, M., EHRENSTEIN, U. & LAVAL, J.-P. 2011 Instability of streaks in wall turbulence with adverse pressure gradient. *J. Fluid Mech.* **681**, 205–240.

MARUSIC, I., MATHIS, R. & HUTCHINS, N. 2010*a* High Reynolds number effects in wall turbulence. *Int. J. Heat Fluid Flow* **31** (3), 418–428.

MARUSIC, I., MATHIS, R. & HUTCHINS, N. 2010*b* Predictive model for wall-bounded turbulent flow. *Science* **329** (5988), 193–196.

MARUSIC, I., MCKEON, B., MONKEWITZ, P., NAGIB, H., SMITS, A. & SREENIVASAN, K. 2010*c* Wall-bounded turbulent flows at high reynolds numbers: Recent advances and key issues. *Phys. Fluids* **22** (6), 065103.

MCMURTRY, P. A., JOU, W.-H., RILEY, J. & METCALFE, R. 1986 Direct numerical simulations of a reacting mixing layer with chemical heat release. *AIAA J.* **24** (6), 962–970.

MODESTI, D. & PIROZZOLI, S. 2016 Reynolds and Mach number effects in compressible turbulent channel flow. *Intl J. Heat Fluid Flow* **59**, 33–49.

MORINISHI, Y., TAMANO, S. & NAKABAYASHI, K. 2004 Direct numerical simulation of compressible turbulent channel flow between adiabatic and isothermal walls. *J. Fluid Mech.* **502**, 273–308.

MORKOVIN, M. V. 1962 Effects of compressibility on turbulent flows. *In Mecanique de la Turbulence, ed. A. Favre* pp. 367–380.

MORRISON, J. F., MCKEON, B. J., JIANG, W. & SMITS, A. J. 2004 Scaling of the streamwise velocity component in turbulent pipe flow. *J. Fluid Mech.* **508**, 99–131.

MOSER, R. D., KIM, J. & MANSOUR, N. N. 1999 Direct numerical simulation of turbulent channel flow up to Re= 590. *Phys. Fluids* **11** (4), 943–945.

MYONG, H. K. & KASAGI, N. 1990 A new approach to the improvement of k-ε turbulence model for wall-bounded shear flows. *JSME Int. J.* **33** (1), 63–72.

NEMATI, H. 2016 *Direct numerical simulation of turbulent heat transfer to fluids at supercritical pressures*. Delft University Press.

NEMATI, H., PATEL, A., BOERSMA, B. J. & PECNIK, R. 2015 Mean statistics of a heated turbulent pipe flow at supercritical pressure. *Intl. J. Heat Mass Transfer* **83**, 741–752.

NICOUD, F. 2000 Conservative high-order finite-difference schemes for low-Mach number flows. *J. Comput. Physics* **158** (1), 71–97.

NICOUD, F. & POINSOT, T. 1999 DNS of a channel flow with variable properties. In *International Symposium on Turbulence and Shear Flow Phenomena (TSFP-1)*, pp. 697–702. Santa Barbara, USA: Begell House.

PAPAMOSCHOU, D. & ROSHKO, A. 1988 The compressible turbulent shear layer: an experimental study. *J. Fluid Mech.* **197**, 453–477.

PATEL, A., PEETERS, J. W. R., BOERSMA, B. J. & PECNIK, R. 2015 Semi-local scaling and turbulence modulation in variable property turbulent channel flows. *Phys. Fluids* **27** (9), 095101.

PATEL, A., BOERSMA, B. J. & PECNIK, R. 2016 The influence of near-wall density and viscosity gradients on turbulence in channel flows. *J. Fluid Mech.* **809**, 793–820.

PATEL, A., BOERSMA, B. J. & PECNIK, R. 2017 Scalar statistics in variable property turbulent channel flows. *Phys. Rev. Fluids, Submitted* .

PECNIK, R. & PATEL, A. 2017 Scaling and modelling of turbulence in variable property channel flows. *J. Fluid Mech., Accepted* .

PEETERS, J. W., PECNIK, R., ROHDE, M., VAN DER HAGEN, T. & BOERSMA, B. 2016 Turbulence attenuation in simultaneously heated and cooled annular flows at supercritical pressure. *J. Fluid Mech.* **799**, 505–540.

PEETERS, J. W. R. 2016 *Turbulence and turbulent heat transfer at supercritical pressure*. Delft University Press.

PEI, J., CHEN, J., HUSSAIN, F. & SHE, Z. 2013 New scaling for compressible wall turbulence. *Sci. China Phys., Mech., Astron.* **56** (9), 1770–1781.

PIORO, I. L., KHARTABIL, H. F. & DUFFEY, R. B. 2004 Heat transfer to supercritical fluids flowing in channels—empirical correlations (survey). *Nucl. Eng. Design* **230** (1), 69–91.

PIROZZOLI, S. & BERNARDINI, M. 2011 Turbulence in supersonic boundary layers at moderate Reynolds number. *J. Fluid Mech.* **688**, 120–168.

PIROZZOLI, S., BERNARDINI, M. & GRASSO, F. 2008 Characterization of coherent vortical structures in a supersonic turbulent boundary layer. *J. Fluid Mech.* **613**, 205–231.

PIROZZOLI, S., BERNARDINI, M. & ORLANDI, P. 2016 Passive scalars in turbulent channel flow at high reynolds number. *J. Fluid Mech.* **788**, 614–639.

PIROZZOLI, S., GRASSO, F. & GATSKI, T. 2004 Direct numerical simulation and analysis of a spatially evolving supersonic turbulent boundary layer at M= 2.25. *Phys. Fluids* **16** (3), 530–545.

POPE, S. B. 2000 *Turbulent flows*. Cambridge University Press.

PUJALS, G., GARCIA-VILLALBA, M., COSSU, C. & DEPARDON, S. 2009 A note on optimal transient growth in turbulent channel flows. *Phys. Fluids* **21** (1), 015109.

REYNOLDS, O. 1883 An experimental investigation of the circumstances which determine whether the motion of water shall be direct or sinuous, and of the law of resistance in parallel channels. *Philos. Trans. R. Soc.* **35** (224-226), 84–99.

RICHARDSON, L. F. 1922 *Weather prediction by numerical process*. Cambridge University Press.

RINGUETTE, M. J., WU, M. & MARTIN, M. 2008 Coherent structures in direct numerical simulation of turbulent boundary layers at Mach 3. *J. Fluid Mech.* **594**, 59–69.

ROBINSON, S. K. 1991 Coherent motions in the turbulent boundary layer. *Annu. Rev. Fluid Mech.* **23** (1), 601–639.

SARKAR, S. 1995 The stabilizing effect of compressibility in turbulent shear flow. *J. Fluid Mech.* **282**, 163–186.

SCHOPPA, W. & HUSSAIN, F. 2002 Coherent structure generation in near-wall turbulence. *J. Fluid Mech.* **453**, 57–108.

SCHWERTFIRM, F. & MANHART, M. 2007 Dns of passive scalar transport in turbulent channel flow at high schmidt numbers. *Intl J. Heat Fluid Flow* **28** (6), 1204–1214.

SHADLOO, M., HADJADJ, A. & HUSSAIN, F. 2015 Statistical behavior of supersonic turbulent boundary layers with heat transfer at $M_\infty = 2$. *Intl J. Heat Fluid Flow* **53**, 113–134.

SMITH, C. & METZLER, S. 1983 The characteristics of low-speed streaks in the near-wall region of a turbulent boundary layer. *J. Fluid Mech.* **129**, 27–54.

SMITS, A. J. & DUSSAUGE, J.-P. 2006 *Turbulent shear layers in supersonic flow*. Springer Science & Business Media.

SMITS, A. J. & MARUSIC, I. 2013 Wall-bounded turbulence. *Physics Today* **66** (9), 25–30.

SPINA, E. F. & SMITS, A. J. 1987 Organized structures in a compressible, turbulent boundary layer. *J. Fluid Mech.* **182**, 85–109.

TENNEKES, H. & LUMLEY, J. L. 1972 *A first course in turbulence*. MIT press.

TRETTEL, A. & LARSSON, J. 2016 Mean velocity scaling for compressible wall turbulence with heat transfer. *Phys. Fluids* **28** (2), 026102.

VREMAN, A. W., SANDHAM, N. & LUO, K. 1996 Compressible mixing layer growth rate and turbulence characteristics. *J. Fluid Mech.* **320**, 235–258.

WILCOX, D. C. 2006 *Turbulence modeling for CFD*. DCW industries, La Canada CA.

WU, Y. & CHRISTENSEN, K. T. 2006 Population trends of spanwise vortices in wall turbulence. *J. Fluid Mech.* **568**, 55–76.

ZHANG, Y.-S., BI, W.-T., HUSSAIN, F., LI, X.-L. & SHE, Z.-S. 2012 Mach-number-invariant mean-velocity profile of compressible turbulent boundary layers. *Phys. Rev. Lett.* **109** (5), 054502.

ZHOU, J., ADRIAN, R. J., BALACHANDAR, S. & KENDALL, T. 1999 Mechanisms for generating coherent packets of hairpin vortices in channel flow. *J. Fluid Mech.* **387**, 353–396.

ZONTA, F., MARCHIOLI, C. & SOLDATI, A. 2012 Modulation of turbulence in forced convection by temperature-dependent viscosity. *J. Fluid Mech.* **697**, 150–174.

ACKNOWLEDGEMENTS

I would like to start by first thanking my supervisors Prof. dr. ir. Bendiks J. Boersma and Dr. Rene Pecnik for giving me the opportunity to pursue this PhD research. I am very thankful to both of them for allowing me to come up with a research subject of my choosing. Their faith instilled a great positive energy in me and has been a constant source of inspiration for me. Thank you both for providing me feedbacks and opportunities that has helped me to develop professionally and also for being so considerate to provide me with a flexible working arrangement that has helped me fulfill my personal commitments. I am thankful to Rene, for his guidance in both professional and personal fronts. I really appreciate the range of our conversations that has helped me become wiser and has improved my perspective of the world. I grew as a better researcher and person under his guidance. This dissertation would not have been possible without him. I thank him for all his efforts and insights.

I would also like to thank colleagues from my research group, Hassan, Jurriaan, Enrico, Uttiya, Simone and Gustavo with whom I had several lively discussions and also collaborated in one or the other way. Special thanks to Jurriaan and Hassan for guiding me through the practical details of the defense process and thanks to Jurriaan for his help in translating the summary from English to Dutch. Next, I would like to thank all my colleagues in the Process and Energy department for creating such a open and creative atmosphere around me. I would also like to express my gratitude to the dissertation committee members for devoting their time and effort in evaluating this dissertation.

I am thankful to my friends of the "Mini van" group - Abhineet, Anurag, Aritra, Darwin, Nakul, Prashant, Ram, Saurabh, Varun- who were like a family away from home and brought humor and warmth in my life. I would also like to extend my gratitude towards the country of The Netherlands that welcomed me so affectionately and has left a lasting impressions of its culture in my memory. Wherever I may be, I will always remain a goodwill ambassador for this country and its people.

I would like to thank my best friend and partner in life - my wife Nidhi- for always being there for me. You are the strength, inspiration and biggest success

of my life. Thank you for bringing our little one - Niara- in this world, the anticipation to see and hold her, enabled me to be more efficient and has played a major role in on-time completion of my PhD. My younger brother, Ayush, has been a bundle of joy in my life. I wish him all the success in his life. Finally, I bow down and express my deepest gratitude to my father and mother for showering their unconditional love and support on me always.

Ashish Patel
Delft, May 2017

CURRICULUM VITÆ

Ashish Patel was born in Raipur, India on 15th August 1987. After finishing his schooling in Raipur in 2005, he enrolled for the bachelor's program in Mechanical Engineering at National Institute of Technology, Allahabad, India. He received a Bachelor of Technology degree with distinction in 2009. After graduation he started working as a Graduate Engineer Trainee in India's leading automobile manufacturer Tata Motors. There he worked on several departments related to engineering and sales of world's least expensive car Tata Nano. After one year of industrial experience, Ashish decided to gain some research experience and started working as a Junior Research Fellow in Indian Institute of Technology Bombay, India, where he worked on several solar based energy conversion systems for 7 months. To study further, Ashish applied to the master's program in Mechanical Engineering at TU Delft, The Netherlands. He was admitted in the program with Delft Excellence Scholarship in Energy and started with his study in September 2011. He received a Master of Science degree with cum laude in August 2013 after defending his thesis on "Turbulence modeling for heat transfer to supercritical pipe flows". He also later received the Best Mechanical Engineering Graduate Award from TU Delft for his thesis. Ashish began his PhD research in September 2013 under the supervision of Prof. dr. ir. Bendiks J. Boersma and Dr. Rene Pecnik in the Process and Energy Department of TU Delft. He presented his results at several national/international conferences and published articles in various international scientific journals. His research received special attention in the form of 'Young Scientist Award' during the Burgers Symposium in Lunteren, The Netherlands. The results of his research work are presented in this thesis. During the PhD research, Ashish also supervised five MSc theses with topics related to radiative and convective heat transfer.

LIST OF PUBLICATIONS

JOURNAL PUBLICATIONS

[1] Nemati, H., Patel, A., Boersma, B. J. & Pecnik, R., "Mean statistics of a heated turbulent pipe flow at supercritical pressure". *Intl. J. Heat Mass Transfer*, 83, 741–752, 2015.

[2] Patel, A., Peeters, J. W. R., Boersma, B. J. & Pecnik, R., "Semi-local scaling and turbulence modulation in variable property turbulent channel flows". *Phys. Fluids*, 27 (9), 095101, 2015.

[3] Nemati, H., Patel, A., Boersma, B. J. & Pecnik, R., "The effect of thermal boundary conditions on forced convection heat transfer to fluids at supercritical pressure". *J. Fluid Mech.*, 800, 531–556, 2016.

[4] Patel, A., Boersma, B. J. & Pecnik, R., "The influence of near-wall density and viscosity gradients on turbulence in channel flows". *J. Fluid Mech.*, 809, 793–820, 2016.

[5] Pecnik, R. & Patel, A., "Scaling and modelling of turbulence in variable property channel flows". *Accepted for publication in J. Fluid Mech.*

[6] Silvestri, S., Patel, A., Roekaerts, D. J. E. M. & Pecnik, R., "Turbulence radiation interaction in channel flow with various optical depths". *Submitted to J. Fluid Mech.*

[7] Patel, A., Boersma, B. J. & Pecnik, R., "Scalar statistics in variable property turbulent channel flows". *Submitted to Phys. Rev. Fluids.*

[8] Rinaldi, E., Patel, A., Schlatter, P. & Pecnik, R."Stability of buffer layer streaks in turbulent channel flows with variable density and viscosity". *In Preparation.*

CONFERENCE PUBLICATIONS AND PRESENTATIONS

[1] Nemati, H., Patel, A., Boersma, B. J. & Pecnik, R., "Direct numerical simulation of turbulent flow with supercritical fluid in a heated pipe". In Proceedings of International Symposium on Turbulence and Shear Flow Phenomena, 2013, Poitiers, France.

[2] Patel, A., Nemati, H., Boersma, B. J. & Pecnik, R., "Heat transfer charac-
     terization and modeling for turbulent supercritical fluid flows in pipes".
     Burgers Symposium, 2014, Delft, The Netherlands.

[3] Patel, A., Peeters, J. W. R, Boersma, B. J. & Pecnik, R., "Numerical experi-
     ments of variable property turbulent channel flow". Bulletin of the Ameri-
     can Physical Society 59, 2014, San Francisco, USA.

[4] Pecnik, R., Nemati, H., Patel, A. & Boersma, B. J., "The effect of large prop-
     erty fluctuations on turbulent heat transfer to supercritical pressure fluids
     in pipes". Bulletin of the American Physical Society 59, 2014, San Francisco,
     USA.

[5] Nemati, H., Patel, A., Boersma, B. J. & Pecnik, R., "The effects of thermal
     boundary condition on turbulent statistics in flow with supercritical CO_2".
     In Proceedings of Direct and Large-Eddy Simulation Workshop, 2015, Li-
     massol, Cyprus.

[6] Patel, A., Peeters, J. W. R, Boersma, B. J. & Pecnik, R., "Effect of viscosity
     and density gradients on turbulent channel flows". European Turbulence
     Conference, 2015, Delft, The Netherlands.

[7] Pecnik, R., Smit, S. H. H. J., Patel, A. & Roekaarts, D. J. E. M., "The influence
     of radiative transfer on the turbulent flow inside solar absorbers operat-
     ing with supercritical CO_2". In Proceedings of International Symposium
     on Supercritical CO_2 Power Cycles, 2016, San Antonio, USA.

[8] Patel, A., Boersma, B. J. & Pecnik, R., "Variable property effects in a turbu-
     lent channel flow ". Burgers Symposium, 2016, Lunteren, The Netherlands.

[9] Patel, A., Pecnik, R., Peeters, J. W. R, Hickel, S. & Moghadam, M. E., "Turbu-
     lence modulation by variable density and viscosity". In Proceedings of the
     2016 Summer Program, Center for Turbulence Research, Stanford Univer-
     sity, USA.

[10] Patel, A., Boersma, B. J. & Pecnik, R., "Influence of property gradients on
     near-wall turbulent structures in a channel flow". European Fluid Mechan-
     ics Conference, 2016, Seville, Spain.

[11] Patel, A., Rinaldi, E., Pecnik, R., Schlatter, P. & Bagheri, S., "Stability of opti-
     mal streaks in the buffer layer of a turbulent channel flow with variable vis-
     cosity. Bulletin of the American Physical Society 61, 2016, Portland, USA.

[12] Pecnik, R., Patel, A., Peeters, J. W. R & Boersma, B. J., "Scaling properties and turbulence modulation of flows with variable density and viscosity". Bulletin of the American Physical Society 61, 2016, Portland, USA.

[13] Pecnik, R. & Patel, A., "Scaling laws for variable property flows". European Turbulence Conference, 2017, Stockholm, Sweden.

[14] Silvestri, S., Patel, A., Roekaerts, D. J. E. M. & Pecnik, R., "Turbulence radiation interaction in fully developed channel flow under various optical depths". European Turbulence Conference, 2017, Stockholm, Sweden.